

# RECONSTRUCTION OF RAILROADS AND HIGHWAYS WITH *IN-SITU* RECLAMATION MATERIALS

by

Principal Investigator: Tuncer B. Edil  
Co-Investigators: James M. Tinjum and Craig H. Benson  
Graduate Assistants: Ali Ebrahimi  
Undergraduate Assistant: Andrew Keene

March 2011

Recycled Materials Resource Center  
University of Wisconsin-Madison  
Madison, WI 53706 USA



# Reconstruction of Railroads and Highways with *in-situ* Reclamation Materials

CFIRE 02-04  
March 2011

National Center for Freight & Infrastructure Research & Education  
College of Engineering  
Department of Civil and Environmental Engineering  
University of Wisconsin, Madison



*Authors:* Ali Ebrahimi, Tuncer Edil, James Tinjum;  
University of Wisconsin-Madison

*Principal Investigator:* Tuncer Edil, James Tinjum, Craig H. Benson;  
Professor, Department of Civil and Environmental Engineering  
University of Wisconsin-Madison



## TECHNICAL REPORT DOCUMENTATION

1. Report No. <b>CFIRE 02-04</b>	2. Government Accession No.	3. Recipient's Catalog No. <b>CFDA 20.701</b>	
4. Title and Subtitle Reconstruction of Railroads and Highways with In-Situ Reclamation Materials		5. Report Date <b>March 2011</b>	
		6. Performing Organization Code	
7. Author/s: <b>Tuncer Edil, James Tinjum, and Ali Ebrahimi</b>		8. Performing Organization Report No. <b>CFIRE 02-04</b>	
9. Performing Organization Name and Address  <b>National Center for Freight and Infrastructure Research and Education (CFIRE) University of Wisconsin-Madison 1415 Engineering Drive, 2205 EH Madison, WI 53706</b>		10. Work Unit No. (TRAI5)	
		11. Contract or Grant No. <b>CFIRE 02-04</b>	
12. Sponsoring Organization Name and Address  <b>Research and Innovative Technology Administration United States Department of Transportation 1200 New Jersey Avenue, SE Washington, DC 20590</b>		13. Type of Report and Period Covered <b>Final Report [12/01/08 – 03/31/11]</b>	
		14. Sponsoring Agency Code	
15. Supplementary Notes Project completed for the <b>CFIRE</b> with support from the Wisconsin Department of Transportation.			
16. Abstract The resilient modulus and plastic deformation of recycled roadway materials with and without fly ash stabilization were characterized using a large-scale model experiment (LSME). Stabilization of recycled pavement materials (RPM) and road surface gravel RSG with 10% by weight of Class C fly ash increased the summary resilient modulus (SRM) two to five times. Moreover, the SRM increased with layer thickness in the LSME. The RPM and RSG exhibited the rate of plastic deformation three to four times higher than the Class 5 base. Stabilized RPM and RSG had the lowest plastic deformation. The moduli obtained from the large-scale model experiment (LSME) were used to develop an equivalency-based design for the recycled materials with and without fly ash. Stabilization of the recycled materials by cementitious fly ash reduced the required thickness of a pavement base course up to 30% in accordance with AASHTO-1993 design guide. The SRM and plastic deformation from LSME tests were incorporated in the Mechanistic Empirical Pavement Design Guide (MEPDG) to predict the lifetime expectancy of the recycled materials in a pavement alone and with fly ash stabilization. The results showed that stabilization of recycled materials with fly ash increases the lifetime of pavements constructed with 0.3-m-thick alternative recycled materials from 17 to 21 years.  A testing protocol and guidelines for testing fouled railway ballast was developed due to the lack of consistent and systematic testing guidelines in the literature and in rail engineering practice. The effect of fouling (internally generated mineral fouling, external coal fouling due to surface spillage, and clay fouling due to subgrade intrusion) on the permanent (plastic) deformation of ballast under traffic loading was studied using the developed testing protocol. Two main phases were distinguished in the development of plastic strain ( $\epsilon_p$ ) with loading cycles in fouled ballast: (1) initial compaction phase (ICP), where the $\epsilon_p$ of ballast steadily increases to a certain point ( $N < 10,000$ ) and (2) fouling impact phase (FIP), where the $\epsilon_p$ and the rate of plastic strain of ballast increases due to the presence of fouling materials (or remains stable in the absence of fouling). A maintenance planning and scheduling software was developed incorporating the mechanistic based predictive model for railway substructure by limiting the surface deviation of the railway track. Maintenance planning for railway track based on deformation of substructure reveals the need for a mechanistic characterization of ballast. Based on the developed model and a given track condition, ballast with initial fouling of 5% requires four maintenance activities (i.e., tamping events) to level the track surface during six years of evaluation. Based on this model, fouling is expected to increase to 25% after six years.  The fundamental mechanistic data generated provide a basis for assessing pavement or rail behavior for various scenarios of freight transport.			
17. Key Words Railways, Highways, Sustainable Construction, Freight Loads		18. Distribution Statement No restrictions. This report is available through the Transportation Research Information Services of the National Transportation Library.	
19. Security Classification (of this report) Unclassified	20. Security Classification (of this page) Unclassified	21. No. Of Pages 98 pages	22. Price -0-

**Form DOT F 1700.7 (8-72)**

**Reproduction of form and completed page is authorized.**

## **DISCLAIMER**

This research was funded by the National Center for Freight and Infrastructure Research and Education. The contents of this report reflect the views of the authors, who are responsible for the facts and the accuracy of the information presented herein. This document is disseminated under the sponsorship of the Department of Transportation, University Transportation Centers Program, in the interest of information exchange. The U.S. Government assumes no liability for the contents or use thereof. The contents do not necessarily reflect the official views of the National Center for Freight and Infrastructure Research and Education, the University of Wisconsin, the Wisconsin Department of Transportation, or the USDOT's RITA at the time of publication.

The United States Government assumes no liability for its contents or use thereof. This report does not constitute a standard, specification, or regulation.

The United States Government does not endorse products or manufacturers. Trade and manufacturers names appear in this report only because they are considered essential to the object of the document.

**TABLE OF CONTENTS**

TECHNICAL REPORT DOCUMENTATION ..... ii

DISCLAIMER ..... iii

TABLE OF CONTENTS ..... iv

LIST OF FIGURES ..... viii

LIST OF TABLES ..... xi

Chapter 1: EXECUTIVE SUMMARY ..... 1

    1.1 Problem Statement and REsearch Objectives ..... 1

        1.1.1 Highway Freight Transport ..... 1

        1.1.2 Rail Freight Transport ..... 1

    1.2 Outlines ..... 1

    1.3 Methods ..... 2

    1.4 Major Findings ..... 2

        1.4.1 Highway research ..... 2

        1.4.2 Railway Research ..... 3

Chapter 2: PRACTICAL APPROACH FOR DESIGNING PAVEMENT STRUCTURES WITH  
    RECYCLED ROADWAY MATERIALS ..... 5

    2.1 Abstract ..... 5

    2.2 Introduction ..... 5

    2.3 Materials ..... 6

    2.4 Methods ..... 7

    2.5 Results and Discussion ..... 9

        2.5.1 Resilient Modulus and Plastic Deformation from LSME ..... 9

        2.5.2 Resilient Modulus from BSRM Test ..... 11

        2.5.3 Comparison between the LSME and BSRM Test results ..... 11

    2.6 Design Approaches for Use of Recycled Materials in Pavement Structures ..... 13

        2.6.1 Equivalency-Based Design Using AASHTO 1993 ..... 14

        2.6.2 Equivalency-Based Design Using MEPDG ..... 16

    2.7 CONCLUSIONS ..... 18

ACKNOWLEDGMENT ..... 19

References ..... 19

Chapter 3: LARGE-SCALE, CYCLIC TRIAXIAL TESTING FOR MEASURING THE  
    DEFORMATION OF FOULED RAILWAY BALLAST ..... 21

    3.1 ABSTRACT ..... 21

    3.2 INTRODUCTION ..... 21

3.2.1 Mechanistic-Based Evaluation of Railway Ballast.....	22
3.3 OBJECTIVES .....	25
3.4 MATERIALS .....	25
3.4.1 Ballast .....	25
3.4.2 Mineral Fouling Material.....	26
3.5 METHOD DEVELOPMENT .....	26
3.5.1 Full-Size Track Model Experiment (FSTME).....	26
3.5.2 Large-Scale, Cyclic Triaxial Equipment .....	26
3.5.2.1 Compaction Method .....	28
3.5.2.2 Membrane Preparation .....	30
3.5.2.3 Specimen Preparation for the LSCT test .....	31
3.5.2.4 Corrections for Membrane Penetration and Strength .....	31
3.5.2.5 Data Acquisition .....	32
3.5.2.6 Volume Change Measurements .....	32
3.5.2.7 Cyclic Loading Used in the Triaxial Testing .....	32
3.5.2.8 Pulse Time and Frequency .....	32
3.5.2.9 Equipment Compliance .....	35
3.6 REPRESENTATIVE STATE OF STRESS FOR LSCT.....	35
3.7 IMPLEMENTATION OF DEVELOPED METHOD .....	35
3.7.1 Sensitivity to Specimen Preparation of Fouled Ballast.....	35
3.7.2 Repeatability of testing .....	38
3.7.3 Membrane Penetration and Volume Measurements.....	38
3.7.4 Effect of Fouling and Water Content on Deformational Behavior of Ballast.....	40
3.8 CONCLUSION AND RECOMMENDATIONS .....	41
ACKNOWLEDGEMENT .....	41
REFERENCES .....	41
Chapter 4: DEFORMATIONAL BEHAVIOR OF FOULED RAILWAY BALLAST .....	44
4.1 ABSTRACT.....	44
4.2 INTRODUCTION .....	44
4.3 MATERIALS .....	44
4.3.1 Fresh Ballast .....	44
4.3.2 Recycled Ballast.....	45
4.3.3 Fouling Materials .....	45
4.4 FOULING RELATED DEFINITIONS .....	47
4.4.1 Fouling Index.....	47

4.4.2 Volumetric Fouling Index (FI) .....	47
4.4.2.1 Contaminated Contact Points of Ballast Particles.....	47
4.5 EXPERIMENTAL EQUIPMENT AND METHODS .....	48
4.5.1 LSCT Test Method .....	49
4.5.2 Specimen Preparation for LSCT test .....	49
4.5.3 Determination of Stress Combinations for Triaxial Testing .....	49
4.6 EXPERIMENTAL RESULTS .....	49
4.6.1 Plastic Strain of Clean Fresh and Recycled Ballast.....	49
4.6.2 Plastic Strain of Fresh and Recycled Ballast with Non-Cohesive Fouling Materials .....	50
4.6.3 Plastic Strain of Fresh Ballast with Non-Cohesive Fouling Materials.....	51
4.6.3.1 Non-Cohesive Fouling Index (NFI) .....	54
4.6.3.2 Non-Cohesive (Mineral and Coal) Fouling Mechanisms.....	56
4.6.4 Plastic Strain of Fresh Ballast with Cohesive Fouling Material .....	57
4.6.4.1 Cohesive Fouling Index .....	59
4.6.4.2 Cohesive (Clay) Fouling Mechanisms .....	60
4.6.5 Suction Control of Cohesive and Non-cohesive Fouling.....	60
4.6.6 Effect of Tamping on Plastic Strain of Fouled Ballast .....	61
4.7 CONCLUSIONS .....	63
ACKNOWLEDGEMENT .....	63
REFERENCES .....	63
Chapter 5: DETECTION OF FOULING IN BALLAST BY ELECTROMAGNETIC SURVEYING	65
5.1 ABSTRACT.....	65
5.2 INTRODUCTION .....	65
5.3 EM WAVE PROPAGATION AND TDR MEASUREMENTS .....	65
5.4 MATERIALS .....	66
5.5 METHODS.....	68
5.6 RESULTS AND DISCUSSION .....	69
5.6.1 TDR Calibration.....	69
5.6.2 Ballast, Fouling, and Water Content .....	71
5.7 CONCLUSIONS .....	75
ACKNOWLEDGEMENT .....	76
REFERENCES .....	76
Chapter 6: MECHANISTIC-BASED MAINTENANCE PLANNING FROM DEFORMATION MODEL OF RAILWAY SUBSTRUCTURE .....	77

6.1 ABSTRACT .....	77
6.2 INTRODUCTION .....	77
6.3 BACKGROUND .....	78
6.3.1 Fouling Indices .....	78
6.3.2 Maintenance Planning Model for Railway Ballast .....	78
6.4 STATISTICAL APPROACH .....	78
6.4.1 Support Vector Regression for Geotechnical Applications .....	78
6.4.2 Support Vector Regression .....	79
6.5 MATERIALS AND METHODS .....	81
6.6 SUMMARY BEHAVIOR OF FOULED BALLAST .....	81
6.7 DEFORMATION MODEL OF RAILWAY BALLAST .....	81
6.7.1 Effect of Fouling and Water Content on the Deformation Model .....	82
6.7.2 Effect of State of Stress on Deformational Behavior of Ballast .....	85
6.7.3 Incremental Analysis by Integrating Change of Fouling, Moisture, and State of Stress .....	87
6.8 DEFORMATION MODEL OF RAILWAY SUBGRADE .....	88
6.9 RAIL TRACK SURFACE DEVIATION .....	89
6.10 MECHANISTIC-BASED MAINTENANCE PLANNING FOR RAIL SUBSTRUCTURE (WiscRail™) .....	89
6.11 ANALYTICAL SUPPORT VECTOR REGRESSION .....	89
6.12 SUMMARY AND CONCLUSIONS .....	93
ACKNOWLEDGEMENT .....	93
REFERENCES .....	93
Chapter 7: SUMMARY AND MAJOR FINDINGS .....	95
7.1 Highway Research .....	95
7.2 Railway Research .....	95

## LIST OF FIGURES

Figure 2.1 RPM aggregates coated with asphalt binders .....	7
Figure 2.2 Particle size distributions of Class 5 base, RPM, and RSG .....	7
Figure 2.3 Large-scale model experiment (LSME) used for prototype pavement testing.....	8
Figure 2.4 Plastic strain and resilient modulus vs. number of load cycles for (a) Class 5, (b) RPM, and (c) RSG with thickness of 0.2 (left) and 0.3 m (right) .....	10
Figure 2.5 Permanent deformation and resilient modulus versus the number of load cycles for (a) RPM and (b) RSG stabilized with fly ash (0.3 m thicknesses) .....	10
Figure 2.6 RSG particle surrounded by the fly ash (a), development of needle-shape ettringite (pointed by arrows) around the fly ash and RSG particles (b) .....	11
Figure 2.7 Summary resilient modulus (SRM) from the LSME and laboratory BSRM test.....	12
Figure 2.8 Strain dependency of the resilient modulus of recycled materials from the BSRM test and LSME .....	13
Figure 2.9 Summary resilient modulus (SRM) of Class 5 base, RPM, RSG, SRPM, and SRSG as a function of base course thickness .....	13
Figure 2.10 Layer coefficients for Class5 base, RPM, RSG, SRPM, and SRSG as a function of base course thickness .....	14
Figure 2.11 Schematic pavement profiles for equivalency based design between conventional and alternative recycled base course materials.....	15
Figure 2.12 Alternative recycled material thickness as a function of Class 5 thickness .....	16
Figure 2.13 Life time expectancy of pavement structure built by conventional and alternative base course materials for limited rut depth (a) and IRI (b) from the MEPDG code .....	18
Figure 3.1 Typical Components of Substructure and Superstructure in a Railway Track .....	22
Figure 3.2 Interaction and Contributions of Environment, Track condition, and Loading on Deformational Behavior of Railway Substructure .....	23
Figure 3.3 Particle Size Distribution of Ballast and Mineral Fouling (AREMA#24 is the Limits for a Standard Ballast, AREMA 2003) .....	25
Figure 3.4 Schematic Configuration of Full-Size Prototype Track Model Experiment (FSTME) .....	27
Figure 3.5 Schematic Configuration of Large-Scale Cyclic Triaxial (LSCT) Equipment for Measuring Plastic Deformation of Railway Ballast.....	27
Figure 3.6 Proposed Compaction Process: Rearranging Particles with Vibratory Rod (Left) and 45-N Dropping Plate for Densification (Right).....	29
Figure 3.7 Calculated State of Stress in Railway Ballast from Finite Element Analysis and Proposed Stress Combinations (Solid Symbols) for Testing Ballast in the LSCT Test.....	33
Figure 3.8 Havesine (HS) Function Fitted to the Stress Distribution Curves in Different Depth of Ballast to Determine the Pulse Length (Time) Used in the LSCT Test .....	34
Figure 3.9 Pulse Time for Ballast Loading as a Function of Ballast Depth under Ties.....	34

Figure 3.10 Matching the Plastic Strain of Ballast Obtained from Full-Size Track Model Experiment (FSTME) with the One Obtained from Different State of Stresses in Large-Scale Cyclic Triaxial (LSCT) Test.....	36
Figure 3.11 Highly Fouled Ballast (a), Moderately (5%) Fouled Ballast (b), Clean Ballast (c), Layered Fouling Mixture (d), Ballast Aggregate Coated by Fouling (e), and Cross Section of Fouled Ballast (f) from the Specimens of Large-Scale Cyclic Triaxial Test .....	36
Figure 3.12 Effect of Specimen Preparation on Accumulation of Plastic Strain of Fouled Ballast in 20% by Weight of Fouling (F) and 15% Moisture (w) Obtained from LSCT Test.....	37
Figure 3.13 Repeatability of Collected Plastic Strain of Ballast in Clean (a) and Fouled (b) Condition from LSCT Equipment .....	39
Figure 3.14 Volume Change of a Clean Ballast Specimen with Time in LSCT Equipment after Confining Stress is Applied.....	40
Figure 4.1 Particle Size Distribution of Fresh and Recycled ballast and Mineral and Coal Fouling .....	45
Figure 4.2 Various Conditions of Ballast Particles Mixed with Fines, (a) Clean Contacts, (b) Minor Fines and Unaffected Contacts, and (c) Contaminated Contacts with Meta-Stable Structure .....	47
Figure 4.3 Large-Scale Cyclic Triaxial (LSCT) Apparatus for Ballast Testing (left) and a Prepared Railway Ballast Specimen before Testing (right) .....	48
Figure 4.4 Accumulation of Plastic Strain of Fresh and Recycled Ballast in Clean and Fouled Condition.....	50
Figure 4.5 Accumulation of Plastic Strain and Rate of Plastic Strain as a Function of Number of Loading Repetitions for Mineral Fouling in FI=24% (a) and 12% (b) .....	52
Figure 4.6 Accumulation of Plastic Strain and Rate of Plastic Strain as a Function of Number of Loading Repetitions for Coal Fouling in FI=24% (a) and 12% (b).....	53
Figure 4.7 Plastic Strain of Ballast after $N=2 \times 10^5$ ( $\epsilon_{pu}$ ) as a Function of Water Content and Fouling Index (a) and Non-Cohesive Fouling Index (NFI) (b).....	56
Figure 4.8 Accumulation of Plastic Strain of Fouled Railway Ballast in Arithmetic-Scale with Cohesive Fouling Materials and Moisture.....	58
Figure 4.9 Accumulation of Plastic Strain of Ballast Fouled with Cohesive Fouling Materials after Moisture was Added in $N= 2 \times 10^5$ (see Fig. 4.8) .....	59
Figure 4.10 Correlation between Plastic Strain of Fouled Ballast and Cohesive Fouling Index (CFI).....	60
Figure 4.11 Defined Zone for Deformational Behavior of Fouled Ballast in ICP and FIP in the Soil Water Characteristics Curves of Fouling Materials (Note: C=clay fraction)....	62
Figure 4.12 Simulation of Rainfall and Tamping in Highly Fouled Ballast .....	62
Figure 5.1 Particle Size Distribution of Ballast, Coal Dust Fouling, and Mineral Ballast Fouling .....	67
Figure 5.2 Test setups on Clean Ballast, Fouling Materials, and Fouled Ballast with various Fouling Material and Moisture Contents .....	68

Figure 5.3 Schematic Diagram of TDR Testing Components. Note: TDR probes were attached to the wall of a polyvinyl chloride (PVC) pipe .....	69
Figure 5.4 Comparison between EM Waveform Propagation in Different Probe Configurations.....	70
Figure 5.5 Calibration of TDR Probes in Different Testing Media.....	70
Figure 5.6 Collected TDR Data on Dry Ballast .....	72
Figure 5.7 Collected TDR Data on Dry Fouled Ballast .....	72
Figure 5.8 Comparison between TDR Results Collected for Test on Fouled Ballast at 5 and 10% Water Content.....	73
Figure 5.9 Collected TDR Data on Coal-Dust Fouled Ballast at 0 and 10% Water Content .....	74
Figure 5.10 Change in Dielectric Permittivity and EM Wave Velocity of Various Fouled Ballast (a) and Electrical Conductivity of Mineral Fouling (b) for Different Depths of Fouling .....	75
Figure 6.1 Different Components of Railway Maintenance Planning .....	79
Figure 6.2 Pre-specified Accuracy $\epsilon$ and Slack Variable ( $\zeta$ ) in Support Vector Regression (after Scholkopf 1997).....	80
Figure 6.3 Deformation Model for Railway Ballast Presented by Deformation of Clean ballast and Fouled Ballast with FI=24% and w=14% .....	82
Figure 6.4 Parameters 'a' and 'b' in Deformation Model of Railway Ballast as a Function of FI and w .....	84
Figure 6.5 Normalized Deformation Parameters (i.e., a and b) of Railway Ballast as a Function of Principal Stress Ratios .....	86
Figure 6.6 Maintenance Planning Using Incremental Analysis of Deformation Model for Ballast with Changing States of Fouling, Moisture, and Traffic.....	88
Figure 6.7 Graphical User Interface Software of Mechanistic Based Maintenance Model of Railway Substructure (WiscRail™) .....	91
Figure 6.8 Comparison of Predicted Data from Ballast Deformation Model and Statistical Regression Method (SVR with $\epsilon$ -insensitive of 0.1).....	92

## LIST OF TABLES

Table 2.1 Chemical composition of Columbia fly ash in comparison with Class C fly ash .....	6
Table 2.2 Index properties of tested base course materials .....	6
Table 2.3 Input parameters for MEPDG program .....	17
Table 3.1 State of Stress, Load Frequency, and Specimen Size in Previous Studies of Railway Ballast.....	24
Table 3.2 Compaction Methods for Preparation of Ballast Specimens in Previous Studies.....	30
Table 3.3 Membrane Thickness and Preparation for Testing Railway Ballast in Previous Triaxial Testing.....	31
Table 4.1 Index Properties of Ballast and Non-Cohesive Fouling Materials.....	46
Table 4.2 Index Properties of Cohesive Fouling Materials .....	46
Table 4.3 Plastic Strain of Railway Ballast at $N= 2 \times 10^5$ ( $\epsilon_{pu}$ ) for Non-Cohesive Fouling Materials .....	55
Table 4.4 Plastic Strain of Railway Ballast at $N= 2 \times 10^5$ ( $\epsilon_{pu}$ ) for Cohesive Fouling Materials....	58
Table 6.1 Deformation Model Parameters for Railway Ballast in Various Fouling Conditions ..	86
Table 6.2 Deformation Model Parameters for Railway Subgrade (from Li and Selig 1994) .....	89

## **CHAPTER 1: EXECUTIVE SUMMARY**

### **1.1 PROBLEM STATEMENT AND RESEARCH OBJECTIVES**

A major concern facing the freight transport industries in the United States (US) is increased maintenance due to heavier freight load. This report focuses on sustainable construction of highways and railways for increasing freight capacity of the transportation systems in the US. First, a methodology for increasing the freight capacity of highways using sustainable geo-materials is explained. Second, service life and freight capacity of railroad systems in various substructure conditions is determined for predicting the maintenance planning of railway tracks.

#### **1.1.1 Highway Freight Transport**

Recycling part or all of the pavement materials in an existing road during rehabilitation and reconstruction is an attractive construction alternative. For roads with a hot mix asphalt (HMA) surface, the HMA, underlying base, and a portion of the existing subgrade often are pulverized to form a new base material referred to as recycled pavement material (RPM). Similarly, when an unpaved road with a gravel surface is upgraded to a paved road, the existing road surface gravel (RSG) is blended and compacted to form a new base layer. Recycling pavement and road materials in this manner is both cost effective and environmentally friendly. Recycled road materials may contain asphalt binder, fines, and/or other deleterious materials that can adversely affect strength and stiffness. To address this issue, chemical stabilizing agents such as cement, cement kiln dust (CKD), or cementitious fly ash can be blended with RPM and RSG to increase stiffness and to limit rutting. Use of industrial byproducts for stabilization, such as CKD or self-cementing fly ash, is particularly attractive in the context of sustainability. The purpose of this study was to develop a practical method to design roadways using recycled materials and increase the freight capacity of highways by stabilizing the recycled road materials using cementitious industrial byproducts. The project consisted of three major elements: (i) laboratory testing, (ii) prototype pavement evaluation, and (iii) development of a design guide.

#### **1.1.2 Rail Freight Transport**

The main reason for railway maintenance is surface deviation of tracks, which results from accumulation of deformation from the different components of the track substructures, including ballast and subgrade. Among these components, railway ballast has a significant role in effectively distributing the train loads to the underlying subgrade. Ballast degrades under repetitive train loads and ultimately deviates from the original specifications. Generation of fines within ballast creates 'fouled ballast', which is one of the main causes of track surface deviation. Fouling drastically changes the deformational behavior of railway track and increases related maintenance costs. There is limited data available to characterize the deformational behavior of ballast in various states of fouling and predict the ballast-related maintenance. Improvements in the mechanistic-based characterization of plastic (permanent) deformation of railway ballast greatly assist in the prediction of surface deviation of rail tracks and associated maintenance planning. Improved characterization techniques for railway ballast and prediction of the mechanistic behavior would allow railway professionals to evaluate initiatives for increasing the freight capacity and speed in railway systems. The mechanistic-based approach reduces the uncertainties in prediction of track lifetime and related maintenance especially in the absence of historical track performance data related to heavier freight loads and higher speed. The objectives of this research were to (1) develop a testing protocol for characterizing deformational behavior of fouled railway ballast, (2) describe fouling mechanisms by which the deformational behavior of ballast changes, (3) quantify the surface deviation of rail track by developing a deformation model for ballast, and (4) apply the developed deformation model into a railway maintenance planning model.

### **1.2 OUTLINES**

This report is written as a collection of five technical papers. First, a methodology for increasing the freight capacity of highways using stabilized base course materials with cementitious industrial byproducts is discussed in Chapter 2. Second, testing protocol is developed and presented in Chapter 3 to quantify the deformation of ballast at a laboratory-scale, which closely simulates field conditions. In Chapter 4, accumulation of plastic deformation of railway ballast under traffic loading is discussed. Effect

of type of fouling, fouling content, and moisture on plastic deformation of ballast is discussed. Mechanisms, such as contaminated contact points of ballast particles and change in shear strength of fouling materials, that affect the plastic deformation of ballast are described in Chapter 4. A geophysical (i.e., electromagnetic surveying) technique to inspect the fouling content and moisture in railway ballast is presented in Chapter 5. Time domain reflectometry (TDR) is proposed for use in conjunction with ground penetrating radar (GPR) to determine fouling and moisture conditions in ballast. In Chapter 6, a deformation model for railway ballast was developed to predict maintenance cycles for railway track due to deformation of rail substructure.

### **1.3 METHODS**

In Chapter 2, the resilient modulus and plastic deformation of recycled roadway materials with and without fly ash stabilization are presented using a large-scale model experiment (LSME). The LSME simulate a part of pavement structure close to the field condition. The data obtained from the LSME were used in the mechanistic empirical pavement design guide (MEPDG) software to determine the life expectancy of recycled base course materials and increased freight capacity of highways.

In Chapter 3, a testing protocol was developed that includes a representative state of stress in railway ballast, loading frequency, equipment dimensions, data acquisition system, and specimen preparation. Large-scale cyclic triaxial (LSCT) equipment with automated data acquisition and loading control systems was designed to simulate the ballast conditions under cyclic traffic loading. A finite element analysis (FEA) was conducted for a typical railway track configuration to determine the range of stresses in ballast required for LSCT testing. The representative state of stress was established by comparing the deformational response of ballast from the LSCT with that from a full-scale track model experiment (FSTME). The state of stress conditions developed in Chapter 2 were employed in the testing program described in Chapter 4 to investigate the effect of fouling and moisture content on plastic deformation of ballast. In Chapter 5, a bench-scale TDR testing on fouled ballast specimens was performed to find a correlation between EM wave properties (i.e., electrical conductivity and dielectric permittivity) of fouled ballast and fouling/moisture conditions of fouled ballast.

A deformation model for railway ballast was developed in Chapter 6 to predict the maintenance of railway track under various traffic scenarios, fouling conditions, moisture content, ballast quality, subgrade condition, and freight capacity. This maintenance model incorporates the deformational behavior of ballast obtained in Chapter 4 and the ballast quality at the beginning of an evaluation obtained by the geophysical inspection techniques described in Chapter 5. Systematically, the deformation model (a) incorporates the impact of moisture, fouling, and state of stress on deformation of ballast, (b) develops an integration method to account for continual change of fouling content, moisture, and freight loads, and (c) outputs a maintenance-planning program for railway track due to deformation of ballast and subgrade via a computer software program.

### **1.4 MAJOR FINDINGS**

#### **1.4.1 Highway research**

Resilient modulus and plastic deformation of two recycled base course materials, recycled pavement material (RPM) and road surface gravel (RSG), were investigated using a large-scale model experiment (LSME) and laboratory bench-scale resilient modulus (BSRM) tests. The RPM and RSG were tested alone and with 10% by weight of Class C fly ash. A natural limestone aggregate (Class 5) was tested as a reference material. The LSME is a prototype-scale pavement test apparatus where cyclic loading is applied and deformations are measured. The LSME replicates field conditions and accounts for scale effects and mixing and curing conditions. The LSME results showed that stabilization of RPM and RSG with 10% by weight of Class C fly ash increased the summary resilient modulus (SRM) two to five times. Moreover, the SRM increased with layer thickness in the LSME. However, the RPM and RSG exhibited the rate of plastic deformation three to four times higher than the Class 5 base. Stabilized RPM and RSG had the lowest plastic deformation. The moduli obtained from the LSME were used to develop an equivalency-based design for the recycled materials with and without fly ash. Stabilization of the recycled materials by fly ash reduced the required thickness of a pavement base course up to 30% in accordance with AASHTO-1993 design guide. The SRM and plastic deformation from LSME tests were incorporated in the Mechanistic Empirical Pavement Design Guide (MEPDG) to predict the lifetime expectancy of the

recycled materials in a pavement alone and with fly ash stabilization. The results showed that stabilization of recycled materials with fly ash increases the lifetime of pavements constructed with 0.3-m-thick alternative recycled materials from 17 to 21 years.

#### 1.4.2 Railway Research

A testing protocol and guidelines for testing fouled ballast was developed due to the lack of consistent and systematic testing guidelines in the literature and in rail engineering practice. Confining stress ( $\sigma_3$ ) in the ballast layer varied between 20 and 200 kPa, and deviator stress ( $\sigma_d$ ) between 50 and 300 kPa. A 5-Hz haversine, bell-shaped loading pulse simulates the traffic loading on ballast. A representative state of stress for railway ballast of  $\sigma_3 = 90$  kPa and  $\sigma_d = 300$  kPa in the LSCT was determined. Ballast that is mixed with relatively dry fouling material prior to compaction prevents the development of heterogeneous layers and simulates tamping activities (such as performed during maintenance events) in the track. Moisture that is added from the top of the specimen was found to best represent changing water content conditions during the study of deformational behavior of ballast.

The effect of fouling (internally generated mineral fouling, external coal fouling due to surface spillage, and clay fouling due to subgrade intrusion) on the permanent deformation of ballast under traffic loading was studied. Large-scale cyclic triaxial test results showed that increased fouling and moisture content accelerate the accumulation of plastic strains ( $\epsilon_p$ ) in ballast. Two main phases were distinguished in the development of  $\epsilon_p$  with loading cycles (N) in fouled ballast: (1) initial compaction phase (ICP), where the  $\epsilon_p$  of ballast steadily increases to a certain point ( $N < 10,000$ ) and (2) fouling impact phase (FIP), where the  $\epsilon_p$  and the rate of plastic strain of ballast increases due to the presence of fouling materials (or remains stable in the absence of fouling). For non-cohesive (mineral and coal) fouling, fouling index and moisture were the controlling parameters. A non-cohesive fouling index (NFI) was introduced to account for the factors affecting the  $\epsilon_p$ . For cohesive (clay) fouling, in addition to fouling index and moisture, Atterberg limits (PL and LL), and percent passing #200 sieve (the fines) were identified as controlling parameters. A cohesive fouling index (CFI) was introduced to account for these factors. In this perspective, the indices for fouled ballast are expected to provide useful tools for assessing track condition. These parameters allow a mechanistically-based rating system for controlling the quality of railway tracks more completely than the previous indices (e.g., Selig and Waters 1994; Inscoes 2002) that do not require information about critical fouling levels and the ability to extend results for a lifetime assessment. A limit for deformational behavior of fouled ballast was illustrated using a suction-based criterion. For the representative state of stress for ballast, fouling materials, irrespective of type, with suction greater than 2,000 kPa only show the initial compaction phase. The main mechanism for accumulation of plastic strain in ballast is considered to be the contaminated contact points of ballast particles by the fouling materials. Also, decreased shear strength of fouling materials at the contact points under cyclic loading increases the plastic strain of ballast in cohesive and non-cohesive fouling. The effect of maintenance on  $\epsilon_p$  was studied. Ballast in a highly fouled condition exhibits extensive  $\epsilon_p$  immediately after tamping due to rearrangement of the particles and loss of the dense condition that has been achieved in previous traffic loading.

Depth and moisture content of fouling were evaluated using time-domain reflectometry (TDR) technique. The waveforms generated from the TDR probes showed that the increase in the water content and depth of fouling changes the electromagnetic properties of ballast. Increasing the fouling depth of ballast from 0 to 75% of the full depth increases the relative real dielectric permittivity of fouled ballast from 1.2 to 2.0, while the EM wave velocity of media decreases from 0.27 to 0.21 m/ns. The TDR data showed that increasing the water content of fouling material increases the electrical conductivity, calculated from TDR waveforms. An increase in the water content of fouling from 5 to 10% increases the electrical conductivity of fouled ballast three times. The data obtained from the TDR show that a qualitative method can be developed to detect the depth of fouling and water content in the ballast by evaluating the change in the electromagnetic properties of ballast during gradual changes of fouling content, starting with clean ballast.

As a practical application, a maintenance planning and scheduling program of railway substructure is proposed. A deformation model including fouling impact phase and initial compaction phase was developed based on the data obtained from the LSCT apparatus. FIP and ICP in the deformation model were characterized in various fouling conditions, moisture contents, and states of stress. A maintenance planning and scheduling software was developed incorporating the mechanistic based predictive model

for railway substructure by limiting the surface deviation of the railway track. Developing a maintenance planning for railway track based on deformation of substructure reveals the need for a mechanistic characterization of ballast. Based on the developed model and a given track condition, ballast with initial fouling of 5% requires four maintenance activities (i.e., tamping events) to level the track surface during six years of evaluation. Based on this model, fouling is expected to increase to 25% after six years.

## **CHAPTER 2: PRACTICAL APPROACH FOR DESIGNING PAVEMENT STRUCTURES WITH RECYCLED ROADWAY MATERIALS**

### **2.1 ABSTRACT**

Use of recycled roadway materials in the rehabilitation and reconstruction of pavement has been accelerated recently. Even though several studies on the mechanical properties of recycled roadway materials have been performed, a design method accounting for the long-term performance of these materials has not been yet developed. In this study, resilient modulus and plastic deformation of two recycled base course materials, recycled pavement material (RPM) and road surface gravel (RSG), were investigated using a large-scale model experiment (LSME) and laboratory bench-scale resilient modulus (BSRM) tests. The RPM and RSG were tested alone and with 10% by weight of Class C fly ash. A natural limestone aggregate (Class 5) was tested as a reference material. The LSME is a prototype-scale pavement test apparatus where cyclic loading is applied and deformations are measured. The LSME replicates field conditions and accounts for scale effects and mixing and curing conditions. The LSME results showed that stabilization of RPM and RSG with 10% by weight of Class C fly ash increased the summary resilient modulus (SRM) two to five times. Moreover, the SRM increased with layer thickness in the LSME. However, the RPM and RSG exhibited the rate of plastic deformation three to four times higher than the Class 5 base. The moduli obtained from the LSME were used to develop an equivalency-based design for the recycled materials with and without fly ash. Stabilization of the recycled materials by fly ash reduced the required thickness of a pavement base course up to 30% in accordance with AASHTO-1993 design guide. The SRM and plastic deformation from LSME tests were incorporated in the Mechanistic Empirical Pavement Design Guide (MEPDG) to predict the lifetime expectancy of the recycled materials in a pavement alone and with fly ash stabilization. The results showed that stabilization of recycled materials with fly ash increases the lifetime of pavements constructed with 0.3-m-thick alternative recycled materials from 17 to 21 years.

### **2.2 INTRODUCTION**

The ability to recycle existing pavement materials in the rehabilitation and reconstruction of roads provides an attractive alternative to conventional methods such as full removal and replacement of the pavement materials. Existing deteriorated asphalt surface can be pulverized and mixed with the underlying materials to form a new recycled base layer known as recycled pavement material (RPM). The depth of pulverization typically ranges from 100 to 300 mm and includes partly or fully the base course and even part of the underlying subgrade (1). Similarly, when upgrading unpaved gravel roads to a roadway with a paved surface, the existing road surface gravel (RSG) can be incorporated as a base or subbase.

In-situ recycling of roadway materials is cost effective and environmentally friendly, resulting in reduced energy consumption, greenhouse gas emissions, and waste material disposal (2, 3). However, the asphalt binder in RPM and fines in RSG may adversely affect the strength, stiffness, and plastic deformation of the recycled materials used as base course (4-8). A method to enhance the performance of the recycled roadway materials is chemical stabilization with binders like cement, asphalt emulsion, lime, cement kiln dust, or fly ash.

The behavior of pavement materials stabilized with fly ash has received increasing attention in recent years (7, 9-13). Fly ash is a byproduct of coal combustion power plant which often has cementitious properties. Adding Class C or self-cementitious high carbon fly ash to RPM and RSG increases CBR and resilient modulus (2, 14-18). Field studies have also showed significant and persistent increases in the modulus of fly ash stabilized layers over several years of service (2, 10-11, 14).

Determining the appropriate thickness of the pavement layers based on engineering properties is a critical task in the design of pavements, particularly when alternative materials are used. The objective of this study was to develop a methodology to incorporate RPM and RSG as a base course alone and with fly ash stabilization in pavement design. The behavior of the materials were characterized through a large-scale model experiment (LSME) and laboratory bench-scale resilient modulus (BSRM) test in accordance with NCHRP 1-28a. Data from the BSRM test were compared to those from the LSME to account for the effects of the test conditions and scale on resilient modulus. The resilient moduli and plastic deformations obtained from the LSME were used to develop a methodology for designing

pavements with these materials. Two design methods using AASHTO 1993 and AASHTO 2008 (Mechanistic Empirical Pavement Design Guide (MEPDG)) were both considered.

### 2.3 MATERIALS

Recycled RPM and RSG alone and with fly ash stabilization were evaluated as alternative base course materials to conventional crushed aggregate base. Class 5 base aggregate, according to Minnesota Department of Transportation (MnDOT) gradation specification, was selected as a reference, conventional base course aggregate. Class 5 base was a limestone aggregate. The RPM was approximately equal mixture of pulverized hot mix asphalt and limestone base course layers from a roadway reconstruction project in Madison, WI. Asphalt coated aggregates in the RPM were mostly limestone and dolomite based on the results of X-ray diffraction (XRD) tests and were coated with 0.1 to 3-mm thick asphalt binder (Fig. 2.1). The RPM had 4.7% asphalt content (ASTM D6307). The RSG was created by combining Class 5 base with clay fines to meet the gradation and plasticity requirements for surface course materials as described in AASHTO M 147. Particle size distributions of Class 5, RPM, and RSG are given in Fig. 2.2.

Class C fly ash was obtained from Unit 2 of Columbia Power Station (Alliant Energy) in Portage, WI. Columbia fly ash has self-cementing properties and classified as Class C according to ASTM C 618 (Table 2.1). RPM and RSG alone and with 10% by weight fly ash (called 'SRPM' and 'SRSG', respectively) were tested as alternative base course materials. Index properties, classification, and compaction characteristics of these base materials are give in Table 2.2.

Table 2.1 Chemical composition of Columbia fly ash in comparison with Class C fly ash

Parameter	Columbia fly ash	Typical Class C ASTM C618
SiO <sub>2</sub> , %	31.1	40
Al <sub>2</sub> O <sub>3</sub> , %	18.3	17
Fe <sub>2</sub> O <sub>3</sub> , %	6.1	6
SiO <sub>2</sub> + Al <sub>2</sub> O <sub>3</sub> + Fe <sub>2</sub> O <sub>3</sub> , %	55.5	63
CaO, %	23.3	24
MgO, %	3.7	2
SO <sub>3</sub> , %	-	3
CaO/SiO <sub>2</sub>	0.8	0.6
CaO/(SiO <sub>2</sub> +Al <sub>2</sub> O <sub>3</sub> )	0.4	0.4
Loss on Ignition, LOI, %	0.7	6

Table 2.2 Index properties of tested base course materials

	w <sub>opt</sub> (%)	γ <sub>d max</sub> (kN/m <sup>3</sup> )	LL (%)	PL (%)	Fines Content (%)	AASHTO (USCS)	Poisson Ratio (ν)
Class 5	5.0	20.9	NP	NP	4	A-1-a (SP)	0.35*
RPM	7.5	21.2	NP	NP	11	A-1-a (GW-GM)	0.35*
RSG	7.5	22.6	21	14	12	A-2-4 (SC-SM)	0.32*
SRPM	8.5	20.4	-	-	-	-	0.2
SRSG	6.6	22	-	-	-	-	0.2

NOTE.- Particle size analysis by ASTM D422, γ<sub>d max</sub> and w<sub>opt</sub> by ASTM D698, AASHTO classification by ASTM D3282, Asphalt Content by ASTM D6307, and Atterberg limits by ASTM D 4318. \*Data from Schuettpelez et al. (19)



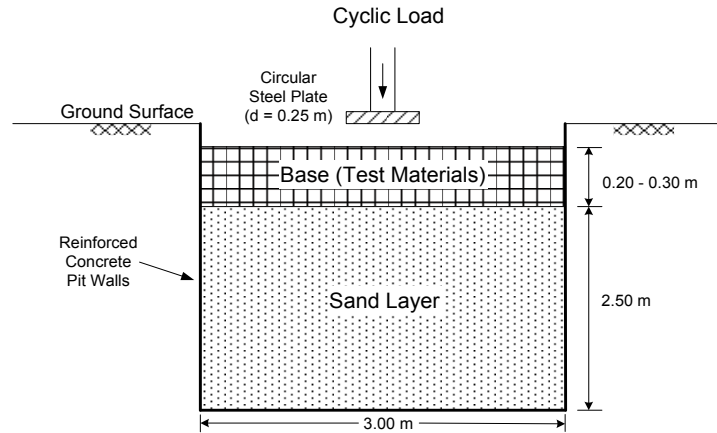


Figure 2.3 Large-scale model experiment (LSME) used for prototype pavement testing

A loading frame (100-kN actuator with 165-mm stroke) and a steel loading plate (125-mm radius and 25-mm thickness) were used to apply cyclic loading to the surface of the pavement. The stress applied at the surface of the base course was estimated by conducting nonlinear finite-element simulations of a pavement profile similar to the one in the LSME but with a 0.1-m thick HMA layer using the program MICHPAVE (21). MICHPAVE accounts for the stress dependency of base course modulus. The simulated pavement was subjected to traffic wheel loads corresponding to 4-axle trucks (70 kN per axle and 35 kN per wheel set) with a tire pressure of 700 kPa. The MICHPAVE analysis showed that the stress at the surface of the base course decreased to 144 kPa with relatively uniform magnitude within the 125-mm radius of loading plate. Thus, load of 7 kN was applied to the plate so that the average stress for the plate was 144 kPa. This load was applied in a haversine pulse shape with loading period of 0.1 s followed by rest period of 0.9 s (NCHRP 1-28a). Deflections at the surface of base course layer and subgrade were measured by six linear variable differential transducers (LVDTs) with 5-mm stroke. Four of the LVDTs measured the deflection at the surface of the base course, and two of them at the surface of the subgrade. Thus, the total, elastic, and plastic deflections at top of the loading plate and the subgrade were determined, and the difference is designated as the deformation in the base course. The recoverable portion of the deflection during a loading pulse was designated as the elastic deflection. The difference between the total deflection and elastic deflection was designated as the plastic deflection. More details on the testing conditions can be found in Benson et al. (22).

MICHPAVE was used to backcalculate the resilient modulus of each base course material using the elastic deflection data for the base course recorded in the LSME. Resilient modulus of the base layer ( $M_r$ ) was assumed to follow the nonlinear elastic power function model,

$$M_r = k_1 \left( \frac{\sigma_b}{p_r} \right)^{k_2} \quad (\text{Eq. 2.1})$$

where  $\sigma_b$  is the bulk stress,  $p_r$  is a reference stress (1 kPa in this study), and  $k_1$  and  $k_2$  are empirical parameters. The parameter  $k_2$  is dimensionless and represents the stress dependency of modulus and falls in the range of 0.45 to 0.62 for granular base course materials (23). The parameter  $k_2$  of each base course material was assumed to be constant in the LSME and set at the value obtained for the same material from the BSRM test. The parameter  $k_1$  was varied until the deflection predicted by MICHPAVE matched the measured elastic deflection in the LSME. This inversion yields the resilient modulus as a function of bulk stress,  $\sigma_b$ , as well as the distribution of stress and strain within the pavement system. A summary resilient modulus (SRM) was computed, as suggested in NCHRP 1-28a, corresponding to a bulk stress of 208 kPa. The underlying sand layer was assumed linear elastic (modulus = 70 MPa). The average plastic strain ( $\epsilon_p$ ) in the base layer was defined as:

$$\varepsilon_p = \frac{d_p}{t} \times 100 \quad (\text{Eq. 2.2})$$

where  $d_p$  is the plastic deflection and  $t$  is the thickness of the base layer.

Standard BSRM test was performed on compacted specimens of base course materials in accordance with NCHRP 1-28a test protocol (Procedure Ia). Specimens were compacted in six lifts of equal mass and thickness using a split mold having 152-mm diameter and 305-mm height. All materials were compacted to 100% of standard Proctor maximum dry unit weight at optimum water content (Table 2.1). Resilient modulus in various bulk stresses was calculated, and the fitting parameters (i.e.,  $k_1$  and  $k_2$ ) in Eq. 2.1 were determined. A summary resilient modulus (SRM) was calculated corresponding to  $\sigma_b$  of 208 kPa.

## **2.5 RESULTS AND DISCUSSION**

### **2.5.1 Resilient Modulus and Plastic Deformation from LSME**

Performance and response of the pavement structure can be determined from the resilient modulus and cumulative plastic strain of the pavement layers (23). The stress and strain distributions within a pavement layer are defined by the resilient modulus. The long-term performance of pavement structure is determined by plastic deformation characteristics of pavement materials. Plastic strain ( $\varepsilon_p$ ) and summary resilient modulus (SRM) of RPM, RSG, and Class 5 base as a function of number of load cycles ( $N$ ) from the LSME are shown in Fig. 2.4 for two base thicknesses (0.20 and 0.30 m). In all cases, the SRM and plastic strain increase monotonically with number of loading cycles. The Class 5 base reaches a steady-state condition (negligible rate of plastic strain ( $d\varepsilon_p/d\ln(N) = 0.01$ )) or plastic shakedown in 2,000 cycles. Werkmeister et al. (24) showed the same behavior for other conventional base course materials and natural aggregates. In contrast, RSG exhibits a high initial rate of permanent deformation for both layer thicknesses, which diminishes to a lower and near constant rate of deformation after 2,000 cycles. This behavior is expected due to the plastic fines (12%) in RSG (also noted by Yang et al. (25)) and suggests that RSG exhibits creep shakedown behavior. The RPM exhibits a similar behavior as the RSG. However, for RPM, the initial rate of plastic strain is lower although the transition to a constant rate of plastic strain also occurs after  $N=2,000$ . The rate of plastic strain accumulation of RPM ( $d\varepsilon_p/d\ln(N) = 0.07$ ) is lower than that of RSG ( $d\varepsilon_p/d\ln(N) = 0.12$ ) when the rate of plastic strain becomes constant. Similar findings have been reported by Mohammad et al. (26) for recycled asphalt pavement (RAP) subjected to cyclic loading. The longer transition to a constant rate of plastic deformation for RPM is attributed to the viscous characteristic of the asphalt in the RPM. The RPM contains limestone and dolomite aggregates coated by asphalt binder (4.6% by weight) up to 3-mm in thickness (Fig. 2.1).

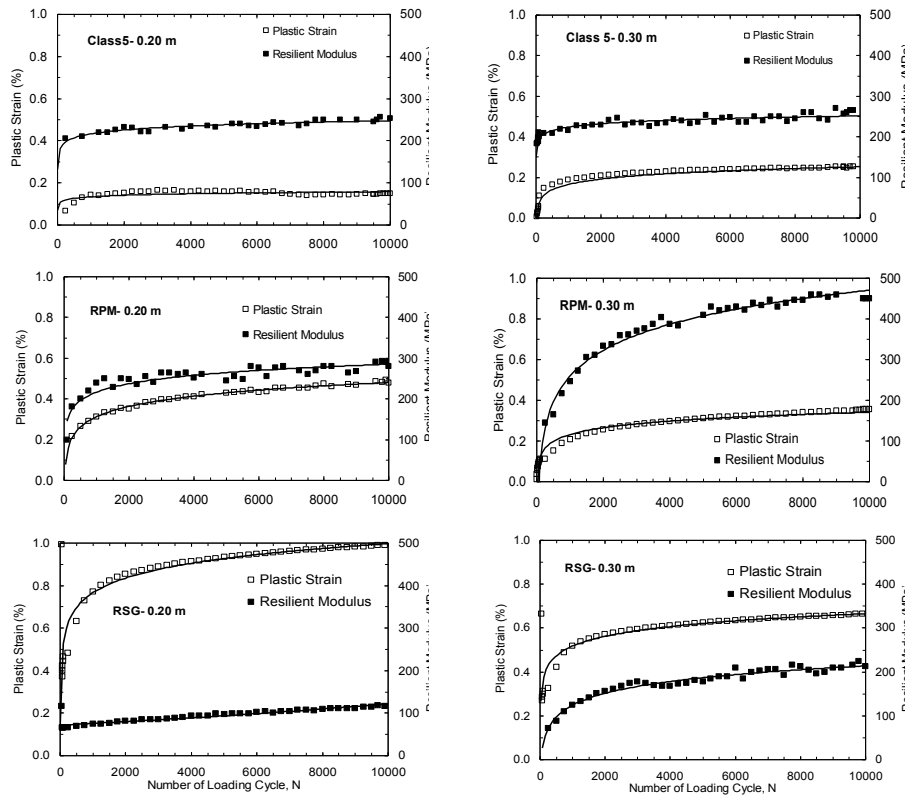


Figure 2.4 Plastic strain and resilient modulus vs. number of load cycles for (a) Class 5, (b) RPM, and (c) RSG with thickness of 0.2 (left) and 0.3 m (right)

Plastic strain and resilient modulus of RPM and RSG stabilized with 10% fly ash (i.e., SRPM and SRSG) are shown in Fig. 2.5 as a function of number of loading cycles. Four LSME test sequences of 10,000 cycles each were conducted on each material, with 7 day of curing between tests. The resilient modulus increases with increasing curing time for both the SRPM and SRSG. The SRPM exhibits a small and near constant rate of plastic strain after approximately 4000 cycles, and the SRSG exhibits a constant and very small plastic strain (< 0.1%). Mohammad et al. (26) also report small plastic strains for recycled foamed asphalt and blended calcium sulfate (BCS) stabilized with fly ash and slag.

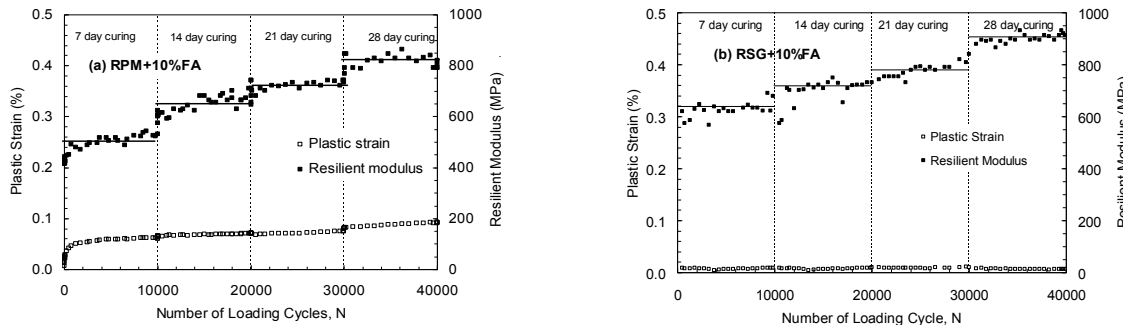


Figure 2.5 Permanent deformation and resilient modulus versus the number of load cycles for (a) RPM and (b) RSG stabilized with fly ash (0.3 m thicknesses)

Lower plastic strains generally are associated with the materials having higher resilient modulus (8). The largest plastic strains are associated with the RPM and RSG, even though these materials have similar resilient modulus or even higher than the Class 5 base. The higher plastic strain is attributed to viscous creep associated with the asphalt in the RPM and the fines in the RSG. In contrast, the SRPM and SRSG have the lowest plastic strains and the highest resilient moduli. Binding by the self-cementing fly ash reduces creep in the RPM and RSG appreciably, which is also evident when Figs. 4 and 5 are compared. Strong binding of aggregates of the RPM and RSG with fly ash increases through creation of needle-shape ettringite during the curing time, as shown in Fig. 2.6. The binding of aggregates is expected to reduce the plastic and elastic deformation of stabilized materials under traffic loading.

Materials with high resilient modulus such as RPM can provide a stiffer foundation for the pavement structure. However, the cumulative permanent deformation of unstabilized RPM and RSG under traffic loading is higher than conventional natural aggregate. Thus, excessive rutting may be encountered in flexible pavements that employ RPM or RSG in lieu of conventional base course materials. Rutting similar or less than that obtained with conventional base course can be expected using RPM or RSG stabilized with cementitious fly ash (8).

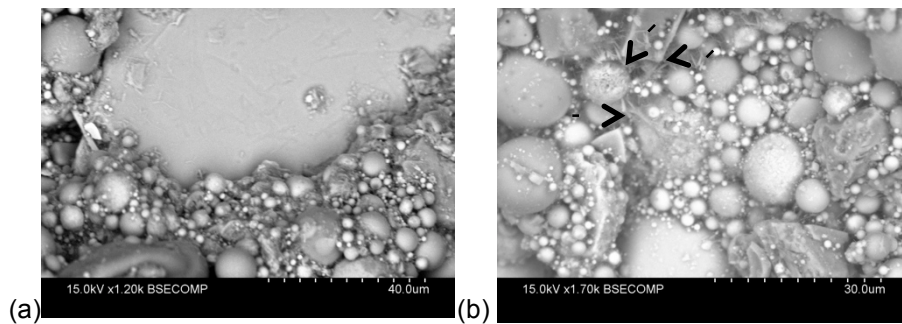


Figure 2.6 RSG particle surrounded by the fly ash (a), development of needle-shape ettringite (pointed by arrows) around the fly ash and RSG particles (b)

### 2.5.2 Resilient Modulus from BSRM Test

The BSRM tests indicated that resilient modulus of materials without fly ash stabilization increases with the bulk stress (i.e.,  $k_2 > 0$ ). Class 5 base has parameter  $k_2$  equal to 0.53, which is in the typical range for the granular materials (23). RPM has lower  $k_2$  ( $= 0.34$ ) indicating lower stress dependency on bulk stress. RSG has  $k_2 = 0.44$ , intermediate between RPM and Class 5 base, reflecting the effect of fines content compared to Class 5 (i.e., less sensitive to the bulk stress than Class 5), as described by Huang (23). The behavior of materials with high fines content is more controlled by cohesive forces between fine particles rather than external forces (i.e., confining stress). For the stabilized materials with fly ash, the resilient modulus is not dependent on bulk stress ( $k_2 \approx 0$ ) in the range of the applied bulk stresses due to the strong cementation between particles, as illustrated in Fig. 2.6. For fly ash stabilized materials, the chemical bonds between particles due to the development of ettringite (Fig. 2.6) prevail over the interparticle friction and thus stress dependency of the resilient modulus. Therefore, the stress and strain levels do not affect the resilient modulus and plastic deformation of SRPM and SRSG in the pavement, unless fatigue cracking takes place.

### 2.5.3 Comparison between the LSME and BSRM Test results

The SRM of base course materials backcalculated from the LSME and calculated from the BSRM test are shown in Fig. 2.7. The SRM of the Class 5 base, RPM, and RSG from the BSRM test was smaller than those obtained from the LSME. The difference in the resilient moduli of unstabilized materials is attributed to the interplay of the strain amplitude in the two test methods. Tanyu et al. (20) indicated that the resilient modulus of granular materials backcalculated from the LSME tend to be higher than those from the BSRM tests. In this study, the SRM of unstabilized materials from the LSME is 1 to 1.5 times as high as that from the BSRM test. This difference was expected by the difference in strain amplitude between two tests (20). In contrast, the SRM from the BSRM test on the SRPM and SRSG was consistently 3 to 5 times higher than that from the LSME, i.e., the opposite of general behavior for granular materials. This is attributed to the mixing and curing conditions associated with fly ash stabilized

materials as reported in several investigations (2, 10, 16). There was more thorough mixing and controlled curing in the BSRM test at 25° and 100% humidity, which was not feasible to achieve in the LSME. During the LSME test, temperature varied from 25° to 30°C and humidity was between 70 to 80%. It appears that the effect of mixing and curing conditions is stronger than the effect of strain amplitude on the resilient modulus of SRPM and SRSG.

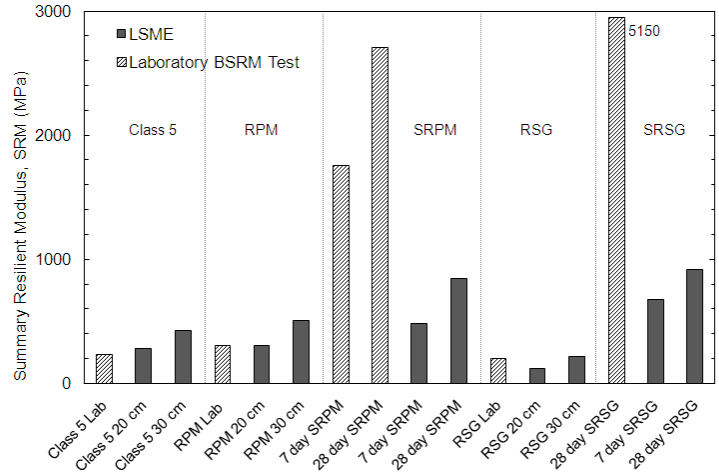


Figure 2.7 Summary resilient modulus (SRM) from the LSME and laboratory BSRM test

Generally, strain dependency of modulus of granular materials can be studied through the backbone curve developed by Hardin and Drnevich (27). The resilient moduli of the recycled materials from the LSME and BSRM tests were normalized with respect to the low strain Young’s modulus from the seismic tests ( $E_s$ ), as shown in Fig. 2.8. The  $E_s$  was calculated as described by Schuttpelz et al. (19):

$$E_s = V_p^2 \rho \frac{(1+\nu)(1-2\nu)}{(1-\nu)} \quad (\text{Eq. 2.3})$$

where  $V_p$  = P-wave velocity calculated from the seismic testing,  $\rho$  = mass density, and  $\nu$  = Poisson’s ratio (see Table 2.2).

Seismic tests were conducted using micro electromechanical systems (called “MEMS”) buried in various depths of the compacted base course materials in the LSME to measure the travel time of the seismic waves transmitted from the surface of materials and generated by a hammer impact. Low strain Young’s modulus ( $E_s$ ) was in the range of shear strain  $< 10^5$ . Increasing shear strain in the materials decreases the normalized resilient modulus. As shown in Fig. 2.8, the same stress level in the LSME and BSRM test (confining stress of 45 kPa) resulted in different strain levels due to the scale effect.

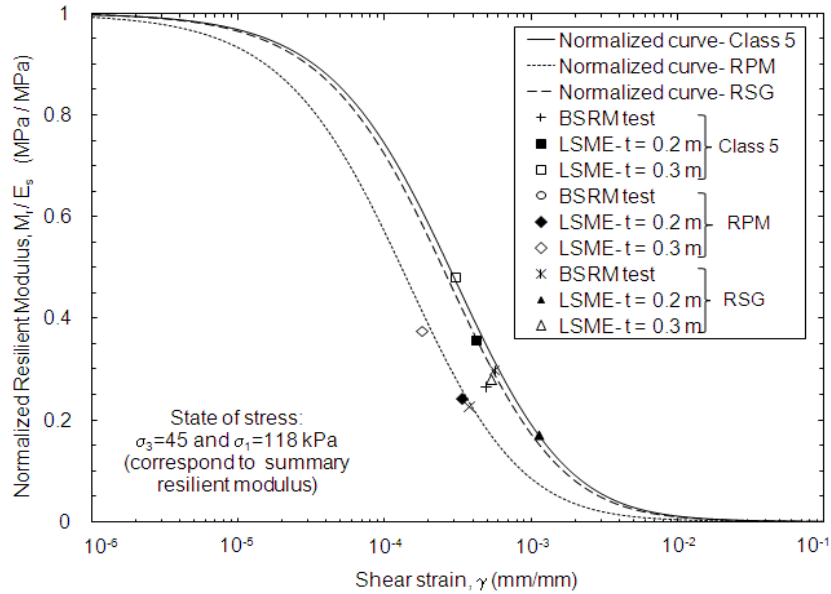


Figure 2.8 Strain dependency of the resilient modulus of recycled materials from the BSRM test and LSME

Fig. 2.9 shows the relationship between layer thickness of base course and SRM obtained from the LSME. The  $M_r$  corresponding to typical base course thicknesses other than 0.20 m and 0.30 m tested in the LSME were predicted using the backbone curve calibrated with the LSME (Benson et al. (22)). For the unstabilized base materials, SRM is consistently higher for thicker base course layers. The increase in modulus from 0.2 to 0.3-m thick bases is 65, 50, and 95% for Class 5, RPM, and RSG, respectively. The thickness-dependency of SRM is due to the lower shear strain amplitude in thicker layers for the same surface load.

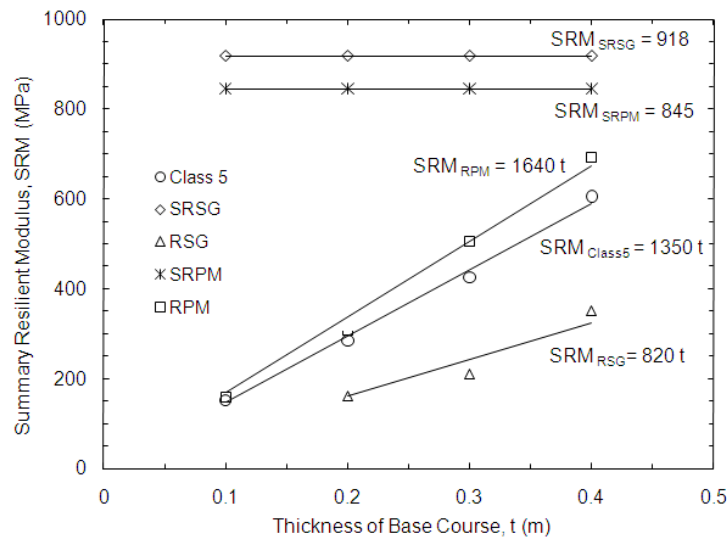


Figure 2.9 Summary resilient modulus (SRM) of Class 5 base, RPM, RSG, SRPM, and SRSG as a function of base course thickness

## 2.6 DESIGN APPROACHES FOR USE OF RECYCLED MATERIALS IN PAVEMENT STRUCTURES

Design method of flexible pavement structures may vary among agencies and countries. In this study, the SRM and plastic deformation obtained from the LSME was used to study two design

approaches: 1. an equivalency-based design using AASHTO-1993 design guide (28) and 2. lifetime expectancy of pavements using the Mechanistic Empirical Pavement Design Guide (MEPDG (29)). The LSME results are assumed to be representative mechanical properties of the base course materials due to the scale effect, layer thickness, and mixing and curing method which are similar to the field conditions.

### 2.6.1 Equivalency-Based Design Using AASHTO 1993

Equivalency-based design was developed based on the premise of generating a pavement structure constructed with alternative recycled base course materials that have the equivalent structural capacity as the pavement constructed with conventional base course materials. AASHTO-1993 (28) Guide for Design of Pavement Structures uses structural number (SN) to assess the structural capacity and contribution of each pavement material on the service life of pavements. Two main factors control the SN of the base course according to the AASHTO 1993: (1) layer thickness and (2) layer coefficient reflecting stiffness of base course (function of the SRM). The SN of the entire pavement is defined as the summation of the SN of each pavement layer (AASHTO 1993),

$$SN = SN_1 + SN_2 m_2 + SN_3 m_3 = b_1 t_1 + b_2 t_2 m_2 + b_3 t_3 m_3 \quad (\text{Eq. 2.3})$$

where  $m_i$  is the drainage modification factor (assumed equal to 1 in this study),  $b_i$  is the layer coefficient and  $t_i$  is the thickness (inches) of the layer  $i$  ( $i=1$  asphalt,  $i=2$  base course,  $i=3$  subbase). The layer coefficient ( $b_2$ ) of a granular base course is empirically related to resilient modulus (28) as given in Eq. 2.4.

$$b_2 = 0.249 \log SRM - 0.977 \quad (\text{Eq. 2.4})$$

where SRM is the summary resilient modulus of the granular base material (in pounds per square inch). Base course material stabilized with fly ash was also assumed to follow Eq. 2.4. The layer coefficients ( $b_2$ ) of the tested materials were calculated using Eq. 2.4 by employing the SRM from the LSME (Fig. 2.9). Layer coefficients of the tested materials are presented in Fig. 2.10. For example, the layer coefficient of 0.3-m-thick RPM is 0.2, while that of 0.2-m-thick RPM is 0.17. The layer coefficient of materials stabilized with fly ash is 0.3, which indicates a significantly higher structural capacity as a base course. The SRM of the materials without fly ash varies with thickness, and therefore, their layer coefficient is dependent on the layer thickness. The layer coefficient of SRPM and SRSG does not vary with the base course thickness due to constant SRM of these materials with changing thickness. The layer coefficient of tested recycled materials is within the typical range of layer coefficients presented in AASHTO-1993 (28) for base course layers.

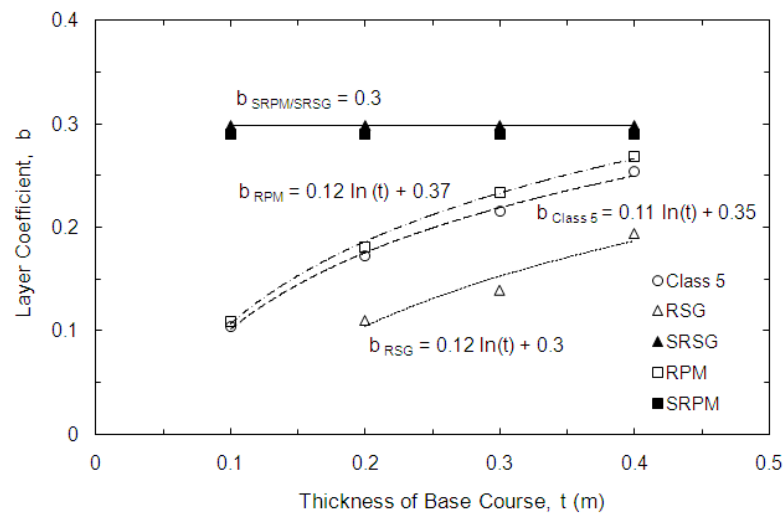


Figure 2.10 Layer coefficients for Class5 base, RPM, RSG, SRPM, and SRSG as a function of base course thickness

The layer coefficients presented in Fig. 2.10 can be directly applied to the design of flexible pavements. However, an equivalency design approach was developed as a design tool to correlate the required thickness of alternative recycled materials relative to that of the conventional base course aggregate. Because designers, in general, have direct experience of what thickness of natural aggregate base is required in most cases, this approach gives them a simple tool in dealing with recycled base materials. The equivalency-based design equates the SN of a pavement having an alternative recycled base course to that of a pavement constructed with selected, acceptable quality aggregate base. MnDOT's Class 5 base (30) was used as the selected standard base material. To make the equivalency, the structural number of base course consisting of alternative recycled material ( $SN_r$ ) was set equal to the structural number of conventional base course material ( $SN_c$ ). The SN of a pavement structure, involving the conventional and the alternative recycled base materials, is calculated,

$$SN_c = b_1 t_1 + b_c t_c \quad (\text{Eq. 2.5})$$

$$SN_r = b_1 t_1 + b_r t_r \quad (\text{Eq. 2.6})$$

where the subscript "c and r" denotes the conventional and the alternative recycled base course materials (Fig. 2.11). If the HMA thickness and properties are assumed to be the same for the two pavement configurations, the relationship between thicknesses and layer coefficients for the conventional and alternative recycled base materials is presented as

$$\frac{b_r}{b_c} = \frac{t_c}{t_r} \quad (\text{Eq. 2.7})$$

Knowing that the layer coefficient is a function of SRM, the thickness ratio of the conventional and the alternative recycled material is given by substituting Eq. 2.4 in Eq. 2.7:

$$\frac{t_r}{t_c} = \frac{0.249 \log SRM_c - 0.977}{0.249 \log SRM_r - 0.977} \quad (\text{Eq. 2.8})$$

Eq. 2.8 requires that the SRM of Class 5 base course and the alternative recycled materials as input to determine the ratio between the thickness of the conventional base course and alternative recycled material ( $t_c / t_r$ ). The relationship between SRM and thickness in Fig. 2.9 can be used in Eq. 2.8. The ratio ( $t_c / t_r$ ) was used to develop a design graph for use of alternative recycled materials as a base course, as shown in Fig. 2.12.

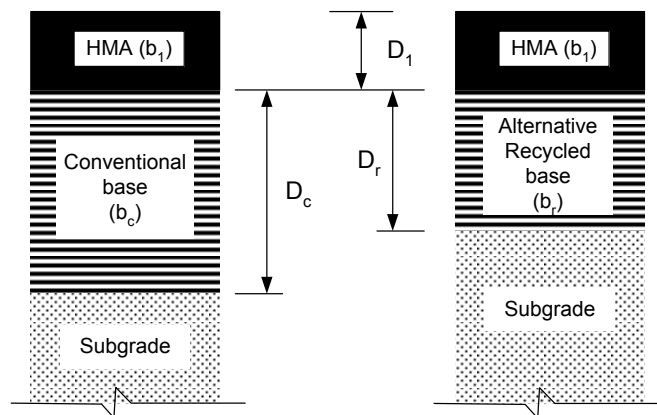


Figure 2.21 Schematic pavement profiles for equivalency based design between conventional and alternative recycled base course materials

Fig. 2.12 exhibits the relationship between the thickness of alternative recycled materials and that of Class 5 base. For example, the RPM has nearly an equivalent thickness to Class 5 base in a pavement structure. A thicker layer of RSG is required to obtain a base equivalent to the Class 5 base. Use of fly ash stabilization improves the structural capacity of the RPM and RSG and results in thinner equivalent base course layer. A 0.22-m-thick SRPM or SRSG is equivalent to a 0.3-m-thick Class 5 base. Use of SRPM and SRSG reduces the base course thickness up to 30% in roadway construction. Fig. 2.12 is a quantitative design tool for use of recycled materials with and without fly ash stabilization in roadway constructions.

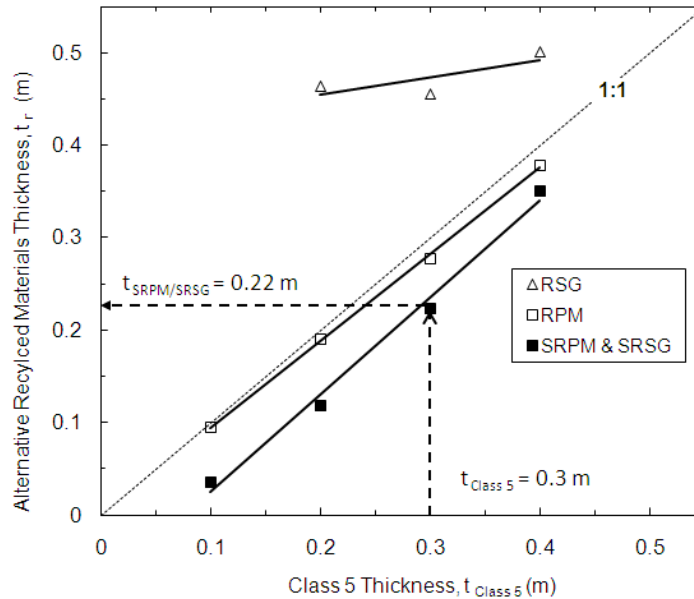


Figure 2.32 Alternative recycled material thickness as a function of Class 5 thickness

### 2.6.2 Equivalency-Based Design Using MEPDG

AASHTO-1993 (28) method does not include the effect of plastic deformation of base course in the design scope, whereas the effect of plastic deformation of base course materials can be accounted in the Mechanistic Empirical Pavement Design Guide (MEPDG (29)). The MEPDG and related software provide capabilities for the analysis and performance prediction of different types of flexible and rigid pavements. The MEPDG uses mechanistic-empirical numerical models to analyze input data for traffic, climate, materials, and proposed structure. The model estimate damage accumulation over the predicted service life.

In this study, the SRM and plastic deformation obtained from the LSME were used in the MEPDG code to predict the rut depth and international roughness index (IRI) of the pavement. The calibration factor ( $B_{s1}$ ) in the Table 2.3 was determined by matching the plastic deformation from the LSME with the predicted one from the MEPDG code. The rut depth and IRI were determined in pavement structures consisting of various base course materials (i.e., Class 5, RPM, RSG, and SRPM/SRSG). The material properties and geometry of HMA and subgrade layers remained constant. Subgrade was modeled with modulus of 70 MPa. The traffic, environment, and material properties were input into the MEPDG design program, as presented in Table. 2.3. Average annual daily truck traffic (AADTT) was chosen 4000.

The service life of the pavement structure constructed with RSG, RPM, and SRPM/SRSG by limiting the rut depth to 12.7 mm (23) is shown in Fig. 2.13a. The service life of the pavement structure by limiting the IRI to 2.7 m/km (MEPDG 2004) is shown in Fig. 2.13b. The life of the pavement built by 0.3-m-thick Class 5 and RPM is 17 years for the limiting IRI = 2.7 m/km and 12 years for the limiting rut depth = 12.7 mm. The MEPDG results showed that the rutting criterion is more critical than the IRI criterion for predicting the service life of the pavements.

Considering the IRI criterion of limiting roughness to 2.7 m/km in Fig. 2.13b for estimating the pavement life, the pavement built with 0.2-m-thick RPM and Class 5 base has a service life of 13 years

that is similar to the pavement built by 0.3-m-thick RSG base. Based on the MEPDG design program, using 0.3-m-thick SRPM/SRSG base instead of 0.3-m-thick Class 5/RPM base increases the service life of the pavement structure from 17 to 21 years.

Comparing the results achieved from AASHTO-1993 (28) and MEPDG (29), adequate properties of pavement materials are necessary to design a pavement with alternative recycled materials in lieu of the conventional base course aggregates. The structural capacity (i.e., SRM) and long term performance (i.e., plastic deformation) of alternative materials should be studied thoroughly for pavement design procedures. For example, in accordance to AASHTO-1993 (28), the SRPM/SRSG with 0.22-m thickness

Table 2.3 Input parameters for MEPDG program

Traffic	Initial Two-way	4000 AADTT		
	Number of Lanes	2		
	Operation Speed	110 km/hr		
	Dual Tire Spacing	0.3 m		
	Tire Pressure	800 kPa (120 psi)		
Environment	I-94 Minnesota -USA			
<b>Asphalt Binder</b> Superpave Binder Grading	Thickness	0.1 m		
	A	10.98		
	VTS	-3.6		
<b>Base Course</b> A-1-a	Thickness	0.3 m		
	Modulus	From LSME, presented in Fig. 2.9		
<b>Subgrade</b>	Thickness	0.5 m		
	Modulus	70 MPa		
Rutting for Granular Materials				
Rutting Calibration Factor	RSG	RPM	Class 5	SRPM/SRSG
$B_{s1}$	1.7	1.35	1	0.1

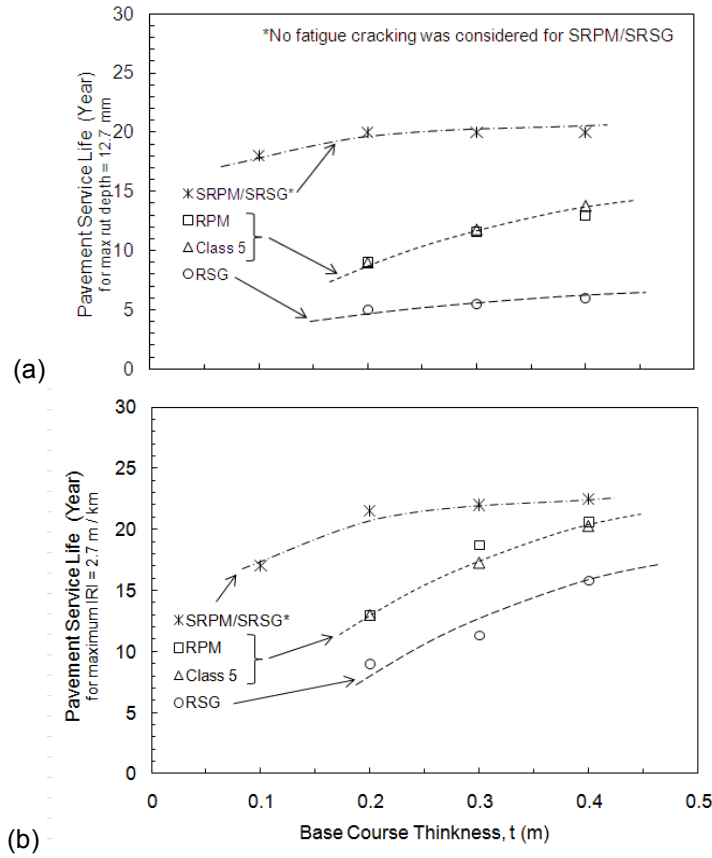


Figure 2.13 Life time expectancy of pavement structure built by conventional and alternative base course materials for limited rut depth (a) and IRI (b) from the MEPDG code is equivalent to the 0.3-m-thick RPM or Class 5 base. However the SRPM/SRSG with 0.1-m thickness is equivalent to the 0.3-m-thick RPM or Class 5 aggregate, based on the MEPDG (29) analysis. Note that fatigue cracking and potential modulus degradation was not considered in the MEPDG and AASHTO 1993 analysis for the stabilized recycled roadway materials. Therefore, the design method for use of stabilized materials should be used with cautions.

## 2.7 CONCLUSIONS

Large-scale model experiments (LSME) and standard bench-scale resilient modulus (BSRM) tests were conducted on base course materials consisting of recycled pavement material (RPM), reclaimed road surface gravel (RSG), and conventional Class 5 base from Minnesota. The RPM and RSG were tested alone and with fly ash stabilization. Based on the findings of this study, the following conclusions are made:

1. Summary resilient moduli (SRM) obtained from the LSME and BSRM tests showed that RSG has the lowest SRM, the RPM the highest, and the Class 5 gravel in between. Stabilization of the RPM and RSG with 10% by weight of self-cementing fly ash increased the SRM significantly.
2. The SRM of unstabilized base course materials backcalculated from the LSME was dependent on layer thickness and higher than that from the BSRM tests. This difference is explained by the differences in strain amplitudes induced in each method.
3. In fly ash stabilized materials, the SRM backcalculated from the LSME was smaller than that from the BSRM tests. This difference is attributed to more thorough mixing and curing procedure in the BSRM tests compared to the LSME.
4. Plastic deformation behavior of materials obtained from the LSME indicated that the RPM and RSG have higher potential for accumulating plastic deformation during the service life of pavement system

compared to the natural aggregate and stabilized RPM and RSG (SRPM and SRSG), which exhibit negligible plastic deformations.

5. Material properties (i.e., resilient modulus and plastic strain) obtained from the LSME are considered to be more representative for the base course materials and more similar to the field conditions. Therefore, they were used to develop design methodology for use of recycled base materials.
6. Layer coefficients of the unstabilized granular base materials are not constant but increase with thickness. The layer coefficients for RSG and RPM are in the range of 0.1-0.2 and 0.1-0.25 depending on layer thickness (0.1 to 0.4m). The SRPM and SRSG have a layer coefficient of 0.3, which is independent of layer thickness. Stabilization of recycled materials can reduce the required thickness of the base course up to 30% based on the AASHTO 1993 design guide.
7. The lifetime expectancy of test materials predicted by the MEPDG code showed that not only the resilient modulus but also the plastic deformation of alternative recycled materials is essential for comprehensive design procedure when alternative materials are used. The results showed that stabilization of recycled materials with fly ash increases the lifetime of pavements constructed with 0.3-m-thick alternative recycled materials from 17 to 21 years.

### **ACKNOWLEDGMENT**

The Minnesota Local Roads Research Board (LRRB) and the Recycled Materials Resource Center (RMRC) provided partial financial support for this study. Xiaodong Wang and William Lang at the University of Wisconsin-Madison assisted with the LSME. Brian Kootstra assisted in the experiments.

### **REFERENCES**

1. Epps, J. A. *Cold-Recycled Bituminous Concrete Using Bituminous Materials*. NCHRP Synthesis of Highway Practice 160, NCHRP, Washington DC, 1990.
2. Wen, H. and Edil, T. B. (2009). Sustainable Reconstruction of Highways with In-situ Reclamation of Materials Stabilized for Heavier Loads, *Proc. 2<sup>nd</sup> Int. Conf. on Bearing Capacity of Roadway, Railways and Airfields*, Urbana-Champaign, IL, on CD-ROM.
3. Lee, J. C., Edil, T. B., Tinjum, J. M. and Benson, C. H. A Quantitative Assessment for Environmental and Economic Benefits of Using Recycled Materials in Highway Construction, *Transportation Research Record*, No. 2158, Transportation Research Board, National Research Council, Washington DC, 2010, 138-142.
4. Taha, R. Evaluation of Cement Kiln Dust-Stabilized Reclaimed Asphalt Pavement Aggregate Systems in Road Bases. *J. of Trans. Res. Rec.*, No. 1819, Transportation Research Board, Washington, DC, 2003, 11-17.
5. Cooley, D. Effects of Reclaimed Asphalt Pavement on Mechanical Properties of Base Materials. *MS Thesis*, Brigham Young University, Provo, UT, 2005.
6. Kim, W., Labuz, J., Dai, S. Resilient Modulus of Base Course Containing Recycled Asphalt Pavement, *J. of Trans. Res. Board*, No. 1981, Transportation Research Board, Washington, DC, 2007, 27-35.
7. Mohammad, L. N., Herath, A., Rasoulia, M. and Zhongjie, Z. (2006). Laboratory Evaluation of Untreated and Treated Pavement Base Materials: Repeated Load Permanent Deformation Test, *J. of the Trans. Res. Board*, No. 1967, Transportation Research Board, Washington, DC, 78-88.
8. Kootstra, B. R., Ebrahimi, A., Edil, T. B., and Benson, C. H. Plastic Deformation of Recycled Base Materials, *Proc. GeoFlorida 2010*, Advances in Analysis, Modeling and Design, ASCE Geo Institute, GSP 199, West Palm Beach, FL, 2682-2691
9. Edil, T. B., Benson, C., Bin-Shafique, M., Tanyu, B., Kim, W. and Senol, A. Field Evaluation of Construction Alternatives for Roadways over Soft Subgrade, *J. of Trans. Res. Board*, No. 1786, Transportation Research Board, Washington, DC, 2002, 36-48.
10. Bin-Shafique, S., Edil, T. B., Benson, C. H. and Senol, A. Incorporating a Fly-Ash Stabilized Layer into Pavement Design. *Geotechnical Engineering-ICE*, 157 (GE4), 2004, 239-249.
11. Li, L., Benson, C. H., Edil, T. B. and Hatipoglu, B. Sustainable Construction Case History: Fly Ash Stabilization of Recycled Asphalt Pavement Material, *Geotechnical and Geological Engineering*, 2008, Vol. 26, No. 2, pp. 177-188 (also TRB Paper 07-0914).
12. Edil, T. B., Acosta, H. A. and Benson, C. H. Stabilizing Soft Fine-Grained Soils with Fly Ash. *J. of Mat. in Civil Eng.*, 18(2), 2006, 283-294.

13. Senol, A., Edil, T. B., Bin-Shafique, M. S., Acosta, H. A., Benson, C. H. Soft Subgrades' Stabilization by Using Various Fly Ashes, *Resources Conservation and Recycling*, 46(4), 2006, 365-376.
14. Wen, H., Tharaniyil, M., Ramme, B. and Krebs, U. Field Performance Evaluation of Class C Fly Ash in Full-depth Reclamation: Case History Study, *J. of Trans. Res. Board*, No. 1869, Transportation Research Board, Washington, DC, 2004, 41-46.
15. Wen, H., Warner, J., Edil, T. B. and Wang, G. Laboratory Comparison of Crushed Aggregate and Recycled Pavement Material With and Without High Carbon Fly Ash, *Geotechnical and Geological Engineering*, 28(4), 2010, 405-411.
16. Hatipoglu, B., Edil, T. B., and Benson, C. H. Evaluation of Base Prepared from Road Surface Gravel Stabilized with Fly Ash, *ASCE Geo. Special Publication*, 177, 2008, 288-295.
17. Camargo, F. F., Edil, T. B., Benson, C. H. Strength and Stiffness of Recycled Base Materials Blended with Fly Ash, *Proc. 88<sup>th</sup> Annual Meeting*, CD-ROM, 09-1971, National Research Council, Washington DC, 2009.
18. Crovetti, J. Construction and Performance of Fly Ash-Stabilized Cold In-place Recycled Asphalt Pavement in Wisconsin, *J. of Tran. Res. Board*, No. 1730, Transportation Research Board, Washington, DC, 2000, 161-166.
19. Schuettpeiz, C. C., Fratta, D., and Edil, T. B. Mechanistic corrections for determining the resilient modulus of base course materials based on elastic wave measurements. *Journal of Geotechnical and Geoenvironmental Engineering*. Vol. 136, No. 8, 2010, 1086-1094
20. Tanyu, B. F., Benson, C. H., Edil, T. B., and Kim, W. Equivalency of Crushed Rock and Three Industrial By-products Used for Working Platforms During Pavement Construction, *J. of Trans. Res. Rec.*, No.1874, Trans. Research Board, Washington, DC, 2004, 59-69.
21. Harichandran, R. S., Baladi, G. Y., Yeh, M. Development of a Computer Program for Design of Pavement Systems Consisting of Bound and Unbound Materials, Dept. of Civil and Envir. Eng., Michigan State University, Lansing, Michigan, 1989.
22. Benson, C. H., Edil, T. B., Ebrahimi, A., Kootstra, R. B., Li, L., and Bloom, P. *Use of Fly Ash for Reconstruction of Bituminous Roads: Large Scale Model Experiments*, Minnesota Department of Transportation, St Paul, MN, 2009. ([http://www.recycledmaterials.org/Research/current/project\\_47/project\\_47\\_final\\_report.pdf](http://www.recycledmaterials.org/Research/current/project_47/project_47_final_report.pdf))
23. Huang, Y. *Pavement analysis and design*, Prentice-Hall, Inc., Englewood Cliffs, New Jersey, 2003.
24. Werkmeister, S., Dawson, A. R., and Wellner, F. Permanent Deformation Behavior of Granular Materials and the Shakedown Concept, *J. of the Trans. Res. Board*, No. 1757, Transportation Research Board, Washington, DC, 2001, 75-81.
25. Yang S. R., Huang. W. H., and Liao. C. C. Correlation Between Resilient Modulus and Plastic Deformation for Cohesive Subgrade Soil Under Repeated Loading, *J. of the Trans. Res. Board*, No. 2053, Transportation Research Board, Washington, DC, 2008, 72-79.
26. Mohammad, L. N., Herath, A., Rasoulia, M. and Zhongjie, Z. Laboratory Evaluation of Untreated and Treated Pavement Base Materials: Repeated Load Permanent Deformation Test, *J. of the Trans. Res. Board*, No. 1967, Transportation Research Board, Washington, DC, 2006, 78-88.
27. Hardin, B. O., and Drnevich, V. P. Shear Modulus and Damping in Soils: Design Equations and Curves. *J. Soil Mech. and Found. Div.*, 98, SM7, 1972, 667-692.
28. *AASHTO Guide for Design of Pavement Structures*, American Association of State Highway and Transportation Officials, Washington DC, 1993.
29. NCHRP 1-37A. *Mechanistic-empirical design method for the structural design of new and rehabilitated pavement structures*. Final Report for NCHRP 1-37A, National Cooperative Highway Research Program, Washington, DC, 2004.
30. MnDOT. *Standard Specifications for Construction*, MnDOT, St. Paul, MN, 2005.

## **CHAPTER 3: LARGE-SCALE, CYCLIC TRIAXIAL TESTING FOR MEASURING THE DEFORMATION OF FOULED RAILWAY BALLAST**

### **3.1 ABSTRACT**

Large-scale, cyclic triaxial (LSCT) equipment and testing protocol were developed to measure plastic deformation of fouled railway ballast, including the preparation of fouled ballast specimens and representative loading conditions. A testing protocol for fouled ballast was developed due to the lack of testing guidelines in the literature and in rail engineering practice. To account for the size of ballast particles, specimen size of 300-mm length and 610-mm height was used. Finite element analysis (FEA) was used to determine a representative state of stress in railway ballast for LSCT testing (i.e., confining ( $\sigma_3$ ) and cyclic ( $\sigma_d$ ) stress, pulse shape, and loading frequency). Confining stress was varied between 20 to 200 kPa, and  $\sigma_d$  between 50 to 300 kPa. A haversine, bell-shaped loading pulse simulated the traffic loading on ballast, with a frequency varying between 5 and 20 Hz. A prototype full-scale track model experiment (FSTME) was developed to find a representative state of stress for railway ballast of  $\sigma_3 = 90$  kPa and  $\sigma_d = 300$  kPa in the LSCT. This stress was then used to study the impact of fouling on the deformational behavior of ballast. The method of introducing fouling material and moisture to the ballast was critical to the deformational behavior. Introduction of fouling material at higher moisture content to ballast can create heterogeneous and layered mixtures without proper control. Adding fouling material with already-compacted ballast resulted in smaller plastic deformation (20 to 50%) than mixing fouling material with ballast prior to compaction. To simulate the field conditions and tamping activities in the ballast layer, ballast is recommended to be mixed with relatively dry fouling materials prior to compaction to prevent layered mixtures. This study introduces fundamental guidelines for testing fouled railway ballast using the LSCT equipment. Deformational behavior of railway ballast in various fouling conditions was determined using the proposed testing protocol and show fouling and moisture increases the accumulation of plastic deformation in railway ballast under cyclic traffic loading.

### **3.2 INTRODUCTION**

Railways are an essential component of a multi-modal, freight transport network. Increasing volume, tonnage, and speed of rail systems are stressing rail substructure (Fig. 3.1) to levels not-yet evaluated or considered in depth (Lee 2009). Railway ballast provides the primary structural support for track structure and facilitates effective track maintenance, such as track leveling. Ballast is typically specified as angular, large ( $< 75$  mm) particles with a mineralogically and chemically sound composition; however, the mechanical behavior of the ballast deteriorates during the service life of rail track due to particle breakage and increasing fines (i.e., ballast 'fouling'). The structural integrity of highly fouled ballast is compromised and can lead to track instability and, ultimately, train derailments (Selig and Waters 1994; Raymond and Bathurst 1994). Fouling impacts the track performance by changing the mechanical properties of substructure layers through (1) loss of effective drainage, (2) formation of "mud-holes", (3) lack of resistance to lateral and longitudinal forces, (4) poor durability after maintenance, and (5) increasing rate of deterioration (Haque et al. 2008; Zaayma 2006; Liu and Xiao 2010); therefore, costly ballast maintenance activities, such as undercutting, tamping, shoulder cleaning, or ballast replacement, are routinely performed by railway companies. In current freight capacity, maintenance of rail track and tamping costs about \$500M annually for 150,000 km of Class1 track (\$3,800/km/yr, Christmer and Davis 2000). The impact of increasing freight loads on lifecycle of a railway track is unknown without proper investigation, characterization, and study of substructure material, primarily railway ballast.

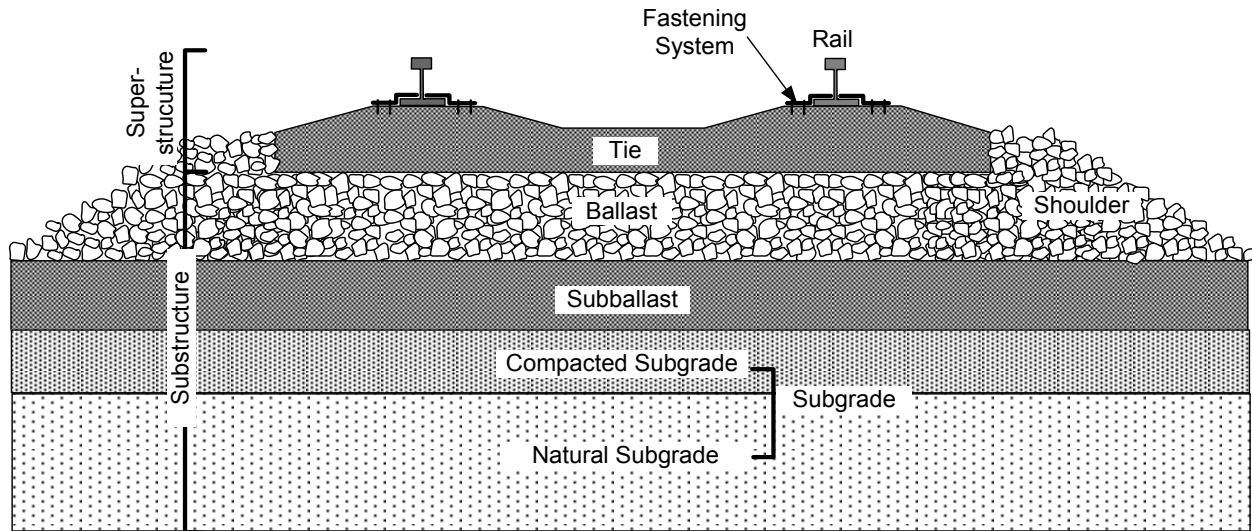


Figure 3.1 Typical Components of Substructure and Superstructure in a Railway Track

Currently, few US-based research institutions participate in rail substructure research, and publications in this area are limited. A logical first step in modeling the deformational behavior of railway ballast is to develop standards and uniform protocol for laboratory equipment that adequately characterizes the performance of railway ballast under a variety of environmental and structural load situations.

### 3.2.1 Mechanistic-Based Evaluation of Railway Ballast

The mechanical properties of railway ballast (e.g., plastic deformation, resilient or elastic deformation, and particle deterioration or crushing) continually change during the service life of ballast due to moisture variation, loading condition, and the generation and accumulation of fouling materials (Fig. 3.2). The mechanical properties of geo-materials have been historically determined in accordance with ASTM D3999 (Determination of the Modulus and Damping Properties of Soils Using the Cyclic Triaxial Apparatus) and ASTM D5311 (Load Controlled Cyclic Triaxial Strength of Soil) using monotonic and cyclic triaxial testing. For highway sub-pavement material, 'resilient modulus' testing (NCHRP 1-28a, 2003) is typically performed with a 100-mm-diameter specimen for finer subgrade materials and a 150-mm-diameter specimen for base course aggregates. For railway ballast, cyclic and monotonic triaxial testing with 300-mm-diameter and 600-mm-height specimens has been performed to determine the shear strength properties and deformational behavior of clean ballast (Indraratna et al. 2005; Anderson and Key 2000; Suiker et al. 2005; Aursudkij 2007). A review of the literature (Table 3.1) shows that deviator stress ( $\sigma_d$ ) within the railway ballast varies from 50 to 1200 kPa and confining stress ( $\sigma_3$ ) varies from 7 to 240 kPa. Loading repetitions up to 1M cycles with frequency of 5 to 20 Hz has been used in the ballast testing. Limited studies on strength properties and deformational behavior of ballast, specifically for fouled ballast, have not led to a standard testing method for railway ballast using the LSCT testing.

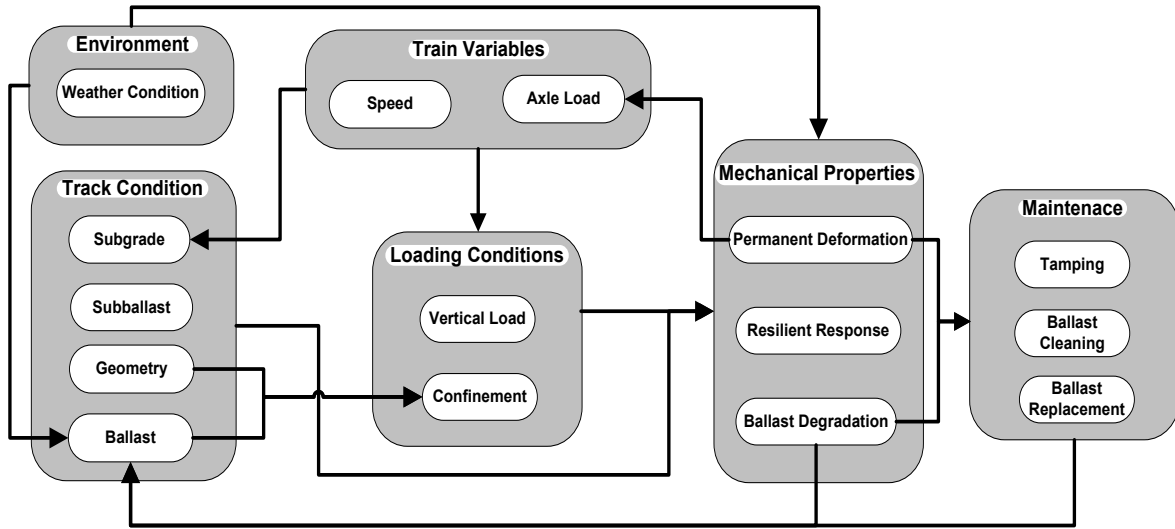


Figure 3.2 Interaction and Contributions of Environment, Track condition, and Loading on Deformational Behavior of Railway Substructure

Table 3.1 State of Stress, Load Frequency, and Specimen Size in Previous Studies of Railway Ballast

Source	Deviator Stress (kPa)	Confining Pressure, (kPa)	Frequency of loading, (Hz)	Number of cycles, N	Max particle size $d_{max}$ (mm)	Specimen Size: Diameter (D) x Height (H) (mm)	D/ $d_{max}$
Thompson (1976)	315	7 to 105	NR	NR	50	150 x 300	3
Sekine et al. (2005)	49, 98, 147	19.6	11	0.3 M	63	300 x 600	4.7
Suiker et al. (2005)	$\sigma_d/\sigma_{max} = 0.5, 0.82, 0.92, 0.97$	41, 69	5	1 M	38	357 x 645	7
Indraratna et al. (2005) Lackenby et al. (2007)	30 to 1200	8, 15, 30, 60, 90, 120, 240	15, 20	0.5 M	53	300 x 600	5.6
Aursudkij (2007)	q/p = 1.5, 2	30, 60, 90, 180	0.2 (Sinusoidal)	0.1 M	50	300 x 450	6
Anderson and Fair (2008)	300 to 900	40, 90, 140	0.16, 0.5 (Square)	1.8 M	50, 20	236 x 455	4.7
Sevi et al. (2009)	$\sigma_d/\sigma_{max} = 0.94$	20-80 (Using Back Pressure)	0.05	10,000	63.5	519 x 889	8

$\sigma_{max}$  = Failure normal stress from monotonic triaxial

q = Difference of principal stresses, p = mean principal stresses.

Critical parameters that have been established as impacting the performance and degradation of railway ballast include fouling level, moisture content, and state of stress. However; a systematic, standardized testing method (including equipment setup, specimen preparation, and loading conditions) for railway ballast has not been established in the profession.

### 3.3 OBJECTIVES

The objective of this research was to develop testing equipment and protocol to characterize the plastic deformation of fouled railway ballast in a manner that represents field conditions. A large-scale cyclic triaxial (LSCT) test was designed to investigate the deformational behavior of clean and fouled ballast including elastic and plastic deformation under rail traffic loading. The LSCT was equipped to perform cyclic testing (with capability of doing monotonic testing) at different confining stresses, cyclic stress, rates of loading or deformation, loading frequencies, pulse shapes, and drainage conditions. A protocol described herein includes specimen preparation and systematic testing steps.

### 3.4 MATERIALS

#### 3.4.1 Ballast

A sample of clean ballast from a quarry in Wyoming was provided by the BNSF Railroad Company. The particle size distribution of the ballast (in accordance with ASTM D6913) in comparison to American Railroad Engineering and Maintenance-of-way Association's (AREMA 2003) ballast specification #24 is slightly coarser (Fig. 3.3). The ballast has a maximum particle size of 63 mm and a minimum particle size of 25 mm. At maximum dry density, the clean ballast has void ratio ( $e_B$ )=0.62. Based on visual inspection of thin sections accompanied by X-ray diffraction (XRD), the ballast is 35% granitic and 45% rhyolitic.

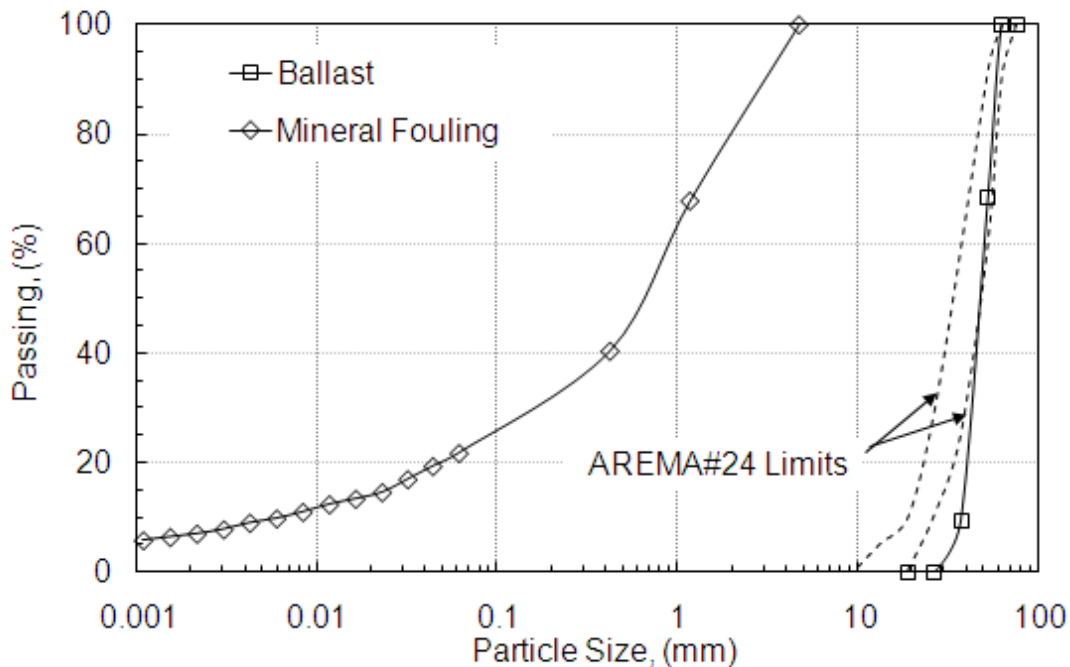


Figure 3.3 Particle Size Distribution of Ballast and Mineral Fouling (AREMA#24 is the Limits for a Standard Ballast, AREMA 2003)

### 3.4.2 Mineral Fouling Material

Mineral fouling due to subballast intrusion or ballast breakage was tested in this study. Mineral fouling was obtained by fractioning (< 4.75 mm) highly fouled ballast obtained from Wisconsin and Southern Railroad Company based on criteria established by Selig and Waters (1994). Selig and Waters (1994) defined the fouling index (FI) by summing % ballast fraction < 4.75mm and % ballast fraction < 0.075 mm (FI=P4+P200). Mineral fouling was 70% dolomitic and 30% quartzite, based on XRD analysis. The particle size distribution of mineral fouling is shown in Fig. 3.3.

## 3.5 METHOD DEVELOPMENT

### 3.5.1 Full-Size Track Model Experiment (FSTME)

A full-size track model experiment (FSTME) was used to find representative state of stress conditions for testing ballast in the LSCT test. The FSTME is a full-size, prototype rail substructure model, with dimensions of 0.6 m (wide) x 1.0 m (high) x 1.8 m (long), shown in Fig. 3.4. A typical tie spacing of 0.6 m was used and only half of the track width was simulated due to symmetry. The rail substructure in the FSTME consisted of (from the bottom up) soft subgrade, 0.3-m-thick subballast (with maximum grain size of 20 mm), and 0.3-m-thick clean ballast. A soft subgrade was simulated with blocks of Styrofoam with a modulus of elasticity,  $E$ , of 100 MPa. Subballast was compacted with a plate compactor to 100% maximum dry unit weight ( $\gamma_d = 19.8 \text{ kN/m}^3$  per standard Proctor, ASTM D698) and optimum water content, which was evaluated by a nuclear density gauge testing. Ballast was compacted to  $\gamma_d = 15.8 \text{ kN/m}^3$  by controlling the volume and weight of the material. FSTME represents the loaded area in one half of the transverse rail-tie-ballast system, separated by the longitudinal mid-plane. The load bearing area of a tie on ballast layer under one rail is approximately 0.15 m x 0.53 m (Ahlf 2007). Therefore, a segment of tie with dimensions of 0.53 (L) x 0.15 (H) x 0.18 (W) m was used. A typical axle load of 264 kN (wheel load = 132 kN) is reduced by the superstructure (i.e., rails and fasteners) to 66 kN on the ties according to Talbot (1980); i.e., approximately 25% of the wheel load. The wheel load was applied to the tie segment through a servo-hydraulic system (MTS<sup>®</sup>, loading capacity of 100 kN). Vertical deflection of substructure layers was measured with extensometers connected to linear variable differential transducer, LVDT, (Omega, 10±0.005-mm, Model AX/5/S) during  $10^5$  load cycles.

### 3.5.2 Large-Scale, Cyclic Triaxial Equipment

A prototype LSCT apparatus was developed to test a specimen with 305-mm diameter,  $D$ , and 610-mm length as shown in Fig. 3.5. A height to diameter ratio of 2 is used to minimize the effect of friction at both ends of the sample (Bishop and Green 1965). In addition, a specimen diameter to maximum particle size ( $d_{\max} = 63 \text{ mm}$ ) ratio of approximately 4.85 was used, which is considered adequate for representative volume of ballast in the specimen of LSCT test (Skoglund 2002; Anderson and Fair 2008). Confining stress (35–200 kPa) was applied with air (or water when volume change of specimen was measured). Top and bottom plates were machined from 25.4-mm-thick aluminum with a snake-drainage pattern to facilitate drainage from the specimen. Plastic and elastic deformations of ballast specimens were determined during  $2 \times 10^5$  of loading repetitions. Few LSCT tests were performed up to 0.5 million cycles. Number of loading cycles ( $2 \times 10^5$ ) was selected based on preliminary results to observe and characterize general deformational behavior of railway ballast and minimize the duration of each LSCT test.

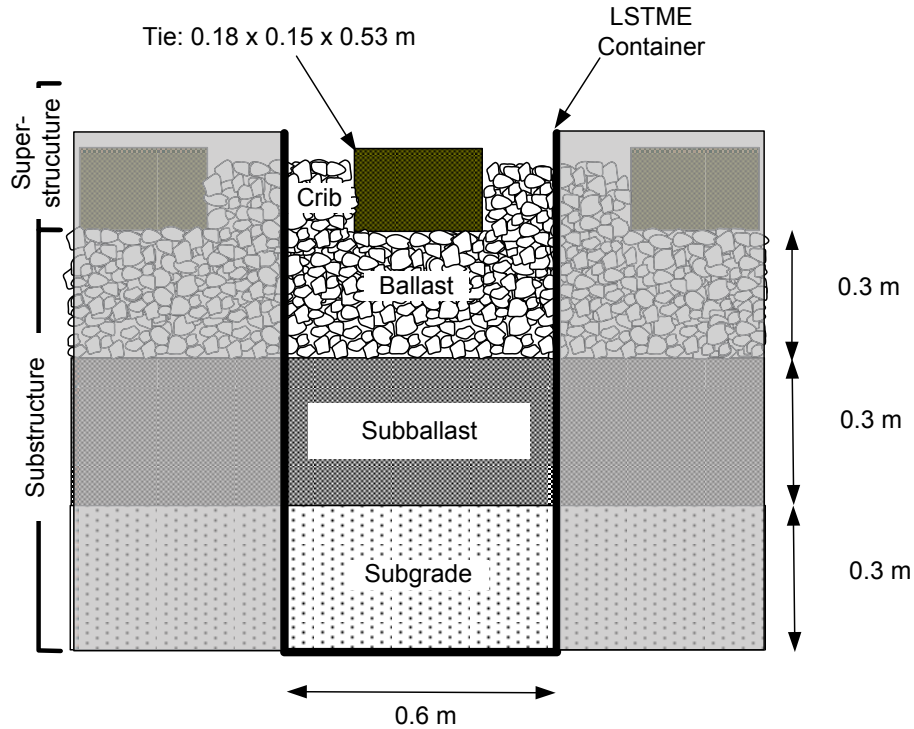


Figure 3.4 Schematic Configuration of Full-Size Prototype Track Model Experiment (FSTME)

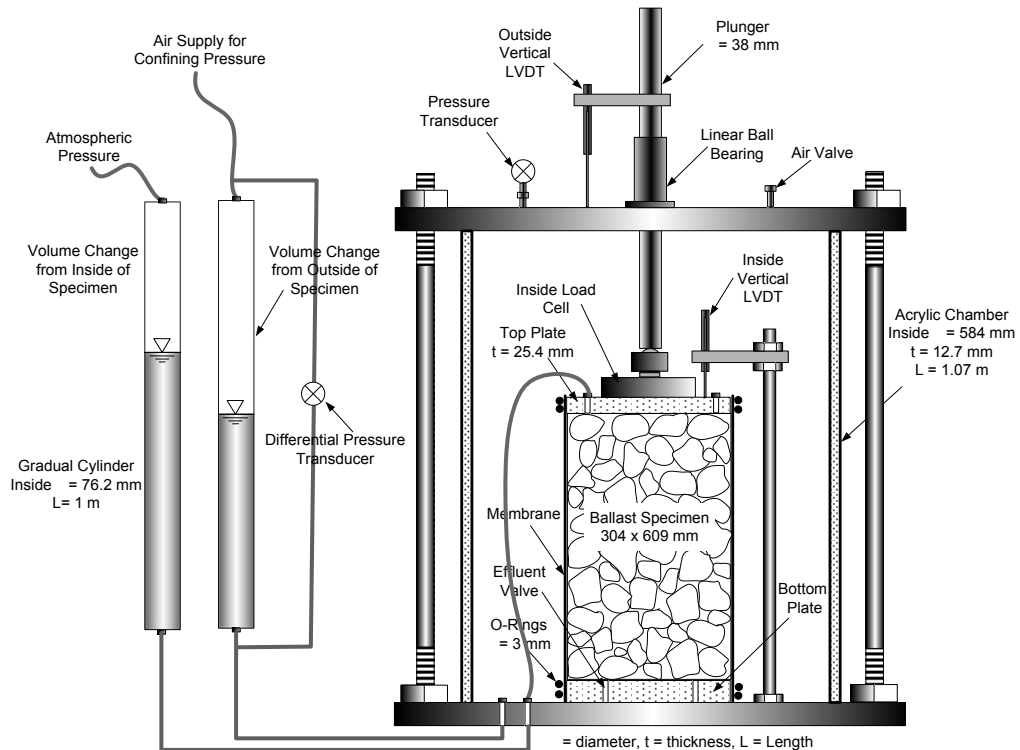


Figure 3.1 Schematic Configuration of Large-Scale Cyclic Triaxial (LSCT) Equipment for Measuring Plastic Deformation of Railway Ballast

### 3.5.2.1 Compaction Method

Proctor methods are usually employed to determine the compaction characteristics of geo-materials. However, standard (ASTM D698) and modified (ASTM D1557) Proctor methods are not appropriate for determining the compaction characteristics of ballast because the particle size of ballast (30 to 75 mm) is considerably larger than the typical particle size of Proctor testing (less than 30% retained on 19-mm sieve, per ASTM D698). In the Proctor test, the compaction energy and water content affect the compaction characteristics of materials; however, the effect of moisture and energy on compaction characteristics reduces as the uniform particle size increases from sand to gravel (Holtz and Kovacs 1981; Johnson and Sallberg 1960). Increasing compaction energy on soils, particularly gap-graded soils, can increase the amount of particle breakage (Ham et al. 2003). ASTM C29 describes two compaction methods for materials with large particle sizes: (1) a rodding procedure with 25 “vigorous” strokes of the tamping rod for  $d_{\max} < 37.5$  mm and (2) a jiggling method by dropping a cylindrical soil container with a volume of  $0.028\text{-m}^3$  on edges for  $37.5 \text{ mm} < d_{\max} < 125$  mm. In railway construction, ballast is compacted by inserting tamping tines into the ballast and vibrating at 20 Hz frequency (Selig and Waters 1994). Cribs and shoulders are compacted by pushing a flat plate on the surface (called ‘stabilizers’). Therefore, ASTM D29 does not represent the field compaction method for ballast. To reproduce similar compaction characteristics of ballast as achieved in the field, researchers have used different methodologies. Proposed compaction methods for ballast reported in the literature, along with typical ballast density and void ratio are summarized in Table 3.2. Lim (2004) used a 20-Hz vibratory hammer to simulate the tamping process in the field. Huang et al. (2009) used a vibratory compactor to compact ballast until the ballast particles did not exhibit any more settlement. Sevi et al. (2009) found the shaking table to be an effective method of compacting ballast. Indraratna et al. (2005) adopted standard Proctor testing by using 25 blows of a Proctor hammer on 50-mm-thick ballast lifts, impacted on a 5-mm-thick rubber to prevent particle breakage.

Vibratory and tamping contribute in different ways to ballast compaction via rearrangement and void filling. In this study, a 3-mm-thick, split-steel mold with 310-mm diameter and 710-mm height was used to determine the density of ballast with different methods to simulate field conditions, as follows:

1. *Shaking table with 15-Hz frequency.* Ballast was placed in four 150-mm lifts and shaken until no more particle movement was observed (about 5 min). A 100-N steel plate was set over the ballast to provide confinement. A 150-mm lift was selected to provide a uniform ballast specimen with  $d_{\max}$  of 63 mm. A dry unit weight ( $\gamma_d$ ) of  $14.3 \pm 0.3 \text{ kN/m}^3$  was achieved with this method.
2. *Vibratory rod.* This method simulated railway ballast tamping. Ballast was placed in the mold in 150-mm-thick lifts and compacted by a vibratory hammer (Fig. 3.6) at 20 Hz until no particle movement was observed (about 2 min). The vibratory rod resulted in a  $\gamma_d$  of  $14.5 \pm 0.5 \text{ kN/m}^3$ .
3. *Rodding.* This method simulated railway ballast stabilizers. Ballast was placed in four 150-mm lifts and rodded vigorously with a 45-N rod in each lift until no more visual particle movement occurred. A  $\gamma_d$  of  $14.6 \pm 1.0 \text{ kN/m}^3$  was achieved. Rodding of ballast mostly confined the particle to fill the voids, while limited particle rearrangement was observed.
4. *Vibratory rod and impact compaction:* Ballast was placed in four 100-mm lifts and rearranged with a 20-Hz vibratory rod until no more rearrangement is observed (~2 min). Then impact compaction was performed by dropping a 45-N, 100-mm plate from 100-mm height 40 times for each lift (Fig. 3.6). The corresponding weight and drop height limits the particle breakage during compaction.

The variation in density of ballast ( $\gamma_d$  between 14.3 and 15.8  $\text{kN/m}^3$ ) achieved through different compaction methods indicates varying effectiveness in achieving particle rearrangement and consistent densification. Method 4 (i.e., vibratory rod and impact compaction) provided reproducible compaction data and effective rearrangement and confinement of particles. This compaction method was thus used for determining ballast density and specimen preparation in the LSCT equipment.



Figure 3.6 Proposed Compaction Process: Rearranging Particles with Vibratory Rod (Left) and 45-N Dropping Plate for Densification (Right)

Table 3.2 Compaction Methods for Preparation of Ballast Specimens in Previous Studies

Source	Compaction Method	Density (kN/m <sup>3</sup> )	Void Ratio (e)	Max Particle Size, d <sub>max</sub> (mm)
Suiker et al. (2005)	40 strokes of a rod, 8 lifts of 75 mm	16.1-17.6	NR	38
Indraratna et al. (1998)	Standard Proctor, 25 blows on 50 mm	15.3	0.74	53
Indraratna et al. (2002)	Vibratory Hammer In 75-mm Lift	15.3	0.74	53
Lim (2004)	Vibratory Hammer	14.7-15.9	0.6-0.70	50
Auksidij (2007)	Vibratory Hammer	15.9	0.70	50
Anderson and Fair (2008)	Shaking Table, Particle dropping from 0.75 mm	14.7-15.0	0.81	50
	Shaking Table	16.4	0.68	20
Chavez et al. (2009)	Marshal Hammer, 6 lifts of 80 mm	NR	NR	40
Sevi et al. (2009)	Shaking Table, 5 lifts of 80 mm	15.4	0.7	63.5

### 3.5.2.2 Membrane Preparation

Membranes used in triaxial testing are typically manufactured by spraying a latex membrane around a mold. Due to difficulties of manufacturing large-size, continuous latex membranes and a limited market, few latex manufacturers provide a membrane with 305-mm diameter. Several studies described the problems with membrane thickness for preventing pin holes during compaction of sharp-edge ballast particles or rupture in high confining stresses (Suiker and Selig 2005; Anderson and Fair 2008; Chavez et al. 2009). As listed in Table 3.3, investigators have used latex or rubber membrane up to 5-mm thickness to address these problems. Increasing thickness of membranes increases unnecessary confinement of ballast specimens in the LSCT equipment that might affect the deformational behavior of ballast.

In this study, a minimum of four membranes was required to prevent ruptures under confining stress <200 kPa and pin holes during compaction. Two types of membrane, protective and air-tight, were used. Protective membranes were constructed manually with a medium-soft, natural-latex sheet and 0.76-mm thickness and tensile strength of 26.5 MPa. The membrane was cut to provide a diameter of 270 mm (10% less than specimen diameter per ASTM D3999). A quick set, super bonder (Loctite® adhesive, commercial standard A-A-3097) was used in seaming the membrane edges, which were cleaned thoroughly prior to bonding. The membrane seam was checked for leakage in accordance with ASTM D3999. Membranes constructed in this manner maintained confining stress ( $\sigma_3$ ) < 50 kPa, but leakage was observed during the triaxial test when  $\sigma_3 > 50$  kPa. An air-tight membrane was used as a seamless, manufactured membrane with 0.76-mm thickness (GeoTech) to provide adequate sealing in  $\sigma_3 > 50$  kPa. No puncture occurred in the four layers of membrane at  $\sigma_3 < 200$  kPa, whereas four layers of membrane were punctured at  $\sigma_3 = 250$  kPa at the location adjacent to the top or bottom platens.

Table 3.3 Membrane Thickness and Preparation for Testing Railway Ballast in Previous Triaxial Testing

Reference	Membrane Layer	Membrane Thickness (mm)	Preparation Method	Diameter (mm)
Suiker et al. (2005)	Two 0.76-mm Latex Membranes	0.76	Overlapped Seam	357
Lackenby et al. (2007)	One Layer Rubber Membrane	5.0	Manufactured	300
Anderson and Fair (2008)	Two 0.76-mm Latex Membrane	0.76	NR	357
Chavez et al. (2009)	One Layer Rubber Membrane	3-4 mm	NR	256
Sevi et al. (2009)	9.5-mm rubber sheet and Latex Membrane	0.63	Overlapped Seam	419

NR: not reported

### 3.5.2.3 Specimen Preparation for the LSCT test

A split-steel mold with inside diameter of 310 mm, height of 710 mm, and wall thickness of 3.1 mm was used for preparing the LCST specimens with 305-mm diameter and 610-mm height. A protective membrane was sealed around the base platen, and the specimen mold was secured around the base platen over the membrane. Another protective membrane was placed inside the first membrane and ballast was compacted to  $\gamma_{dmax} = 15.8 \text{ kN/m}^3$ , in accordance with the compaction method proposed in this paper. The 25.4-mm-thick top platen capped the specimen, and vacuum air was applied to hold the specimen before removing the split mold. The third membrane covered the entire specimen after removing the mold. A 76-mm-thick air-tight membrane sealed the specimen, leading to total membrane thickness of 3.0 mm of four used membranes. Two 3-mm-wide O-rings with 190-mm inside diameter sealed the air-tight membrane to the top and bottom platens. An acrylic cell was placed around the specimen in a 6.35-mm-deep groove and sealed with a 5.3-mm-diameter, cord O-ring. The acrylic cell was secured on top by a 25.4-mm-thick plate. The acrylic cell was also sealed on top with a 5.3-mm-diameter, cord O-ring placed in a 6.35-mm-deep groove.

### 3.5.2.4 Corrections for Membrane Penetration and Strength

In triaxial testing, the flexible membrane carries part of the axial and lateral loads applied to the specimen. Application of a membrane correction based on the assumption of thin wall cylindrical shell membrane in the triaxial test (Kuerbis and Vaid 1990) can be applied, as long as visible buckling does not occur and the membrane is not susceptible to buckling (< 5 to 10% of the compression strain in the specimen); therefore, axial pre-stretching of 5 to 10% is applied to the membrane during preparation. In the LSCT testing, no visible buckling was observed during the test; accordingly, the axial and radial stress correction for the membrane force (Kurbis and Vaid 1990) is:

$$\sigma_{am} = \sigma_a - \frac{4E_M t_o (2 + \varepsilon_v + \varepsilon_{Ma})(3\varepsilon_{Ma} + \varepsilon_v)}{3D_o (2 - \varepsilon_v + \varepsilon_{Ma})} \quad (\text{Eq. 3.1})$$

$$\sigma_{rm} = \sigma_r - \frac{4E_M t_o (2 + \varepsilon_v + \varepsilon_{Ma})\varepsilon_v}{3D_o (2 - \varepsilon_v + \varepsilon_{Ma})} \quad (\text{Eq. 3.2})$$

where  $\sigma_{rm}$  and  $\sigma_{am}$  are the radial and axial effective stresses on a soil specimen corrected for membrane stresses,  $\sigma_r$  and  $\sigma_a$  are the applied effective radial and axial stress, respectively, on a cylindrical soil specimen,  $\varepsilon_v$  is the volumetric strain of the cylindrical membrane referenced to un-stretched dimensions,  $\varepsilon_{Ma}$  is the axial strain in the cylindrical membrane shell, and  $E_M$  is the membrane modulus (8 MPa). The correction for the  $\sigma_d$  of 0 to 900 kPa varies between 0 and 3.5 kPa at  $\sigma_3$  of 210 kPa. The membrane correction for confining pressure ( $\sigma_c$ ) of 210 kPa is < 1 kPa. Even though four layers of membrane were used to prevent puncture and provide sealing, the effect of the membrane on axial and lateral stresses was negligible due to the large specimen size.

### 3.5.2.5 Data Acquisition

Confining stress was applied through a Fairchild™ pressure regulator (Model 10162, 15 to 1000 kPa). The confining stress was applied by an air pressure adjuster (QB1, Model TFEE100, Q1872), and controlled by a pressure transducer (Microswitch model 242DC100G 700 ± 1 kPa). A pressure gauge (0 - 1000 kPa, Swagelok model PGI-63B-MG1-LAQX) was connected to the top of the chamber to monitor the confining stress. A triaxial acrylic chamber (Abbott Plastics, 12.7-mm-thick wall, tensile strength = 43 MPa) was constructed to house a maximum confining pressure of 310 kPa (with a safety factor of 3). A brass ASME pop-safety valve (Model 9889K677) provided a mechanical safety for inside pressure. The confining pressure remained stable within a variation of ±2 kPa during testing. Axial load was applied by an MTS loading frame (280-liter/m MTS hydraulic actuator, 100-kN). An actuator load cell (MTS, 100 ± 0.1 kN) and inside load cell (DCT, DCL 100 ± 0.05 kN) were used to measure the applied load. A flange-mount linear ball bearing (Model 6483K78) with 38.1-mm inside diameter was employed to seal and reduce the friction resistance of the loading plunger (38.1-mm, super corrosion-resistance, stainless steel, precision round rod). Deflections outside and inside the cell were measured by LVDTs. An inside LVDT (Omega, 10±0.005-mm, Model AX/5/S) were used to eliminate the noise in recorded deformations. LVDTs were calibrated using a micrometer close to the intrinsic accuracy of LVDTs. Load cells were calibrated using a proving ring with accuracy of better than 1N.

### 3.5.2.6 Volume Change Measurements

Two graduated cylinders (76.2-mm diameter) were used to measure the volume change of ballast specimens during cyclic or monotonic triaxial tests, as shown in Fig. 3.5. One of the graduated cylinders measured the volume change of specimens from outside of the specimen, while the other graduated cylinder measured the volume change from inside of the specimen. The volume change from inside and outside of the clean ballast specimen was determined to control the leakage from the triaxial cell or the membrane. For fouled ballast specimens, volume change was only measured with the outside graduated cylinder. The specimen was not saturated in the case of fouled ballast to independently verify the effect of water content on the deformational behavior. Volume change was measured automatically using a differential pressure transducer.

### 3.5.2.7 Cyclic Loading Used in the Triaxial Testing

A finite element code, ANSYS, was used to predict the typical stress levels in railway ballast layers. 3D models were employed to simulate the overall state of stress in the railway ballast. The 3D model simulated the geometry conditions typical of a railway track system (see Fig 2.1). Ballast and subballast was modeled at 400- and 300-mm thickness with modulus of 400 and 200 MPa, respectively (Alva Hurtado and Selig 1981). The tie dimension was 150 by 180 mm, with tie spacing of 0.6 m and tie length of 2.5 m (Selig and Waters 1994). 25% of the wheel load (= 132 kN) was applied on the tie surface to account for the load distribution due to the rails and fasteners (Talbot 1980). The model consisted of one half of the track structure because of geometrical symmetry. The stress distribution from the wheel load in various depths of ballast showed that vertical ( $\sigma_1$ ) and lateral ( $\sigma_3$ ) stresses are the highest immediately under the location of loading (i.e., rails). The stress decreases in depth with asymmetry about the loading axis. The principal stress ratio ( $\sigma_1 / \sigma_3 < 4$ ) occurs when the lateral stress is between 50 and 200 kPa. A  $\sigma_1 / \sigma_3$  ratio between 4 and 12 occurs with lateral stress < 50 kPa, typically at the bottom of ballast layer.

The modeled vertical stress and corresponding horizontal stress from the track simulation is shown in Fig. 3.7. The vertical and horizontal stresses defined the range of principal stresses within the ballast. The horizontal stress (i.e., confining stress) varied between 10 and 200 kPa and vertical stress varied between 50 and 300 kPa.

### 3.5.2.8 Pulse Time and Frequency

Loading frequency is dependent on train speed and shape of stress curve at different depths of ballast. Ballast in a higher speed track undergoes a corresponding higher loading frequency. Ballast positioned at shallower depths undergoes shorter pulse time during cyclic loading. The stress distribution curve is wider for deeper ballast layers as compared to the surface ballast. A haversine function (Eq. 3.3) has been shown to imitate the shape of cyclic loading in geo-materials (Barksdale 1971; Loulizi et al.

2002) in transportation infrastructure. Vertical stress varies temporally as a haversine function, where  $x=0$  at the peak,

$$\sigma_v(x) = \sigma_{v0} \sin^2\left(\frac{\pi}{2} + \frac{\pi X}{L}\right) \quad (\text{Eq. 3.3})$$

where  $\sigma_{v0}$  is the maximum vertical stress and  $x$  is the distance from the center of loading. This equation was fit to the stress distribution curves at various depths of ballast to estimate the pulse length,  $L$ . Fig. 3.8 shows the fitted haversine function to the stress distribution curve resulting from the FE computer simulations to determine the pulse length ( $L_{HS}$ ). The pulse length varies between 1 and 3 m at various depths of ballast. Pulse time (pulse length / track speed) was calculated as a function of ballast depth under the tie for a train moving at 110 km/h (Fig. 3.9). Pulse time varies between 0.02 and 0.1 s with frequency of 20 to 10; i.e.,  $f=(\text{axle distance}/ \text{speed})^{-1}$ , which is in the range of reported frequency by other investigators (see Table 3.1). Although a loading frequency of 10 to 20 Hz with pulse time of 0.02 to 0.1 s is calculated for a track speed of 110 km/h, cyclic triaxial testing was performed at a loading frequency of 5 Hz based on the field data reported by (Indraratna et al. 2010).

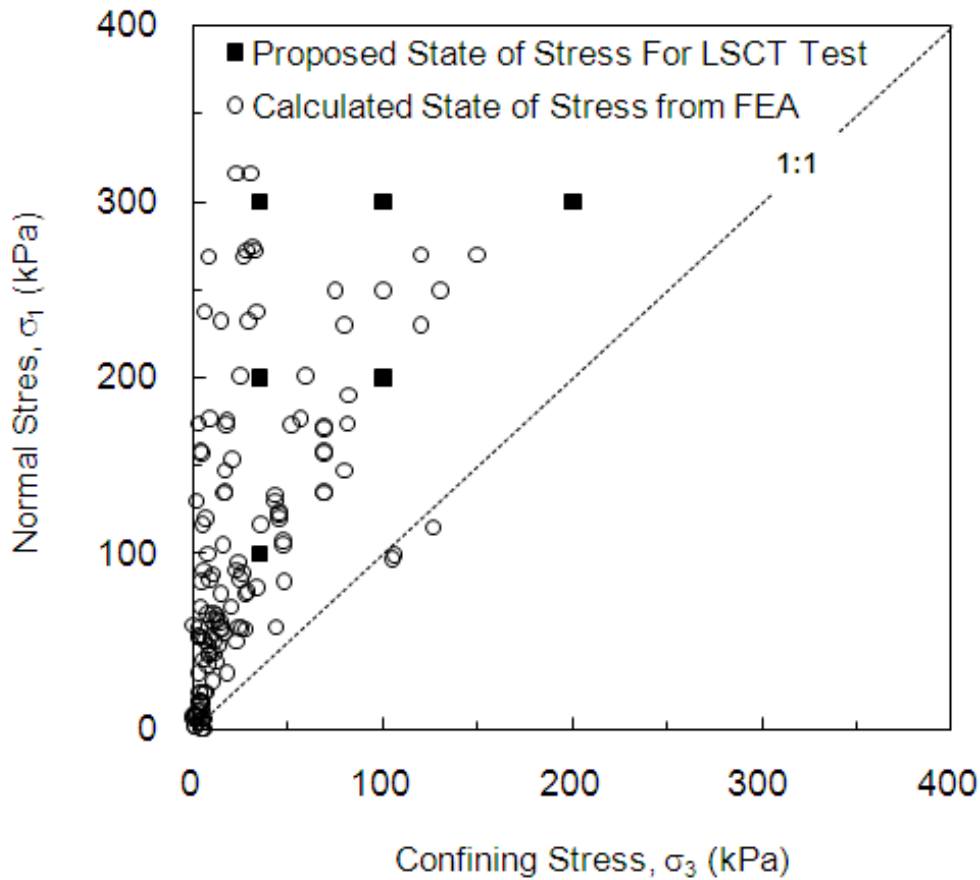


Figure 3.7 Calculated State of Stress in Railway Ballast from Finite Element Analysis and Proposed Stress Combinations (Solid Symbols) for Testing Ballast in the LSCT Test

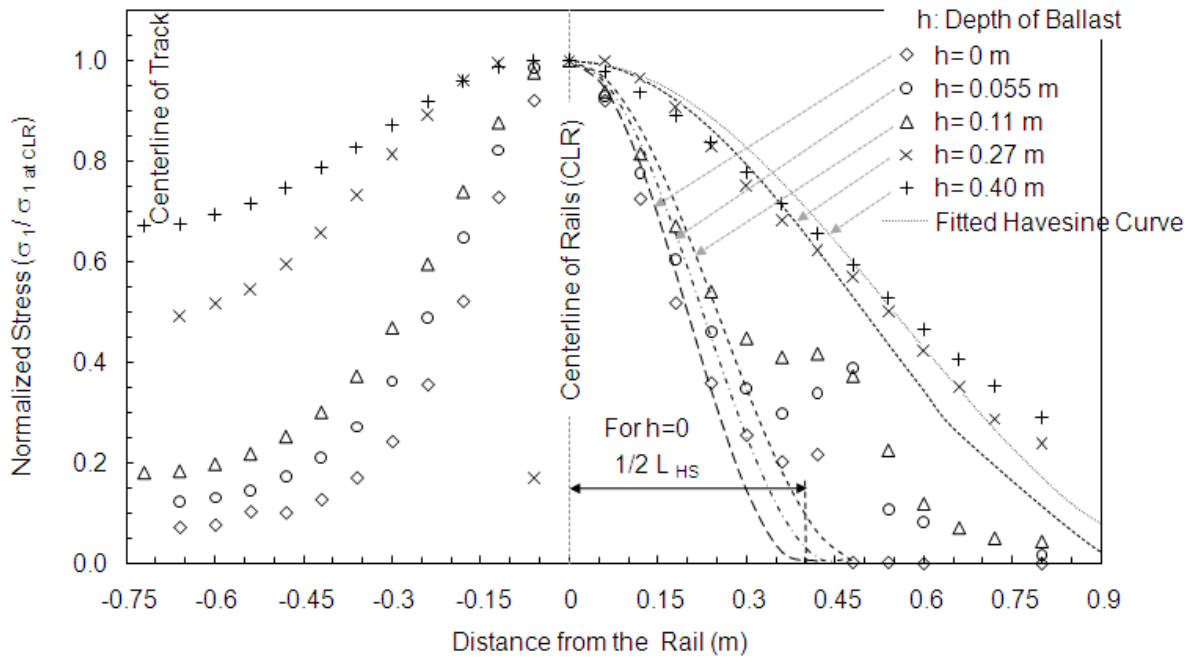


Figure 3.8 Havesine (HS) Function Fitted to the Stress Distribution Curves in Different Depth of Ballast to Determine the Pulse Length (Time) Used in the LSCT Test

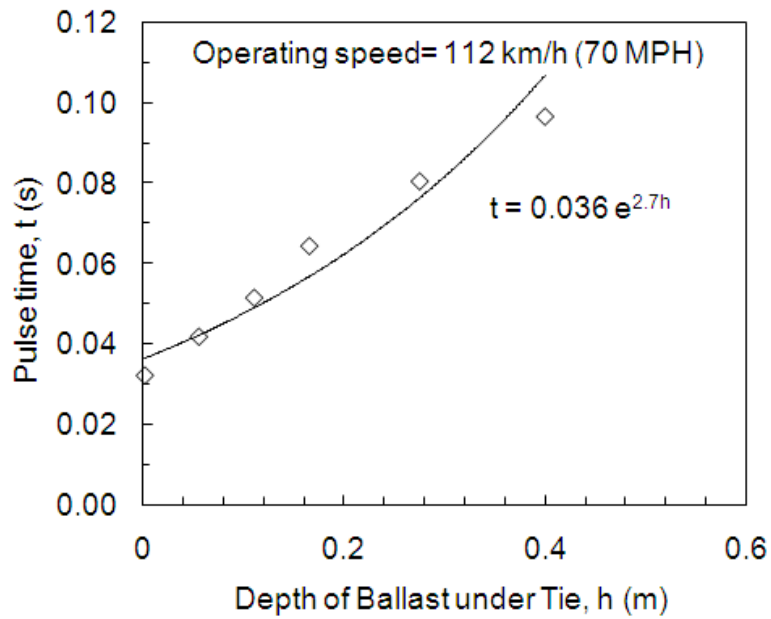


Figure 3.9 Pulse Time for Ballast Loading as a Function of Ballast Depth under Ties

### 3.5.2.9 Equipment Compliance

The system compliance between where the specimen was located and the deformation was measured, including all parts (top platens, bottom platen, and connections), was assessed. In accordance with ASTM D3999, a dummy cylindrical specimen of a similar size and length and Young's modulus of minimum 10 times the modulus of the tested materials was rigidly placed in the equipment. The deformation is recorded at different compression loads up to two times the expected load in the testing equipment. The minimum deformation monitored and recorded during the actual test was ten times the corresponding system deformation. In accordance with ASTM D3999, pebbles and crumbling result in excessive irregularity at the ends of specimens when large granular aggregate is used in a triaxial test. Compliance was reduced in the triaxial equipment by tapping and rotating the specimen cap on top of the specimen and filling the voids between the cap and specimen with smaller particles to provide more loading contacts between the specimen and the cap plate.

## 3.6 REPRESENTATIVE STATE OF STRESS FOR LSCT

A representative state of stress is necessary to systematically study the effect of various fouling conditions on ballast performance. To quantify this representative state of stress (i.e., confining stress,  $\sigma_3$ , and cyclic deviator stress,  $\sigma_d$ ) for testing fouled railway ballast in the LSCT, three steps were taken: (1) conducting a numerical analysis of rail track under typical wheel loads (i.e., 132 kN) to determine the distribution of  $\sigma_3$  and  $\sigma_d$  in the track substructure, (2) performing a series of LSCT tests using  $\sigma_3$  from 35 to 200 kPa and  $\sigma_d$  between 200 and 400 kPa as determined in the FEA, and (3) performing a prototype full-size track model experiment (FSTME) to determine the representative combination of  $\sigma_3$  and  $\sigma_d$  on the basis of matching the plastic strain of LSCT to the normalized deformation of the ballast layer from the FSTME. The comparison between the FSTM experiments and LSCT test results for ballast is shown in Fig. 3.10. The representative stress was found to be  $\sigma_3 = 90$  kPa and  $\sigma_d = 300$  kPa in which the normalized plastic deformation of ballast from the FSTME and plastic strain of ballast from the LSCT test are similar.

## 3.7 IMPLEMENTATION OF DEVELOPED METHOD

### 3.7.1 Sensitivity to Specimen Preparation of Fouled Ballast

When preparing a mixture of fine and coarse aggregates, the method of introducing fines is critical (Mitchell and Soga 2005). By extension, the method of preparing fouled ballast specimens is of critical importance. One method of preparing a fouled ballast specimen is to mix clean ballast with wet fouling material prior to compaction. In this study, we observed that ballast mixed with non-cohesive fouling materials (mineral and coal fouling) with water content greater than 8% create non-heterogeneous specimens. For example, mineral fouling with  $w=15\%$  created a non-uniform ballast specimen with density of  $14.0 \text{ kN/m}^3$  ( $e_B = 0.74$ ), while the target density was  $15.8 \text{ kN/m}^3$ . Moist fouling material was 'clumped' and created a 'layered soil mixture' as also described by Thevanayangam and Martin (2002). This condition is shown in Fig. 3.11d. A uniform mixture of ballast at highly, moderately, and clean fouling condition is shown in Fig. 3.11a-c. Fouling coats ballast particles and results in contamination of contact surfaces of ballast, as presented in Fig. 3.11e and 3.11f.

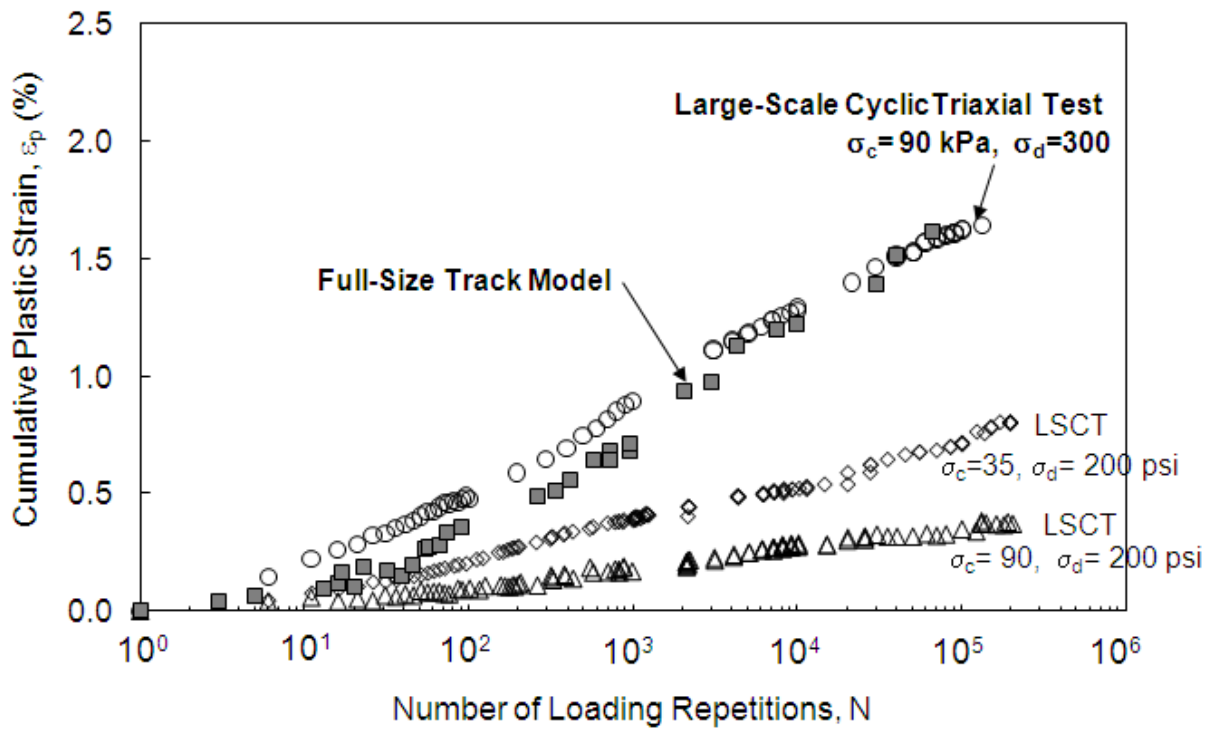


Figure 3.10 Matching the Plastic Strain of Ballast Obtained from Full-Size Track Model Experiment (FSTME) with the One Obtained from Different State of Stresses in Large-Scale Cyclic Triaxial (LSCT) Test

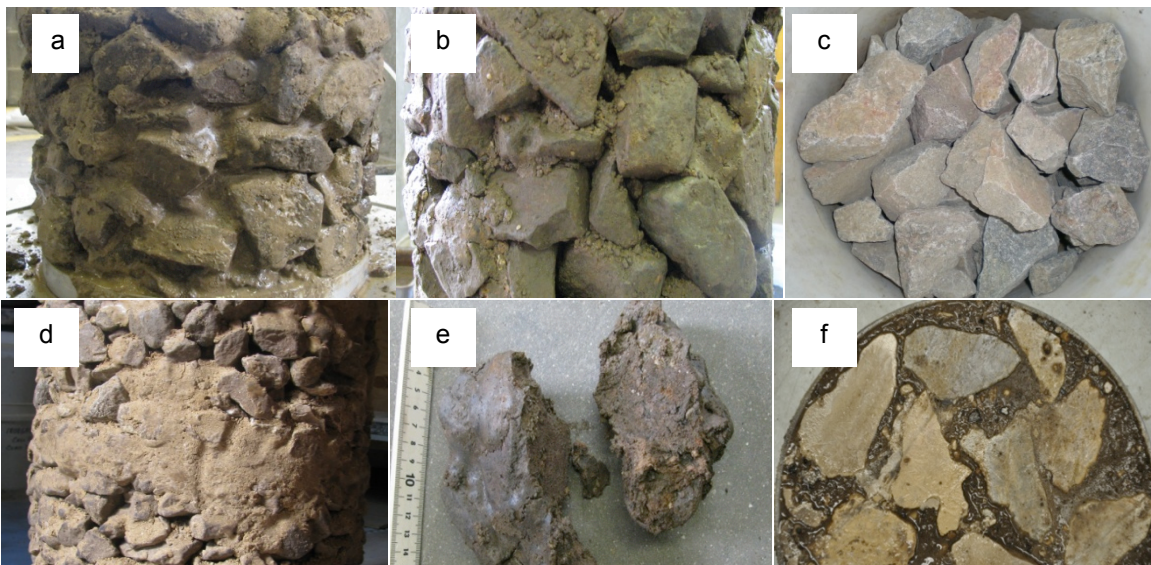


Figure 3.11 Highly Fouled Ballast (a), Moderately (5%) Fouled Ballast (b), Clean Ballast (c), Layered Fouling Mixture (d), Ballast Aggregate Coated by Fouling (e), and Cross Section of Fouled Ballast (f) from the Specimens of Large-Scale Cyclic Triaxial Test

One method of preparing a fouled ballast specimen is to mix ballast with moist, fouled material prior to compaction. This mixing method simulates the internal degradation of ballast particles under cyclic loading and infiltration of subgrade into the ballast in which the initial structure of ballast is deformed and the ballast particles are coated by fouling materials. However, a true methodology to simulate fouling via specimen preparation has not been identified due to the continual change of ballast properties. Huang et al. (2009) simulated ballast fouling from the surface (e.g., spillage of coal dust) by adding coal dust to the pre-compacted ballast assemblage. Therefore, a potential preparation method is to add wet fouling material to the pre-compacted ballast structure to simulate fouling due to surface spillage or wind-blown fines. Fig. 3.12 shows the results of cyclic testing on ballast prepared with 20% by weight fouling material and different specimen preparation methods.

The specimens prepared by adding the fouling material to the compacted ballast lifts (i.e., adding fouling to the ballast matrix that has been formed) resulted in plastic deformations ~ 25% less than those of the specimens prepared by mixing the fouling material prior to compaction. More likely, fouling material added to the pre-compacted ballast fills the voids of the ballast initially and, by progressive movement of particles, fouling affects the contact points between ballast particles and increases the plastic deformation.

Other factors that should be considered in the method of specimen preparation are the field activities, including maintenance. The adopted procedure mimics a tamping and compaction operation in railway ballast. Coal fouling (i.e., external spillage) might not contaminate the contact points of ballast aggregates solely by infiltration from the surface; however, rearrangement of aggregates (due to cyclic loading and tamping operations) likely results in contaminating the ballast aggregates contacts in the presence of coal. Typically, tamping activities rearrange the ballast particles to align the track surface; therefore, tamping disturbs the contact points of ballast. In a modified compaction procedure, ballast specimens with mineral and coal fouling were prepared by mixing clean ballast with fouling at  $w = 5-8\%$ . Clay fouled ballast (mimicking subgrade infiltration) was initially moistened to 15% prior to the mixing process. After the specimen was compacted, water content was increased by adding moisture from the top of the specimen. Six water content samples were taken from the specimen to ensure the uniformity of moisture in the specimen. Using this preparation method, the moisture content of the fouling materials varied  $\pm 1\%$ .

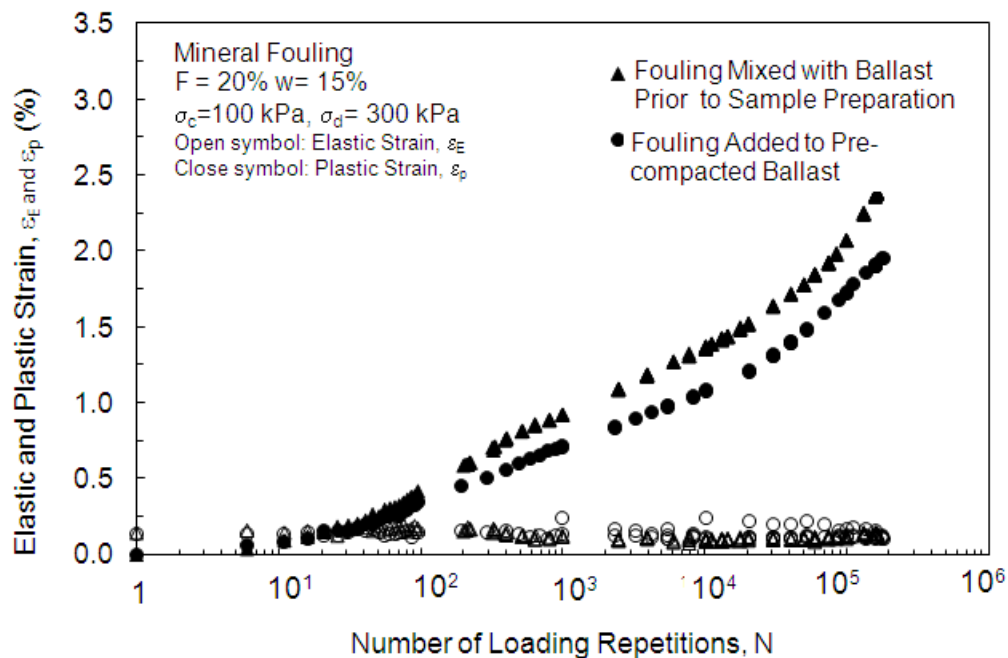


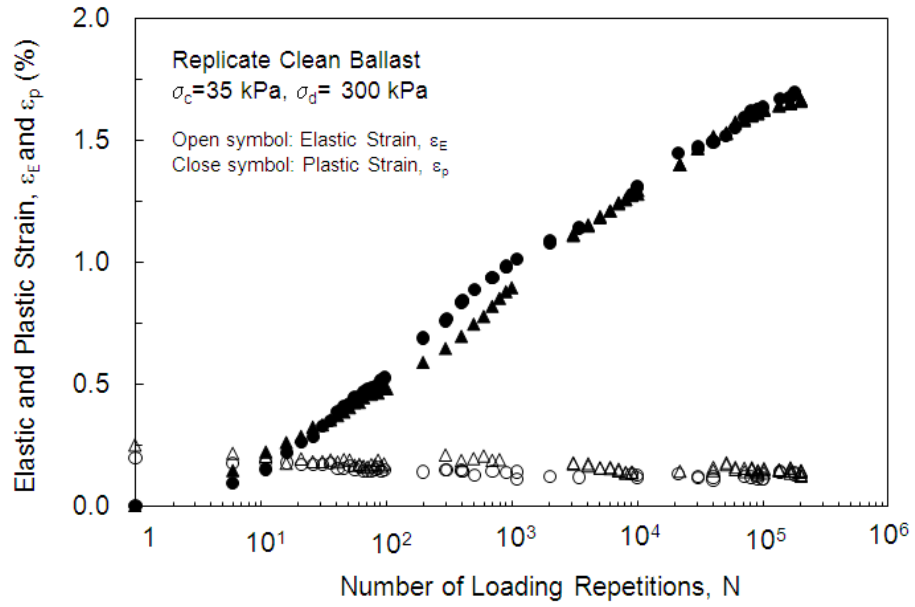
Figure 3.12 Effect of Specimen Preparation on Accumulation of Plastic Strain of Fouled Ballast in 20% by Weight of Fouling (F) and 15% Moisture (w) Obtained from LSCT Test

### **3.7.2 Repeatability of testing**

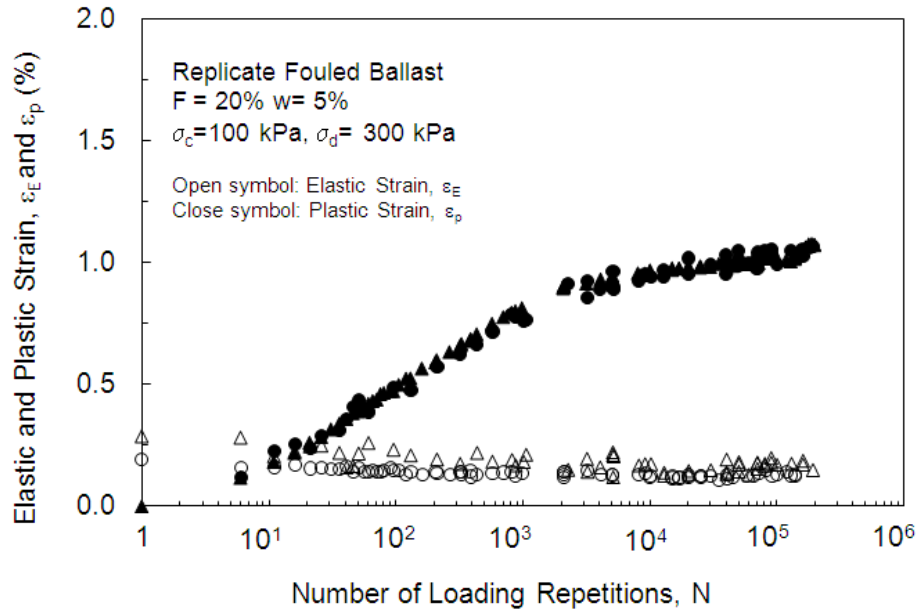
To evaluate the repeatability of LSCT testing, including sample preparation and deformational characteristics of ballast, cyclic testing on the specimens in the same fouling and loading conditions was replicated. The replicate test results of clean and fouled ballast are shown in Fig. 3.13. The deformation characteristics of ballast, such as elastic and permanent deformation, are consistent in both tests. During LSCT testing, appreciable rotation of the top plate was observed to influence the test results by providing a non-uniform state of stress and deformation on top of the ballast specimen. During LSCT testing, attempts were made to prevent misalignment of the loading piston. Specimens showed consistent and reproducible results when sufficient contact between ballast particles and top plate is attained. After compaction of the specimen, smaller ballast fragments ( $10 < d < 20$  mm) were located between large ballast particles to provide a better load-transferring interface between the specimen and the top platen.

### **3.7.3 Membrane Penetration and Volume Measurements**

Specimen consolidation was determined by measuring the volume change of a ballast specimen with time at constant confining pressure, as shown in Fig. 3.14. The rate of volume change decreased with time, which is negligible after 4 h. The volumetric strain was small (less than 0.15%), which likely resulted from the deformation and penetration of the latex membrane in the large void spaces of ballast. Similar volume change by measuring the volume of inside and outside of specimens exhibited no leakage of the specimens.



(a)



(b)

Figure 3.13 Repeatability of Collected Plastic Strain of Ballast in Clean (a) and Fouled (b) Condition from LSCT Equipment

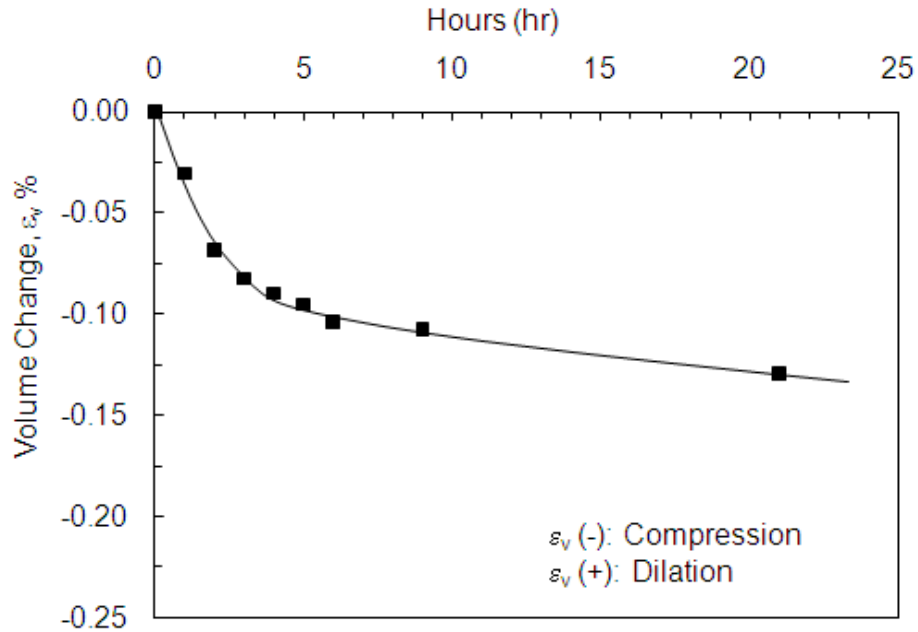


Figure 3.14 Volume Change of a Clean Ballast Specimen with Time in LSCT Equipment after Confining Stress is Applied

### 3.7.4 Effect of Fouling and Water Content on Deformational Behavior of Ballast

The developed testing protocol including testing equipment, specimen preparation, and state of stress was used to determine the deformational behavior of fouled railway ballast. Ballast was tested at different fouling conditions in the LSCT test. The plastic strain measured as a function of loading cycles is shown in Fig. 3.15. The data suggest that mineral fouling content up to 20% by itself does not affect the plastic deformation when the material is nearly dry. The rate of plastic deformation of the ballast at low water content ( $w = 0$  and 3 %), increases in the initial stage of loading cycles in semi-log-scale graphs and, subsequently, the rate of deformation becomes constant. Ballast with high fouling content ( $F = 10$  and 20%) and high water content (10 to 25%) exhibit significant increases in plastic deformation. The rate of plastic deformation at  $F = 10$  and 20% increases continually with increasing cycles of loading in semi-log scale.

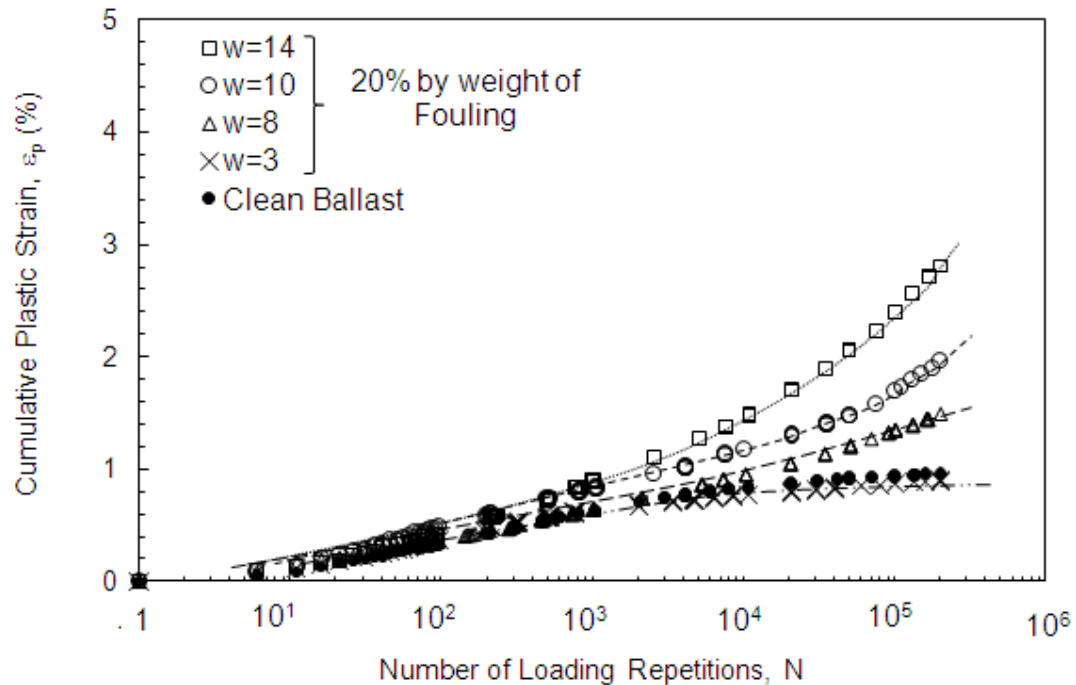


Figure 3.15 Effect of Fouling Content and Moisture on Plastic Strain of Ballast Obtained from LSCT Tests

### 3.8 CONCLUSION AND RECOMMENDATIONS

Large-scale, cyclic triaxial equipment and testing protocol were developed to measure plastic deformation of fouled railway ballast. A testing protocol and guidelines for fouled ballast was developed due to the lack of consistent and systematic testing guidelines in the literature and in rail engineering practice. Confining stress in the ballast layer varied between 20 and 200 kPa, and  $\sigma_d$  between 50 and 300 kPa. A 5-Hz haversine, bell-shaped loading pulse simulates the traffic loading on ballast. The representative state of stress for railway ballast of  $\sigma_3 = 90$  kPa and  $\sigma_d = 300$  kPa in the LSCT was determined. Ballast is recommended to be mixed with relatively dry fouling materials prior to compaction to prevent layered mixtures and simulate the tamping activities in the track. Moisture is then added from the top of specimens to study deformational behavior of ballast with water content.

### ACKNOWLEDGEMENT

Funding for this research was provided by National Center for Freight and Infrastructure Research and Education (CFIRE). Xiadong Wang (Soil Mechanics Laboratory) and William Lang (Structural and Material Laboratory) of the University of Wisconsin-Madison assisted with the experimental setups for the cyclic triaxial testing; their assistance is gratefully acknowledged. Assistance of BNSF and Wisconsin and Southern Railway companies for providing the testing materials is appreciated.

### REFERENCES

- Ahlf, R. E., 2007, Railway Track Systems: Engineering and Design, Unpublished and Personal Communication
- Alva-Hurtado, J.E., Selig, E.T., 1981, Permanent Strain Behavior of Railroad ballast," Proc. of int. Con. on soil mech. & geotech. Eng., Netherlands, Lisse, pp.543-546
- Anderson, W.F., Fair, P., 2008, Behavior of Railroad Ballast under Monotonic and Cyclic Loading, J. Geotech. and Geoenv. Eng., ASCE, 134(3), pp.316-328
- Anderson, W.F., and Key, A.J., 2000, Model Testing of a Two-Layer Railway Track Ballast, Chinese J. Catal., 126(4), pp.317-323.

- AREMA, 2003, Manual for Railway Engineering. American Railway Engineering Association, Washington, D.C
- ASTM C29/C29M, 2007, Standard Test Method for Bulk Density ("Unit Weight") and Voids in Aggregate, Annual Book of ASTM Standards, ASTM International, West Conshohocken, PA
- ASTM D698, 2007, Standard Test Methods for Laboratory Compaction Characteristics of Soil Using Standard Effort, Annual Book of ASTM Standards, ASTM International, West Conshohocken, PA
- ASTM D1557, 2009, Standard Test Methods for Laboratory Compaction Characteristics of Soil Using Modified Effort, Annual Book of ASTM Standards, ASTM International, West Conshohocken, PA
- ASTM D3999, 2003, Standard Test Methods for the Determination of the Modulus and Damping Properties of Soils Using the Cyclic Triaxial Apparatus, Annual Book of ASTM Standards, ASTM International, West Conshohocken, PA
- ASTM D5311, 2004, Standard Test Method for Load Controlled Cyclic Triaxial Strength of Soil, Annual Book of ASTM Standards, ASTM International, West Conshohocken, PA
- ASTM D6913, 2009, Standard Test Methods for Particle-Size Distribution (Gradation) of Soils Using Sieve Analysis, Annual Book of ASTM Standards, ASTM International, West Conshohocken, PA
- Aursudkij, B., 2007, A Laboratory Study of Railway Ballast Behavior Under Traffic Loading and Tamping Maintenance, PhD Thesis, The University of Nottingham, UK
- Barksdale, R.G., 1971, Compressive Stress Pulse Times in Flexible Pavements for Use in Dynamic Testing, Highway Research Record, Vol.345, pp.32-44
- Bishop, A.W., and Green, G.E., 1965, The Influence of End Restraint on the Compression Strength of a Cohesionless Soil, *Geotechnique*, 15, pp.243-266
- Chavez, E.R., Alonso, E.E., 2009, A Rockfill Triaxial Cell with Suction Control, *Geotechnical Testing J.*, GTJ101590, 32(3), pp.1-13
- Chrismer, S., and Davis, D., 2000, Cost Comparisons of Remedial Methods to Correct Track Substructure Instability, *Trans. Res. Rec.*, 1713, Paper 00-019, pp.10-15
- Haque A., Kamruzzaman, A., Christie, D., Bouazza, A.M., 2008, Towards a Better Design Guideline of Subballast Materials for Filtration Purpose Under Cyclic Load, *Proc. of Conf. Railway Eng.*, Perth, Australia, pp.611-617
- Holtz, R.D., and Kovacs, W.D., 1981, An Introduction to Geotechnical Engineering, Pearson Education Taiwan Ltd., Prentice Hall, Taiwan
- Huang, H., Tutumluer, E., Dombrow, W., 2009, Laboratory Characterization of Fouled Railroad Ballast Behavior, 88<sup>th</sup> annual Mtg. of Trans. Res. Board, on CD-ROM
- Indraratna, B., Lonescu, D., Chistie, H.D., 1998, Shear Behavior of Railway Ballast Based on Large Scale Triaxial Tests, *J. Geotech. and Geoenv. Eng.*, ASCE, 124(5), pp.439-449
- Indraratna, B., Lackenby, J., and Christie, D., 2005, Effect of Confining Pressure on the Degradation of Ballast under Cyclic Loading, *Geotechnique*, 55(4), pp.325-328
- Indraratna, B., Nimbalkar, S., Christie, D., Rujikiatkamjorn, C., Vinod, J., 2010, Field Assessment of the Performance of a Ballasted Rail Track with and without Geosynthetics, *J. of Geotech. & Geoenv. Eng.*, 136(7), pp.907-1008
- Johnson, A.W., and Sallberg, J.R., 1960, Factors that Influence Field Compaction of Soils, Bulletin 272, Highway Research Board, pp.206-210
- Kuerbis, R.H., Vaid, Y.P., 1990, Corrections for Membrane Strength in the Triaxial Test, *Geotechnical Testing J.*, GTJODJ, 13(4), pp.361-369
- Lackenby, J., Indraratna, B., McDowell, G., Christie, D., 2007, Effect of Confining Pressure on the Ballast Degradation and Deformation under Cyclic Triaxial Loading, *Geotechnique*, 57(6), pp.527-536
- Lee, H. M., 2009, Ballast Evaluation and Hot Mixed Asphalt Performance, *Proc. BCR2A Conf.*, University of Illinois Urbana-Champaign, Urbana, IL, pp.1283-1289.
- Liu, J., and Xiao, J., 2010, Experimental Study on the Stability of Railroad Silt Subgrade with Increasing Train Speed, *J. of Geotech. & Geoenv. Eng.*, 136(6), pp.833-842
- Lim, W.L., 2004, Mechanics of Railway Ballast Behavior, PhD Thesis, Univ. of Nottingham, UK
- Louilizi, A., Al-Qadi, I.L., Lahouar, S., Freeman, T., 2002, Measurement of Vertical Compressive Stress Pulse in Flexible Pavements, *Trans. Res. Rec.*, 1816, 02-2376, pp.125-137
- Mitchell, L. K., Soga, K., 2005, Fundamentals of Soil Behavior, 3rd Edition, John Wiley and Sons Inc., NY
- Raymond, G.P., Bathurst, R.J., 1994, Repeated Load Response of Aggregates in Relation to Track Quality Index, *Canadian Geotechnical Journal*, 31, pp.547-554

- Sekine, E., Kono, A., Kito, A., 2005, Strength and Deformation Characteristics of Railroad Ballast in Ballast Particle Abrasion Process, QR of RTRI, 46(4), pp.256-262
- Selig, E.T., and Waters, J.M., 1994, Track Geotechnology and Substructure Management, Thomas Telford, NY
- Sevi, A.F., Ge, L., Take, W.A., 2009, A Large-Scale Triaxial Apparatus for Prototype Railroad Ballast Testing, Geotechnical Testing J., GTJ102033, 32(4), pp.1-8.
- Skoglund, K. A., 2002, A study of some factors in mechanistic railway track design, Ph.D. dissertation, Norwegian University of Science and Technology.
- Suiker, A.S.J., Selig, E.T., Frenkel, T., 2005, Static and Cyclic Triaxial Testing of Ballast and Subballast, J. Geotech. & Geoenv. Eng., ASCE, 131(6), pp.771-782
- Talbot, A.N., 1980, Stresses in Railroad Track - The Talbot Reports, American Railway Engineering Association
- Thevanayagam, S., and Martin, G.R., 2002, Liquefaction in Silty Soils - Screening and Remediation Issues, Soil Dynamics and Earthquake Eng., 22, pp.1035–1042
- Thompson, M.R., Hay, W.W., Tayabji, S.D., 1976, Reports of Ballast and Foundation Materials, US DOT, Washington, D.C.
- Zaayman, L., 2006, Ballast Cleaning, a Prerequisite for a Sustainable, Reliable, Safe and Cost Effective Railway Track, Magazine of the South African Institute of Civil Eng., 14(5), pp.20–29

## **CHAPTER 4: DEFORMATIONAL BEHAVIOR OF FOULED RAILWAY BALLAST**

### **4.1 ABSTRACT**

Plastic strain of railway ballast subjected to various fouling conditions (fouling material type, fouling content, water content) was determined with a large-scale cyclic triaxial apparatus under typical traffic loading. Effect of fouling material type, such as mineral fouling from ballast degradation, coal fouling from surface spillage, and clay fouling from subgrade infiltration, on plastic strain of railway ballast was studied. Mechanisms by which fouling materials affect the plastic strain of railway ballast were investigated. The results of this study show that fouling increases the plastic strain of ballast by affecting the condition of the contact points of large ballast particles. Fouling interacting with the contact points of ballast particles reduces the shear resistance properties of the ballast skeleton and accelerates the accumulation of plastic strain. Increasing moisture >3% and fouling content (% by weight of particles < 4.75 mm) resulted in larger accumulation of plastic strain in fouled ballast. Plastic strain increases linearly with fouling and water content. For mineral and coal fouling, plastic strain is affected by two main factors: fouling and moisture; whereas, with cohesive (clay) fouling, plastic strain is controlled not only by moisture and fouling, but also by compositional characteristics of the cohesive fouling material, primarily represented by Atterberg limits and % mass < 0.075 mm.

### **4.2 INTRODUCTION**

A major concern facing the freight rail industry in the US is increasing maintenance costs due to heavier freight load (Lee 2009). Maintenance operations for ballast in the U.S. cost about \$500 million annually for 150,000 km of Class1 track (\$3,800/km/yr, Christmer and Davis 2000). The main reason for track maintenance is accumulation of deformation in ballast and subgrade layers, which may result in surface deviation of the railway track. Clean railway ballast, consisting of angular, uniform, large-grain particles has a significant role in distributing the train loads to the underlying subgrade. Unlike granular layers in pavement structures, ballast significantly deteriorates over time under heavy freight loads and deviates from its original standard specifications by creating fines (typically particles < 4.75 mm). Generation of fines in ballast creates 'fouled ballast', which can cause significant accumulation of deformation in the track. The frequency of railway maintenance is linked to the quality of ballast, which changes continually due to the generation of fine particles (i.e., 'fouling').

Fouling is caused by a number of mechanisms. Fracturing and abrasion (i.e., particle attrition) of ballast or infiltration of subballast under cyclic loading results in 'mineral fouling.' Infiltration from underlying subgrade results in 'clay fouling.' Spillage from surface sources (e.g., 'coal fouling') is another mechanism of fouling. In the US, particle attrition is the greatest cause of fouling and generates 76% of fouling (Selig and Waters 1994), while surface spillage is the main source of fouling in the UK with 52% (Darell 2003). Fouling impacts the track performance by changing the mechanical properties of substructure layers through (1) loss of effective drainage, (2) formation of "mud-holes", (3) lack of resistance to lateral and longitudinal forces, (4) poor durability after maintenance, and (5) increasing rate of deterioration (Haque et al. 2008; Zaayma 2006; Liu and Xiao 2010). Railway professionals largely agree that fouling appreciably changes the deformational behavior of railway track (Selig and Waters 1994). However, there are limited available data or techniques to characterize the behavior of fouled railway ballast.

The objective of this paper is to quantify the deformational behavior (i.e., plastic strain) of ballast in various fouling conditions under freight traffic. The plastic strain of fouled ballast by mineral, coal, and clay fouling is determined using large-scale cyclic triaxial (LSCT) equipment. Mechanisms by which fouling affects the plastic strain of ballast are discussed.

### **4.3 MATERIALS**

#### **4.3.1 Fresh Ballast**

A sample of granitic fresh ballast was provided from a quarry in Wyoming by BNSF Railroad Company. The particle size distribution of the ballast (in accordance with ASTM D6913) in comparison to ballast specification #24 by AREMA 2003, is shown in Fig. 4.1. The particle size distribution of the as-received fresh BNSF ballast is slightly coarser than that of the AREMA 2003 specification. The fresh

ballast has a maximum particle size of 63 mm and a minimum particle size of 25 mm. The ballast particles had irregular shape, with a particle aspect ratio (ratio of the largest to the smallest dimension) of 2.5. The fresh ballast had relatively sharp edges. In a ‘clean’ condition and at the maximum unit weight of 15.8 kN/m<sup>3</sup>, the fresh ballast had a void ratio ( $e_B$ ) of 0.62.

#### 4.3.2 Recycled Ballast

A sample of highly fouled dolomitic ballast was obtained from a stockpile in a track yard of the Wisconsin and Southern Railroad Company (WOS) in Madison, WI. Particles larger than 19 mm were retained as ‘recycled ballast’, which is based on the current state of practice for ballast recycling (Ahlf 2007). Recycled ballast particles are smaller than the AREMA#24 specification. The recycled ballast had a maximum particle size of 53 mm and a particle aspect ratio of 2; i.e, fairly rounded due to attrition and erosion processes. In a clean condition and at the maximum unit weight of 18.4 kN/m<sup>3</sup>, recycled ballast had  $e_B = 0.53$ . The difference in void ratio of fresh and recycled clean ballast is likely due to the higher angularity of fresh ballast, similar to the effect of angularity on density of sand (Edil et al. 1975).

#### 4.3.3 Fouling Materials

Different sources of fouling materials were tested in this study: (1) mineral fouling due to subballast intrusion or ballast breakage, (2) coal fouling due to surface spillage, and (3) clay fouling due to subgrade infiltration. Mineral fouling was obtained by fractioning highly fouled ballast obtained from WOS Railroad Company. The fraction passing a No.4 sieve (4.75 mm), based on the criteria by Selig and Waters (1994), is designated mineral fouling.

Coal fouling was obtained by grinding Wyoming-based coal to produce particles with a size distribution similar to typical coal fouling that has been observed in the field (Huang et al. 2009). Fig. 4.1 shows particle size distributions of mineral and coal fouling. The mineral and coal fouling both had low plasticity (i.e., plastic limit, PL, was not achieved) and are collectively referred as non-cohesive fouling material. Table 4.1 summarizes the physical properties of mineral and coal fouling.

Different cohesive fouling mixtures were produced in the laboratory using low and high plasticity clay sources (designated as ‘Clay L’ and ‘Clay H’) from Sauk County, WI. Table 4.2 presents the physical properties of the cohesive fouling materials. Modified Clay L and H were prepared to target a wide range of cohesive fouling that may occur in the field with respect to particle size distribution, plastic limit, liquid limit (LL), and fines content.

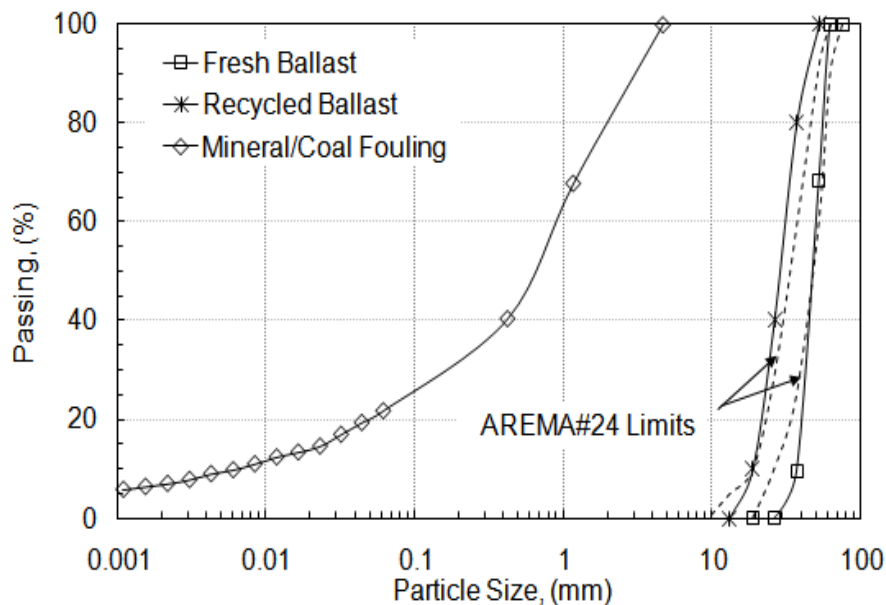


Figure 4.1 Particle Size Distribution of Fresh and Recycled ballast and Mineral and Coal Fouling

Table 4.1 Index Properties of Ballast and Non-Cohesive Fouling Materials

Sample	D <sub>50</sub> (mm)	C <sub>u</sub>	C <sub>c</sub>	G <sub>s</sub>	LL (%)	PL (%)	e <sub>B</sub>	Sand Content (%)	Fines Content (%)	USCS Symbol
Fresh BNSF Ballast	53	1.4	0.6	2.6	NA	NA	0.62	0	0	-
Recycled Ballast	30	1.7	0.8	2.65	NA	NA	0.53	0	0	-
Mineral Fouling	1	113	4.5	2.6	20	NP	-	100	20	SM
Coal Fouling	1	113	4.5	1.3	31	NP	-	100	20	SM

Note. NP = not plastic, NA = not applicable, D<sub>50</sub> = median particle size, C<sub>u</sub> = coefficient of uniformity, C<sub>c</sub> = coefficient of curvature, G<sub>s</sub> = specific gravity, LL = liquid limit, PL = plastic limit, e<sub>B</sub> = void ratio of ballast. Particle size analysis conducted following ASTM D 422, G<sub>s</sub> by ASTM D 854, USCS classification by ASTM D 2487, and Atterberg limits by ASTM D 4318.

Table 4.2 Index Properties of Cohesive Fouling Materials

Clay Fouling	LL (%)	PI (%)	C <sub>u</sub>	Clay Fraction	USCS Symbol	Nomenclature P200/LL/PI
Clay L Low plasticity	36	19	2.0	80	CL	90/36/19
Clay H High plasticity	64	42	3.5	51	CH	60/64/42
Modified Clay L	28	6	5.3	ND	CL-ML	90/28/6
Modified Clay H	38	22	10	34	SC	40/38/22
	30	14	25	25	SC	30/30/14
	21	NP	62	17	SC-SM	20/21/NP
	20	NP	253	8	SM-SW	10/20/NP
	20	NP	-	4	SM	5/20/NP

Note. ND= Not Determined, NP= non plastic, LL = liquid limit, PL = plastic limit, PI = plasticity index. USCS classification following by ASTM D 2487, and Atterberg limits by ASTM D 4318. C<sub>u</sub> & C<sub>c</sub> = coefficient of uniformity & coefficient of curvature of fouling.

## 4.4 FOULING RELATED DEFINITIONS

### 4.4.1 Fouling Index

Fouling has been identified as small-size particles in the matrix of large-size ballast particles (Selig and Waters 1994; Ionescu 2004; Zaayman 2006). Several correlations and indices have been proposed in the rail profession to define the effective grain size of fouling materials and their impact on the railway track. Selig and Waters (1994) defined a fouling content (FC) that has been widely used in the USA:

$$FC = P4 + P200 \quad (\text{Eq. 4.1})$$

where P4 fraction is % mass < 4.75 mm, and P200 fraction is % mass < 0.075 mm. A universal fouling index that accounts for the type of fouling and effect of moisture on deformational behavior of railway track has not been established in the literature.

### 4.4.2 Volumetric Fouling Index (FI)

Fouling content is typically expressed in terms of mass percentage. Because the deformational behavior of railway ballast is likely affected by contaminated contact points of ballast particles, fouling material of the same mass but with different specific gravity (e.g., mineral and coal fouling) would occupy different volumes in the ballast. The contaminated contact points of ballast are proportional to the relative volume of the voids that has been occupied by fouling. Therefore, a volumetric fouling index (FI) is proposed in this study to equate the volume of fouling in ballast when different fouling materials are involved:

$$FI = FC \frac{G_{so}}{G_s} \quad (\text{Eq. 4.2})$$

where FC is from Eq.4.1,  $G_{so}$  is the reference specific gravity (= 2.6, which is the  $G_s$  of mineral fouling), and  $G_s$  is the specific gravity of the specific fouling material.

#### 4.4.2.1 Contaminated Contact Points of Ballast Particles

The mechanisms by which fine particles affect the strength and deformational properties of coarse-particle ballast matrix has been evaluated in studies of the behavior of gap-graded material such as mixtures of sand and fines. Thevanayangam and Martin (2002) showed that shear strength properties of a sand-silt mixture decreases or is unaffected by increasing the silt fraction. Polito and Martin (2001) stated that when the voids created by large particles are filled by fines but the contact points of particles are intact, the strength and deformational properties of the mixture is not influenced by the presence of fines. If fines coat the contact points of large particles, an unstable structure may develop that may decrease the strength of the original particle network. For example, Polito and Martin (2001) stated that fines content (< 0.075 mm) between 25 to 45% can initiate the formation of an unstable condition for typical gap-graded sand-fines mixtures. Similar mechanisms are hypothesized when ballast is mixed with fouling. As illustrated in Fig. 4.2, when the proportion of fouling (i.e., fines) increases, ballast particles eventually become embedded in a matrix of fines and the macro void space formed by the ballast particles increases.

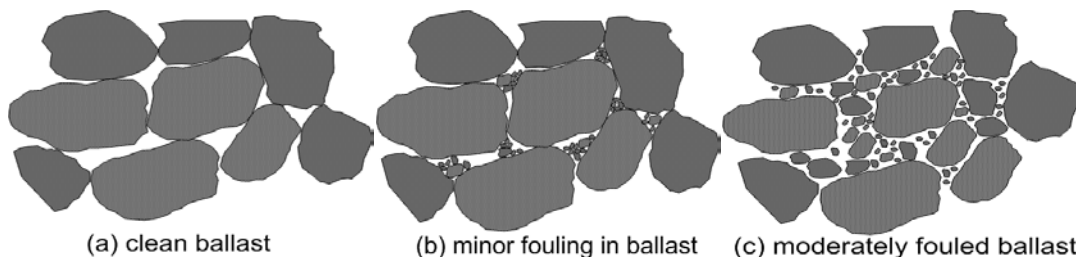


Figure 4.2 Various Conditions of Ballast Particles Mixed with Fines, (a) Clean Contacts, (b) Minor Fines and Unaffected Contacts, and (c) Contaminated Contacts with Meta-Stable Structure

To evaluate the presence of fouling at the contact points of ballast particles, the macro void space created by coarse ballast particles in clean and fouled ballast are compared. Fig. 4.2 shows that an increase of the void ratio of macro pores of ballast indicates contamination of ballast particle contacts; i.e., expansion of the ballast skeleton due to intrusion of fouling material at the contact points. The macro void ratio of ballast ( $e_B$ ) in different fouling conditions can be calculated from Eq. 4.3:

$$e_B = \left( \frac{G_{sB} \gamma_w V_t}{W_B} - 1 \right) \quad (\text{Eq. 4.3})$$

where  $\gamma_w$  is unit weight of water,  $V_t$  is the total volume of fouled ballast specimen,  $W_B$  is the weight of coarse ballast particles contained in the specimen, and  $G_{sB}$  is the specific gravity of ballast. As shown in Table 4.1, fresh ballast has  $e_B$  equal to 0.62 when compacted to the achievable maximum unit weight of  $15.8 \text{ kN/m}^3$ . In Eq. 4.3, the reduction in void ratio of ballast is ideally assumed to be solely due to the contamination of contact points of ballast.

#### 4.5 EXPERIMENTAL EQUIPMENT AND METHODS

A prototype large-scale cyclic triaxial (LSCT) apparatus was developed to test specimens with 305-mm diameter and 610-mm length (volume of  $0.044 \text{ m}^3$ ). The LSCT is capable of performing cyclic testing at varying cyclic stress, confining stress, loading frequencies, pulse shapes, and drainage conditions. The LSCT equipment and a prepared ballast specimen are illustrated in Fig. 4.3. LSCT tests were performed at 5 Hz, similar to what was measured in the field by Indraratna et al. (2010). Plastic (permanent) deformation of ballast was recorded over  $N = 2 \times 10^5$  traffic cycles of loading. The  $N = 2 \times 10^5$  was selected in our preliminary tests to capture the effect of fouling conditions on long-term accumulation of plastic strain of ballast under traffic load.



Figure 4.3 Large-Scale Cyclic Triaxial (LSCT) Apparatus for Ballast Testing (left) and a Prepared Railway Ballast Specimen before Testing (right)

#### 4.5.1 LSCT Test Method

A steel split mold with inside diameter of 310 mm, height of 610 mm was used for preparing the LSCT specimens. Three membranes with 0.76-mm thickness were used as protective membranes during ballast compaction. An air-tight membrane with 0.76-mm thickness was used to seal the protective membranes with potential pin holes due to the compaction method, as shown in Fig. 4.3. Total membrane thickness was 3.0 mm. A membrane effect correction was made as described by Kuerbis and Vaid (1990). The LSCT cell was assembled using the acrylic cell wall and top plate. Vacuum was released as the chosen confining stress was applied in the cell with open drainage. Subsequently, the cyclic stress was applied to the specimen using a loading rod attached to the top loading platen with open top and bottom drainage. Axial deformation of the specimen under cyclic loading was recorded by inside (mounted at the top of loading platen) and outside LVDTs from which plastic deformation was obtained. While plastic deformation was recorded both by the inside and outside LVDTs, the data from the outside LVDT was used to calculate the plastic strain of ballast. Elastic deformation measurements are typically affected by system compliance and are recorded by inside LVDTs. Plastic strain of railway ballast was computed by dividing the specimen deformation by the original height of the specimen. Axial load was applied by a MTS™ loading frame (280-L/m MTS hydraulic actuator, 100-kN). Details of the loading system and instrumentation are given in Chapter 3.

#### 4.5.2 Specimen Preparation for LSCT test

The ratio of the specimen diameter ( $D$ ) to maximum particle size ( $d_{max}$ ) was 5. Ballast was compacted to a maximum dry unit weight of  $15.8 \pm 0.3 \text{ kN/m}^3$ . Ballast was placed in lifts of 100-mm and compacted using a vibratory rod with a frequency of 20 Hz until no more rearrangement of particles was observable (about 2 min). Impact compaction was then applied by dropping a 100-mm-diameter plate weighing 45-N from a height of 100-mm 40 times over each lift.

#### 4.5.3 Determination of Stress Combinations for Triaxial Testing

To study the effect of various fouling conditions on ballast, a representative field state of stress was determined a typical ballast layer. The representative stresses were found to be confining stress ( $\sigma_3$ ) = 90 kPa and cyclic stress ( $\sigma_d$ ) = 300 kPa following a three-step procedure described in Chapter 3. Ballast specimens were tested at this representative state of stress to independently evaluate material factors such as fouling index and moisture content.

### 4.6 EXPERIMENTAL RESULTS

#### 4.6.1 Plastic Strain of Clean Fresh and Recycled Ballast

Under cyclic loading, only a portion of the deformation that occurs is recovered. Lambe and Whitman (1969) stated that the deformation from sliding between particles or from fracturing of particles is largely irreversible. However, there is small reversible deformation due to confinement by other particles. Size/shape and mineralogy of granular particles affects the accumulation of plastic strain under cyclic loading. Tests were performed to observe the difference in the plastic strain due to type of ballast; e.g., fresh versus recycled. The accumulation of plastic strain ( $\epsilon_p$ ) of clean fresh and recycled ballasts is shown in Fig. 4.4. Plastic strain is a function of the number of loading cycles ( $N$ ). The number of loading cycles can also be expressed in equivalent million gross tons (MGT), a widely used terminology among rail professionals. In our tests, freight with an axle load of 264 kN (~ 30 tones) was simulated. Therefore, million gross tones can be defined as:

$$\text{MGT} = \frac{N \times 30}{10^6} \quad (\text{Eq. 4.4})$$

The fresh ballast shows linear accumulation of  $\epsilon_p$  up to  $N = 10^4$  and relatively constant  $\epsilon_p$  thereafter in a semi-logarithmic scale. The behavior prior to  $N = 10^4$  is termed herein as 'initial compaction phase (ICP)' for ballast particles under cyclic loading and virtually all samples displayed this behavior. During the ICP, the number of contacts between ballast particles increases due to particle rearrangement and densification. Lambe and Whitman (1969) stated that this behavior in granular particles is likely due to a

gradual increase in the contact areas, or because the contamination (dust or small fragments) are gradually squeezed out from the contact surfaces.

Plastic strain of clean recycled ballast after  $N = 2 \times 10^5$  is 50% greater than that of clean fresh ballast; even though the macro void ratio of fresh ballast ( $e_B = 0.62$ ) is higher than that of recycled ballast ( $e_B = 0.53$ ). Higher  $\epsilon_p$  is likely due to the size and shape of recycled ballast particles compared to that of fresh ballast particles; however, the mineralogy of the ballast particle also may have played a role (Indraratna and Salim 2002). Barksdale and Itani (1989) showed that rounded particles are twice as susceptible to plastic deformation under cyclic loading when compared to crushed angular stones.

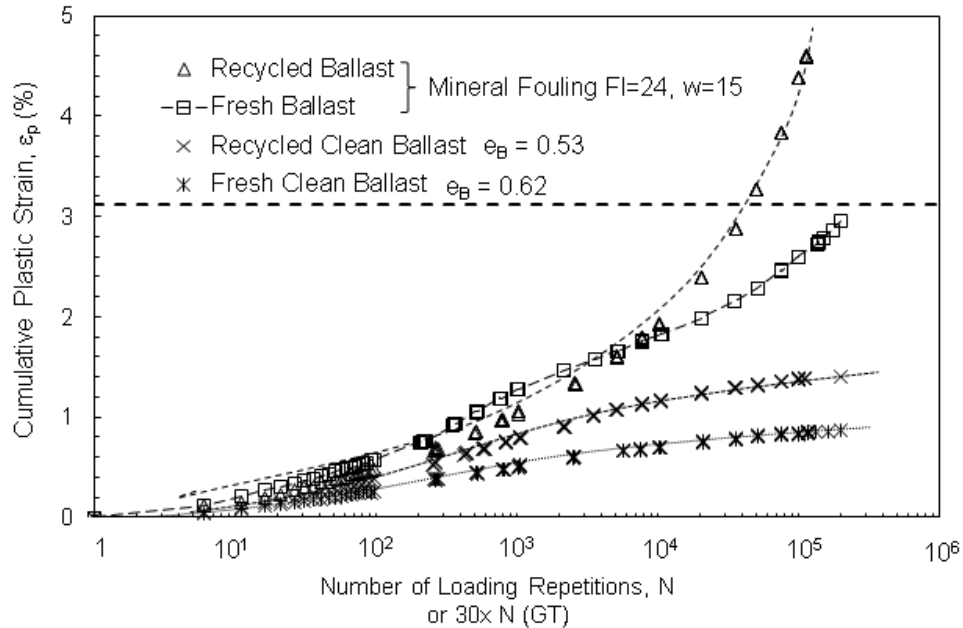


Figure 4.4 Accumulation of Plastic Strain of Fresh and Recycled Ballast in Clean and Fouled Condition

#### 4.6.2 Plastic Strain of Fresh and Recycled Ballast with Non-Cohesive Fouling Materials

Plastic strain responses of fresh and recycled ballast with mineral fouling are also shown in Fig. 4.4. Recycled ballast with mineral fouling experiences a large accumulation of  $\epsilon_p$  to reach nearly 5% at  $N = 2 \times 10^5$ , while fresh ballast in the same fouling condition showed  $\epsilon_p = 2.8\%$  at  $N = 2 \times 10^5$ . This behavior is likely affected by two main factors, size/shape of ballast particles and volume of voids in fresh and recycled ballast. Fresh ballast with high angularity tends to create a strong interlock between particles. Breakage and particle degradation (due to different mineralogy) is assumed to have small impact on the  $\epsilon_p$  of fouled ballast when  $N < 2 \times 10^5$ . The typical rate of fouling generation due to ballast deterioration is about 0.1%/MGT (data presented by Selig and Waters 1994). Thus, fouling content of ballast specimens was expected to change less than 0.5% during these test programs.

Macro pore space,  $e_B$ , of railway ballast in fresh and recycled ballast can also control the percentages of contaminated inter-particle surfaces. For fresh ballast with  $e_B = 0.62$ , approximately 25% by weight of mineral fouling is required to contaminate all contact points; i.e., assuming that fully fouled ballast is achieved when all void space is filled with mineral fouling. This ratio is about 20% for recycled ballast due to the smaller void ratio ( $e_B = 0.53$ ). Even though the lower  $e_B$  of recycled ballast created a denser skeleton, the lower  $e_B$  also led to more contaminated contact points in recycled ballast resulting in larger accumulation of  $\epsilon_p$ . This mechanical behavior is consistent with the current state of practice in the railway industry where highly angular ballast for railway track is specified (AREMA 2003). Even though the plastic deformation of fresh ballast was less than that of recycled ballast, the deformational behavior of fouled fresh ballast is only investigated further in this study, and future research is necessary to study the deformation of various types of ballast.

#### 4.6.3 Plastic Strain of Fresh Ballast with Non-Cohesive Fouling Materials

Plastic strain of fouled ballast was measured as a function of  $N$  for a wide range of fouling indices (FI) and water contents ( $w$ ). Plastic strains and semi-logarithmic rates of plastic strain ( $r_p = \frac{d\varepsilon_p}{\ln N}$ ) of fresh ballast mixed with mineral fouling at FI=12 and 24% are shown in Fig. 4.5 at  $w$  varying between 3 to 14%. Water content is the average of six samples from the various locations of the specimens after LSCT testing. The dashed horizontal line in these graphs is the plastic strain that corresponds to the contribution of ballast to the serviceability limit of deformation (i.e., 25 mm) used for Class5 freight track in the US (Federal Railroad Administration, FRA 2007) for maintenance program. For this criterion, ballast with 0.4-m thickness was assumed to contribute 40% of the allowable deformation limit of 25-mm for the entire track deformation.

Plastic strain and rate of plastic strain ( $r_p$ ) of fresh ballast mixed with coal fouling at FI=12 and 24 are shown in Fig. 4.6 for  $w$  between 3 to 14%. By increasing  $w$  and FI, the  $r_p$  increases significantly, thus increasing the  $\varepsilon_p$  of coal fouled ballast. As shown in Figs. 4.5 and 4.6, the  $\varepsilon_p$  of non-cohesive (i.e., mineral and coal) fouled ballast increases linearly in semi-log scale up to  $N=10^4$  during the initial compaction phase (ICP). This pattern was captured with constant  $r_p$ . The  $r_p$  is fairly constant up to  $N= 10^4$ , and the effect of fouling on  $\varepsilon_p$  of ballast is pronounced when ICP is passed. After ICP, the  $r_p$  increases linearly. This part of the deformational behavior of ballast is herein termed the 'fouling impact phase (FIP).'

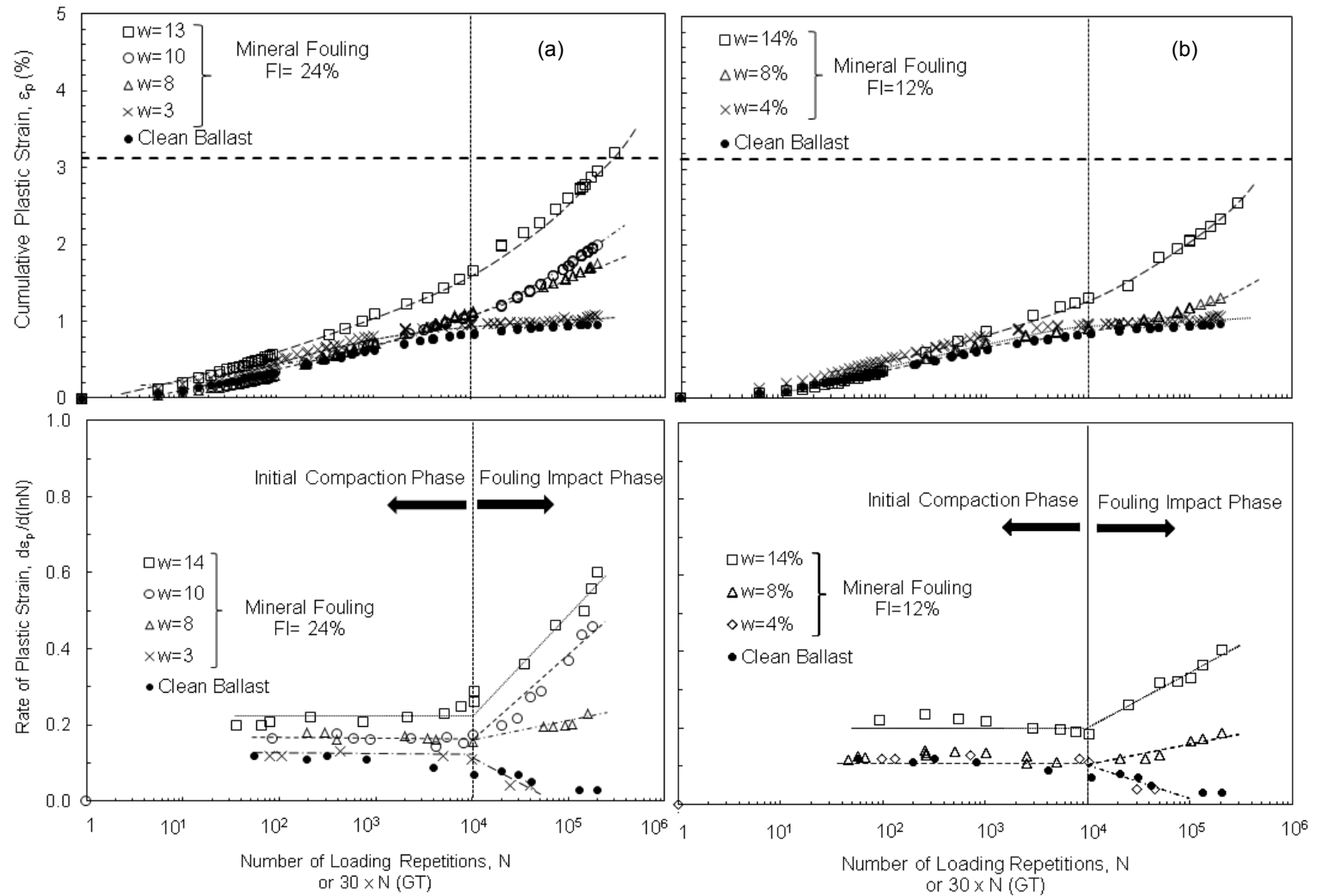


Figure 4.5 Accumulation of Plastic Strain and Rate of Plastic Strain as a Function of Number of Loading Repetitions for Mineral Fouling in FI=24% (a) and 12% (b)

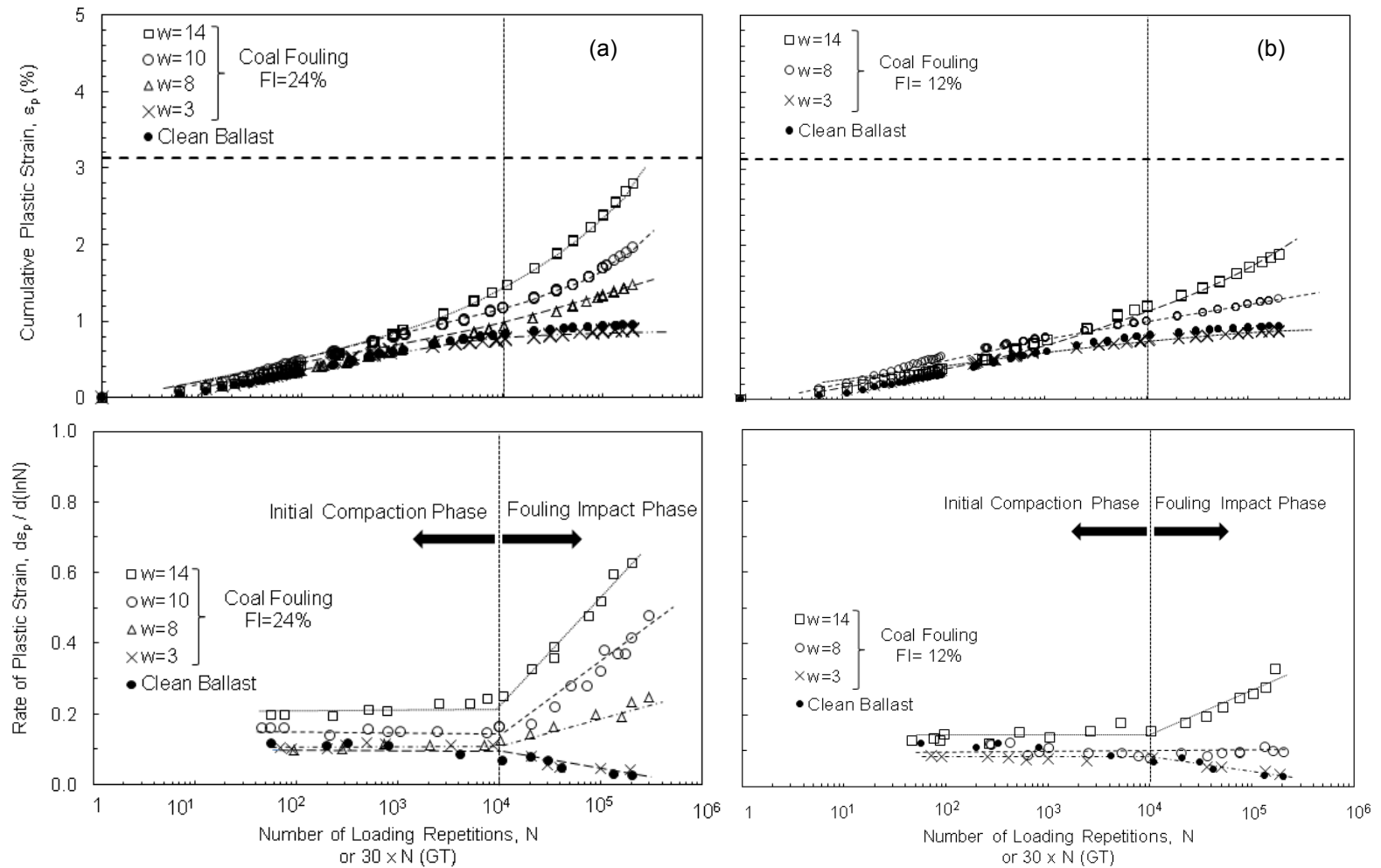


Figure 4.6 Accumulation of Plastic Strain and Rate of Plastic Strain as a Function of Number of Loading Repetitions for Coal Fouling in FI=24% (a) and 12% (b)

#### 4.6.3.1 Non-Cohesive Fouling Index (NFI)

Plastic strain at the end of the loading program; i.e., at  $N = 2 \times 10^5$ , is referred as  $\epsilon_{pu}$ . The  $\epsilon_{pu}$  of ballast mixed with non-cohesive fouling is listed in Table 4.3. The  $\epsilon_{pu}$  is plotted as a function of  $w$  and FI for non-cohesive fouling materials in Fig. 4.7a. The  $\epsilon_{pu}$  of ballast with coal and mineral fouling shows a similar linear trend with respect to  $w$  and FI. The  $\epsilon_{pu}$  of ballast for coal and mineral fouling is similar regardless of the type of fouling. The same mechanisms are assumed to occur for non-cohesive (i.e., coal and mineral) fouled ballast when the grain size distributions of fouling materials remain the same.

In Fig. 4.7a,  $\epsilon_{pu}$  increases linearly by increasing  $w$  for a given FI. Water content less than 3% does not affect the  $\epsilon_{pu}$  in the fouled ballast. Therefore, a non-cohesive fouling index (NFI) is proposed as:

$$NFI = \frac{FI(w - 3)}{100} \quad (\text{Eq. 4.5})$$

Eq. 4.5 accounts for the effects of  $w$  (%) and FI (%) together for non-cohesive fouling materials. The correlation between  $\epsilon_{pu}$  of ballast fouled with non-cohesive fouling materials and NFI is shown in Fig. 4.7b and expressed as:

$$\epsilon_{pu} = 0.7858 NFI + 0.98 \quad (\text{for } w > 3\%) \quad R^2 = 0.92 \quad (\text{Eq. 4.6})$$

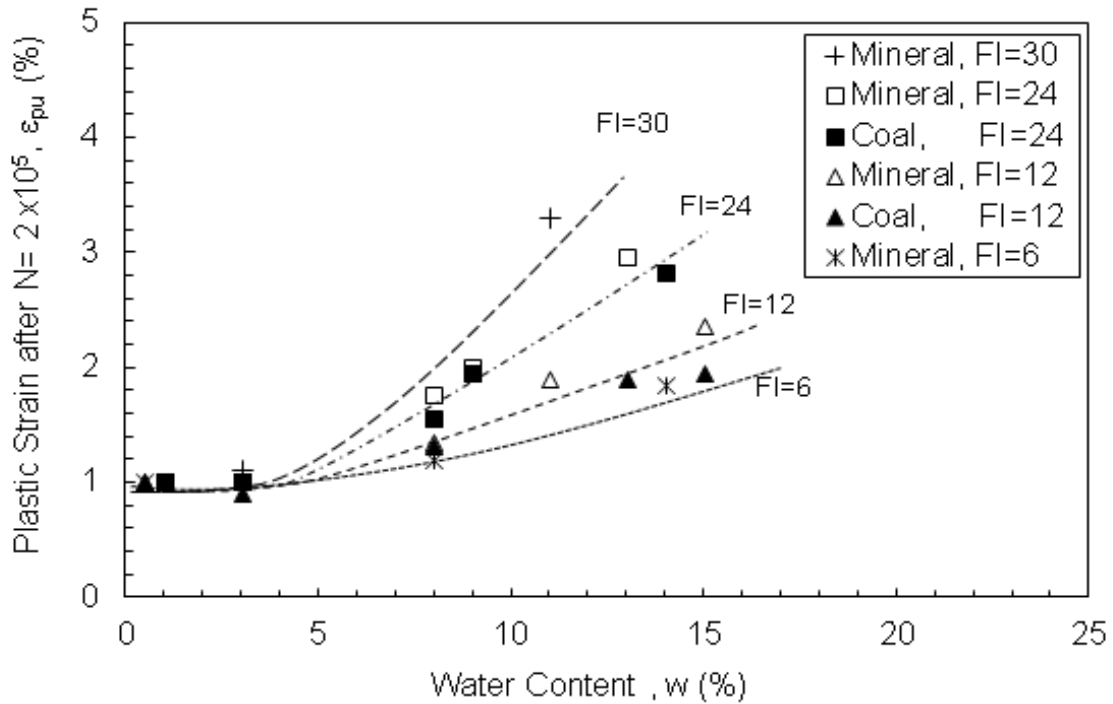
The average of  $\epsilon_p$  after ICP, shown in Figs. 4.5 and 4.6, is equal to 0.98 for all fouled ballast specimens and implemented in Eq. 4.5. This implies that the  $\epsilon_{pu}$  of fouled ballast in a dry condition ( $w < 3\%$ ) remains in the initial compaction phase. At  $w > 3\%$ ,  $\epsilon_p$  of fouled ballast increases linearly by NFI according to Eq. 4.6. This behavior implies that NFI increases the percentage of contaminated contact points in the ballast linearly, and consequently, increases the accumulation of  $\epsilon_p$ .

Table 4.3 Plastic Strain of Railway Ballast at  $N= 2 \times 10^5$  ( $\epsilon_{pu}$ ) for Non-Cohesive Fouling Materials

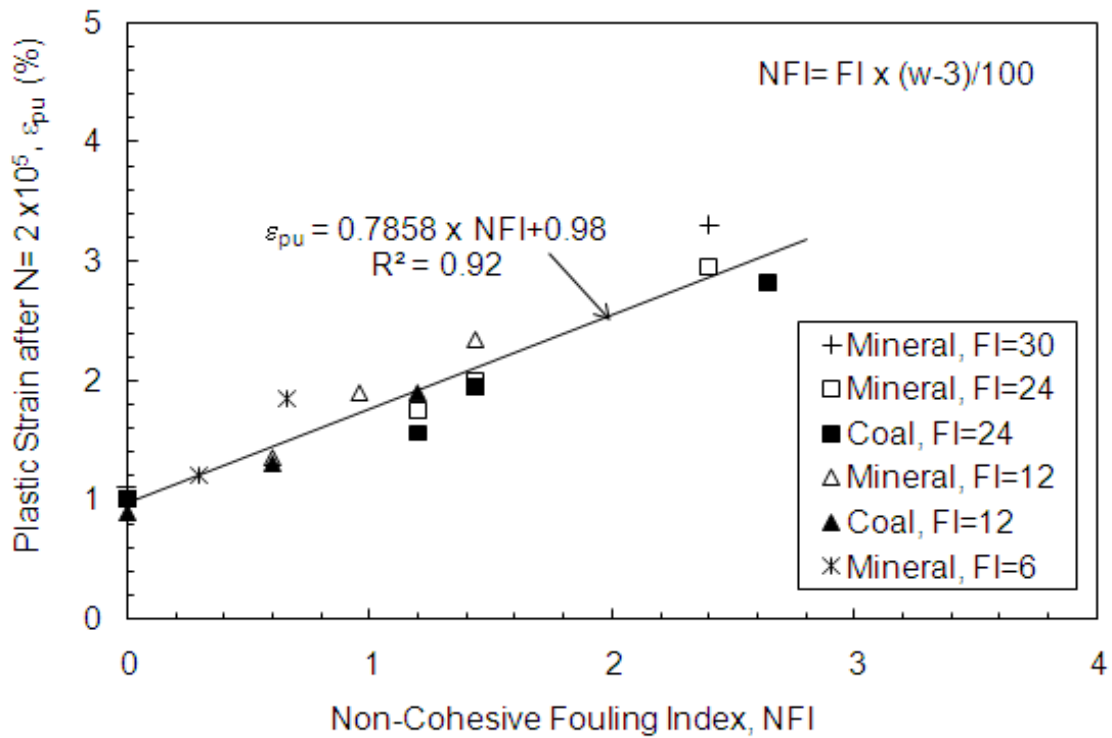
Mineral Fouling									Coal Fouling								
FI=30			FI=24			FI=12			FI=6			FI=24			FI=12		
W	$\epsilon_{pu}$	$e_B$	W	$\epsilon_{pu}$	$e_B$	W	$\epsilon_{pu}$	$e_B$	W	$\epsilon_{pu}$	$e_B$	W	$\epsilon_{pu}$	$e_B$	W	$\epsilon_{pu}$	$e_B$
14	-	-	13	2.95	0.65 (4%)	14	2.35	0.64 (3%)	14	1.85	0.64 (3%)	14	2.82	0.65 (4%)	14	1.95	0.65 (4%)
11	3.3	0.65 (4%)*	10	2	0.65 (4%)	11	1.90	0.64 (3%)	10	1.63	0.63 (1%)	9	1.95	0.65 (4%)	10	1.9	0.64 (3%)
8	-	-	8	1.75	0.64 (3%)	8	1.35	0.64 (3%)	8	1.2	0.63 (1%)	8	1.56	0.64 (3%)	8	1.31	0.64 (3%)
3	1.1	0.63 (1%)	3	1.1	0.64 (3%)	3	1.05	0.64 (3%)	3	1.01	0.63 (1%)	3	1	0.62 (0%)	3	0.9	0.63 (1%)

Note:  $e_B$  of clean fresh ballast is  $0.62 \pm 0.01$  for  $\gamma_{d \max} = 15.8 \pm 0.3 \text{ kN/m}^3$

\*(%): percentage of increase in the void ratio of only coarse ballast particles with fouling



(a)



(b)

Figure 4.7 Plastic Strain of Ballast after  $N=2 \times 10^5$  ( $\epsilon_{pu}$ ) as a Function of Water Content and Fouling Index (a) and Non-Cohesive Fouling Index (NFI) (b)

#### 4.6.3.2 Non-Cohesive (Mineral and Coal) Fouling Mechanisms

Non-cohesive fouling material by itself does not affect the  $\epsilon_p$  of ballast when fouling is nearly dry ( $w < 3\%$ ). This behavior might be due to (1) retention of relatively clean contact points of ballast at low

moisture condition and (2) higher strength properties of dry non-cohesive fouling in contact points of ballast; i.e., binding ballast particles. The relatively clean contacts are evidenced by the fact that  $e_B$  remains constant or slightly increases (increase in  $e$  of 0 to 3%, see Table 4.3). In contrast, increasing  $w$  of fouling from 3 to 14% causes  $e_B$  to increase by 3 to 4% compared to  $e_B$  of clean ballast, implying more contamination with wetter and weaker fouling material.

Higher FI in ballast may tend to create thicker lenses of contaminated contact points that can be compressed or squeezed out during cyclic loading, resulting in overall plastic deformation of fouled ballast. The loss of shear strength in non-cohesive granular materials, such as silt and sand, under cyclic loading due to generation of excess pore water pressure is well established (Kramer 1996). Assuming that the contact surface of a particle covers about 3 to 10% of the entire surface (Lambe and Whitman 1969), non-cohesive mineral fouling that is trapped at the contact points of ballast is likely to be compacted to the  $\gamma_d$  of 20 kN/m<sup>3</sup> (standard Proctor maximum unit weight) and saturated at  $w=13\%$ . Therefore, increasing  $w$  (e.g.,  $w > 8\%$ ) of fouling in contaminated contact points of ballast can increase the potential of excess pore water generation, resulting in accumulation of plastic strain of ballast under cyclic traffic loading, as shown in Figs. 4.5 and 4.6.

#### 4.6.4 Plastic Strain of Fresh Ballast with Cohesive Fouling Material

Fouled ballast specimens with 20% by weight of cohesive fouling were tested to investigate the impact of various factors on the accumulation of  $\epsilon_p$  (i.e., ~80% of contact points of ballast are likely contaminated by 20% fouling). Specimens of fresh railway ballast with Clay L (low plasticity) and Clay H (high plasticity) were prepared at  $w=14\%$  and  $\epsilon_p$  was measured during the cyclic loading in the LSCT. As shown in Fig. 4.8, the specimens exhibit only the ICP with stabilization of  $\epsilon_p$  at larger  $N$ , regardless of the type of clay fouling. The presence of fouling in the contact points of ballast was studied by comparing  $e_B$  of fouled ballast with  $e_B$  of clean ballast. As listed in Table 4,  $e_B$  of ballast with cohesive fouling increases about 4 to 6% compared to the  $e_B$  of fresh ballast, indicating the potential for cohesive fouling being present at the contact points. To further investigate the presence of cohesive fouling at the ballast contact points, strength properties of cohesive fouling in the contact points of ballast were changed. Vanapalli et al. (1996) described that an increase in  $w$  of clay decreases the shear strength. Therefore, water was added to reach  $w = 14\%$  from the top of the fouled ballast specimen without disturbing the arrangement of ballast particles in the specimens. As shown in Fig. 4.8, increasing  $w$  from 14 to 24% accelerates the accumulation of  $\epsilon_p$  in ballast fouled with Clay L (~ 5 times larger than the  $\epsilon_p$  in ICP) and ballast fouled with Clay H (~ 2.5 times larger than the  $\epsilon_p$  in ICP). At  $w=24\%$ , FIP is pronounced. To systematically evaluate the effect of cohesive fouling on  $\epsilon_p$  of ballast, P200 of fouling between 5 and 90% of total fouling (i.e., fraction P4) was considered. LL changes from 20 to 64 by increasing P200 from 5 to 90% to account for a wide range of LL for cohesive clay fouling. The accumulation of  $\epsilon_p$  of ballast in various cohesive fouled ballast specimens is summarized in Table 4 and displayed in Fig. 4.9. After ICP is reached in the first  $N=2 \times 10^5$  (i.e., ballast at low water content (Table 4.4) where FIP was not observed), the accumulation of  $\epsilon_p$  increases and is different for different fouling conditions.

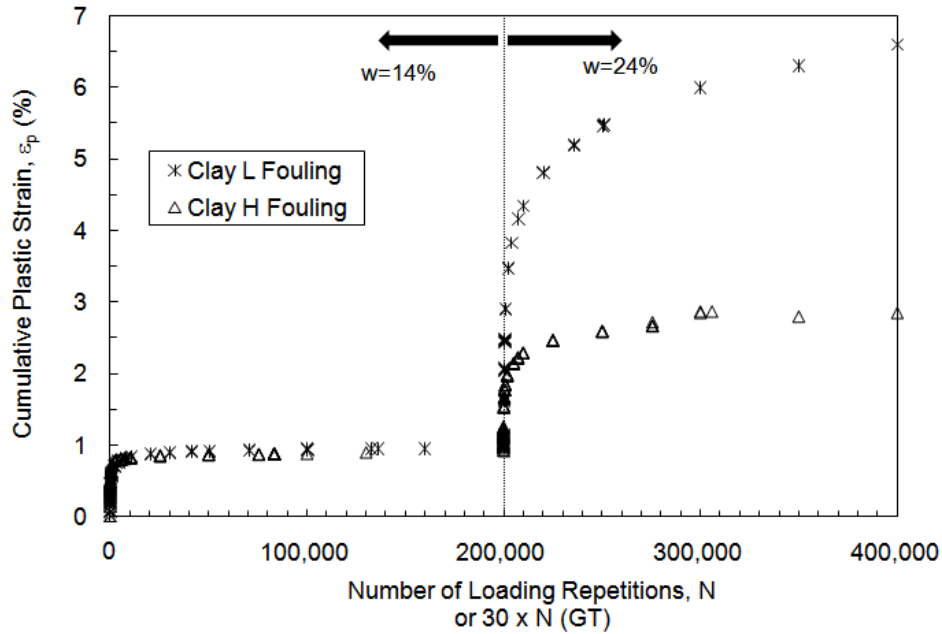


Figure 4.8 Accumulation of Plastic Strain of Fouled Railway Ballast in Arithmetic-Scale with Cohesive Fouling Materials and Moisture

Table 4.4 Plastic Strain of Railway Ballast at  $N=2 \times 10^5$  ( $\epsilon_{pu}$ ) for Cohesive Fouling Materials

Nomenclature P200/LL/PI	90/36/19	90/28/6	60/64/42	40/38/22	30/30/14	20/21/NP	10/20/0
FI (%)	38	38	31.6	28	26	24	22
Initial Moisture in ICP	14	13	14	14	13	10	NA
w	25	24	23	18	16	15	14
$(1+w-LL) \times PI$	0.2	0.1	0.22	0.2	0.1	0.04	0
$e_B$	0.65 (5%)*	0.65 (5%)	0.66 (6%)	0.65 (4%)	0.66 (6%)	0.66 (6%)	0.66 (6%)
$\epsilon_{pu}$	5.8	1.7	1.93	1.4	0.9	0.9	0.8

Note1: P4= %<4.75mm, P200= %<0.075mm, w=water content of specimen, LL = liquid limit, PL = plastic limit.

Note2:  $e_B$  of clean fresh ballast is  $0.62 \pm 0.01$  for  $\gamma_{d \max} = 15.8 \pm 0.3 \text{ kN/m}^3$

\* (%): percentage of increase in the void ratio of only coarse ballast particles with fouling

For the two cohesive fouled ballast specimens with P200 = 90%, fouling with higher PI exhibit a significant increase in  $\epsilon_p$ . However, cohesive fouling with higher PI does not necessarily result in the largest  $\epsilon_p$ , while P200 and moisture content also have a significant role on  $\epsilon_p$  of ballast (compare 60/21/72/23 to 90/17/36/25, nomenclature in Fig. 4.9). Therefore, multiple factors in cohesive fouling change the shear strength properties of cohesive fouling, and consequently,  $\epsilon_p$  of ballast. Fig. 4.9 shows that, in addition to moisture, compositional characteristics of cohesive fouling, such as Atterberg limits and P200, are important factors controlling the deformational behavior of railway ballast.

#### 4.6.4.1 Cohesive Fouling Index

Significance of Atterberg limits, P200, and moisture on the plastic deformation of ballast were studied in a series of LSCT tests on cohesive fouled ballast. Fouling index is used to evaluate the correlation between the conventional fouling term (proposed by Selig and Waters 1994) and the  $\epsilon_{pu}$  of ballast. Increasing FI from 24 to 40 in cohesive fouling increases the accumulation of  $\epsilon_{pu}$  of fouled ballast from 1 to 6%. The same behavior is observed for the effect of P200. The  $\epsilon_p$  of cohesive fouled ballast is not solely dependent on  $w$  of fouling materials. However, the effect of moisture on deformational behavior of cohesive fouled ballast is dependent on the  $w$  relative to LL and PI of fouling material. A multi variable regression analysis was conducted to correlate  $\epsilon_{pu}$  to LL, PI,  $w$ , P200, and FI. The following regression equation was obtained:

$$\epsilon_{pu} = 0.063 \exp(5.57 \text{ CFI}) \quad R^2=0.91 \quad (\text{Eq. 4.7})$$

where cohesive fouling index (CFI) is introduced as,

$$\text{CFI} = \text{FI} \times \text{CMI} \times \frac{\text{P200}}{\text{P4}} \quad (\text{Eq. 4.8})$$

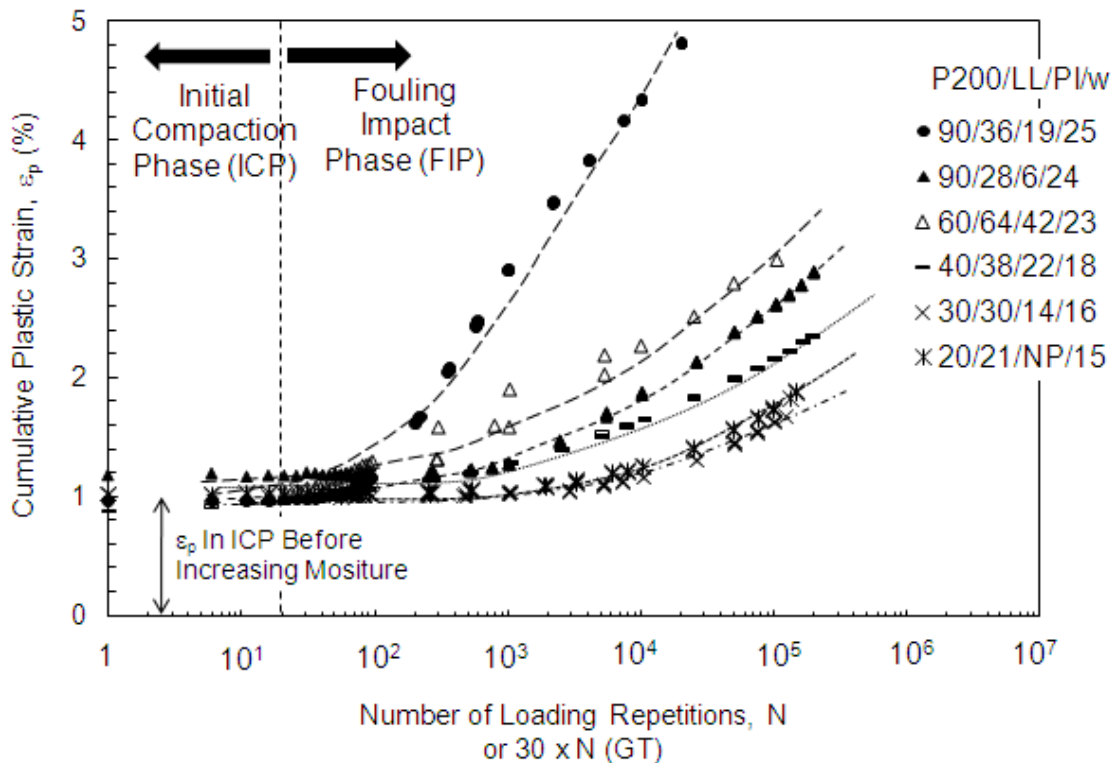


Figure 4.9 Accumulation of Plastic Strain of Ballast Fouled with Cohesive Fouling Materials after Moisture was Added in  $N= 2 \times 10^5$  (see Fig. 4.8)

CFI includes the impact of FI (%), cohesive-fouling moisture index (CMI), and fines content (P200/P4, %). The CMI was defined to incorporate the effect of index properties of fouling materials (i.e., LL and PI) and  $w$ :

$$\text{CMI} = (1+w-\text{LL}) \times \text{PI}^{0.5} \quad (\text{Eq. 4.9})$$

where  $w$ ,  $\text{LL}$ , and  $\text{PI}$  are in  $\%/100$ . The term of  $(1+w-\text{LL})$  represents the moisture level with respect to the liquidity limit of fouling materials. The correlation between  $\epsilon_{pu}$  and CFI is shown in Fig. 4.10. The CFI increases by increasing  $(w-\text{LL})$ ,  $\text{PI}$ ,  $\text{P200}$ , and  $\text{FI}$ . Increasing the CFI exponentially increases the  $\epsilon_{pu}$ . Cohesive fouling index presented herein is expected to be a useful term to account for the significant factors affecting the  $\epsilon_p$  of ballast in the presence of cohesive fouling.

#### 4.6.4.2 Cohesive (Clay) Fouling Mechanisms

The mechanisms by which cohesive fouling material affects the  $\epsilon_p$  of ballast are similar to those in non-cohesive fouling material but is further complicated by the cohesive nature and the very small particle size of clay and silt compared to ballast particles. Cohesive fouling creates fouling contamination at ballast particle contacts, as confirmed by an increase of  $e_B$  of ballast (about 4 to 6%), as given in Table 4.4. As also listed in Table 4.4, cohesive fouled ballast at relatively low water content only shows the ICP, likely due to high shear strength properties of fouling at the contact points. Soft cohesive fouling material is expected to be compacted or squeezed out of the contact points of ballast under cyclic loading. The plastic strain behavior of the fouled ballast with cohesive fouling material essentially follows the deformational behavior of cohesive soils; i.e.,  $\epsilon_{pu}$  depends on CFI and the factors included in this index.

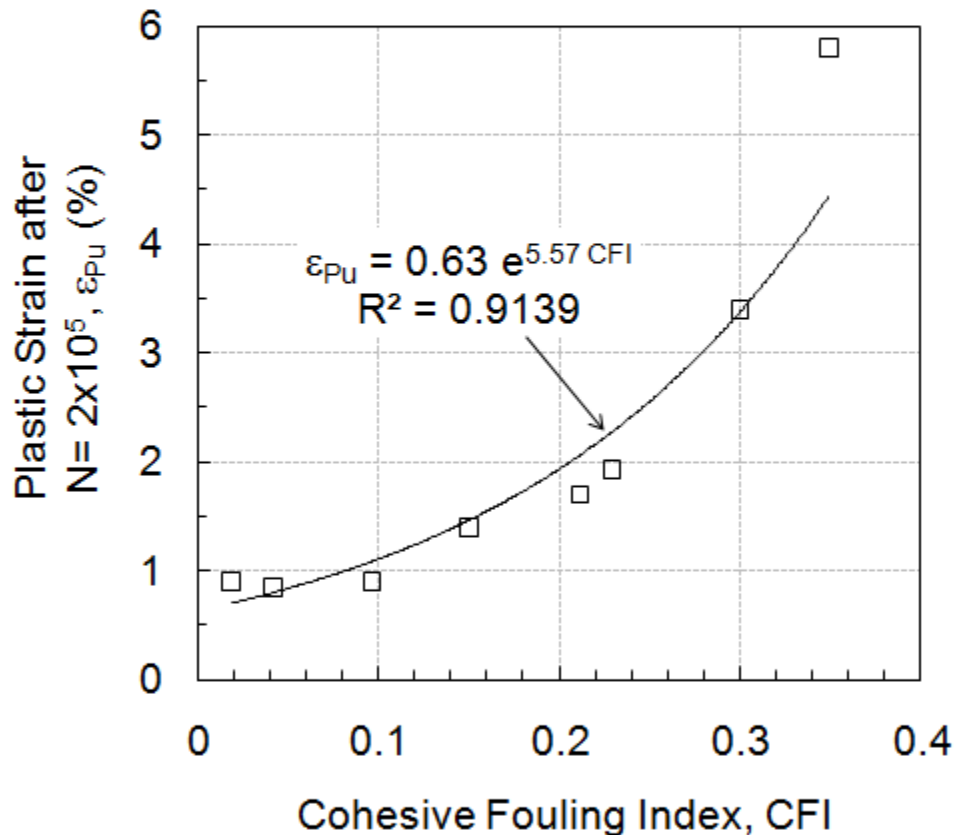


Figure 4.10 Correlation between Plastic Strain of Fouled Ballast and Cohesive Fouling Index (CFI)

#### 4.6.5 Suction Control of Cohesive and Non-cohesive Fouling

Contaminated contact points appear to be the main cause of increase in  $\epsilon_p$  of ballast under cyclic loading. Therefore, deformational behavior of both cohesive and non-cohesive soil is dependent on moisture state among other factors. Moisture state is characterized by volumetric water content and soil suction for unsaturated soil. To demonstrate this effect, a series of soil water characteristic curves (SWCC) of fouling material were performed in accordance with ASTM D6836. As shown in Fig. 4.11, the

deformational behavior of fouled railway ballast can be explained by the suction control of unsaturated fouling material. Fig. 4.11 demonstrates that mineral fouling at  $w < 3\%$  and cohesive fouling at low  $w$  exhibit only the initial compaction phase. A suction-related limit for fouling material is proposed to distinguish between ICP and FIP in the deformational behavior of fouled ballast. Fouled railway ballast with water contents less than those that generate soil suction greater than 2,000 kPa tend to exhibit only ICP, whereas for suctions less than 2,000 kPa, the behavior essentially starts with the ICP and continues with the FIP (i.e., increase in rate of plastic strain) irrespective of the fouling type.

#### 4.6.6 Effect of Tamping on Plastic Strain of Fouled Ballast

In addition to the fouling-related factors presented above, tamping also impacts the  $\varepsilon_p$  of ballast by rearranging the particles during the maintenance of railways. Therefore, ballast loses the dense structure achieved during traffic loading as a result of tamping activities. Zaayman (2006) described that ballast deforms abruptly after maintenance when the main source of deterioration (fouling) has not been solved properly. In Fig. 4.12,  $\varepsilon_p$  of ballast fouled with high plasticity clay (Clay H fouling, 20% by weight) is shown at different moisture and maintenance conditions. Increasing  $w$  from 13 to 19% considerably increases the  $\varepsilon_{pu}$  of ballast from 1 to 2.8%. At  $N=4 \times 10^5$ , ballast was tamped by re-compacting the sample at the existing moisture content ( $w=19\%$ ). Tamping eliminated the plastic deformation of ballast by rearranging the particles. Tamping also causes the unit weight of ballast to decrease from 15.6 to 15.0  $\text{kN/m}^3$ , that causes lower density for fouled ballast and higher potential of plastic deformation under cyclic loading. Lower unit weight of the highly cohesive fouled ballast after tamping is attributed to prevention of effective compaction of ballast due to the presence of fouling in the particle contacts and ballast voids. However, after tamping,  $\varepsilon_p$  increases at a higher rate due to the larger  $e_B$  (~ 4% larger than  $e_B$  of fouled ballast before tamping). At  $N=6 \times 10^5$ , ballast was moisturized to reach to  $w=25\%$ . An abrupt increase in  $\varepsilon_p$  was again observed likely due to increased moisture content reducing the shear strength of the clay fouling at the ballast contact points. Fig. 4.12 shows the influence of a proper maintenance activity in railway track. In a high fouling condition, tamping temporarily solves the problem of uneven surfaces but shortens the long-term serviceability of the railway track.

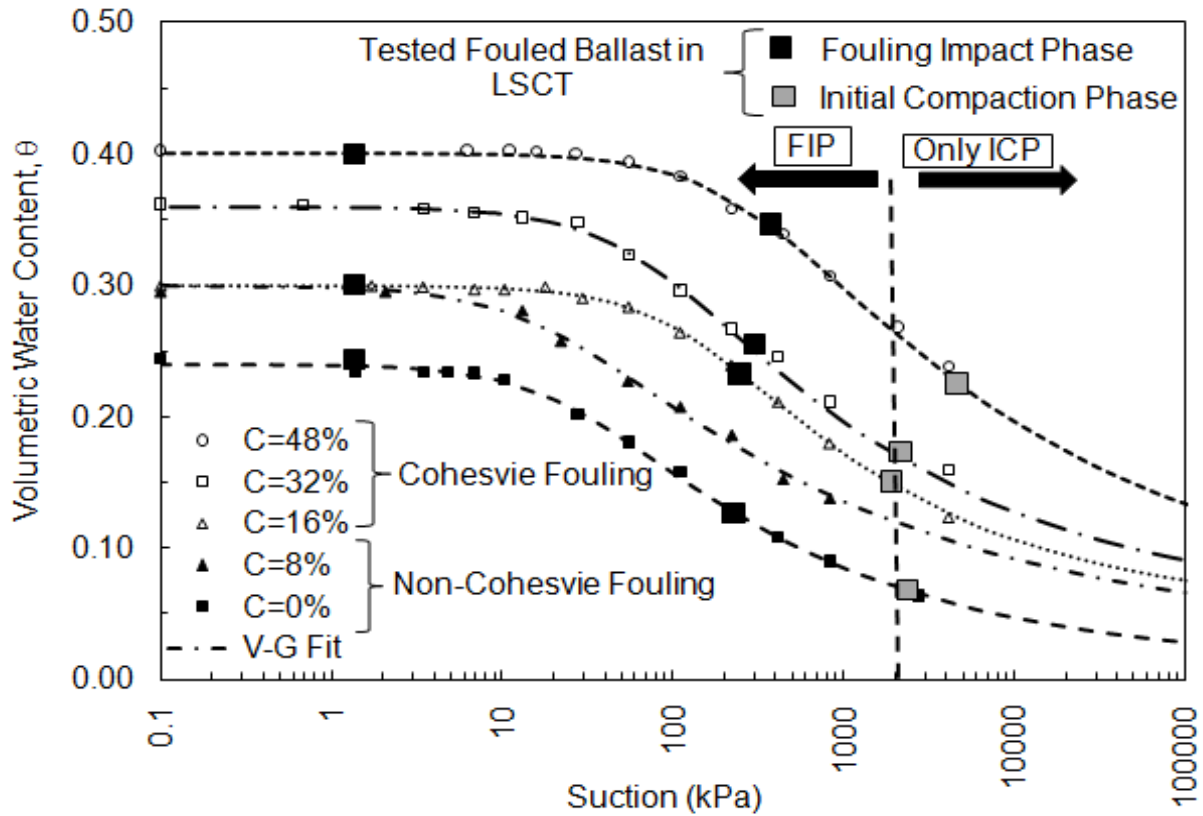


Figure 4.11 Defined Zone for Deformational Behavior of Fouled Ballast in ICP and FIP in the Soil Water Characteristics Curves of Fouling Materials (Note: C=clay fraction)

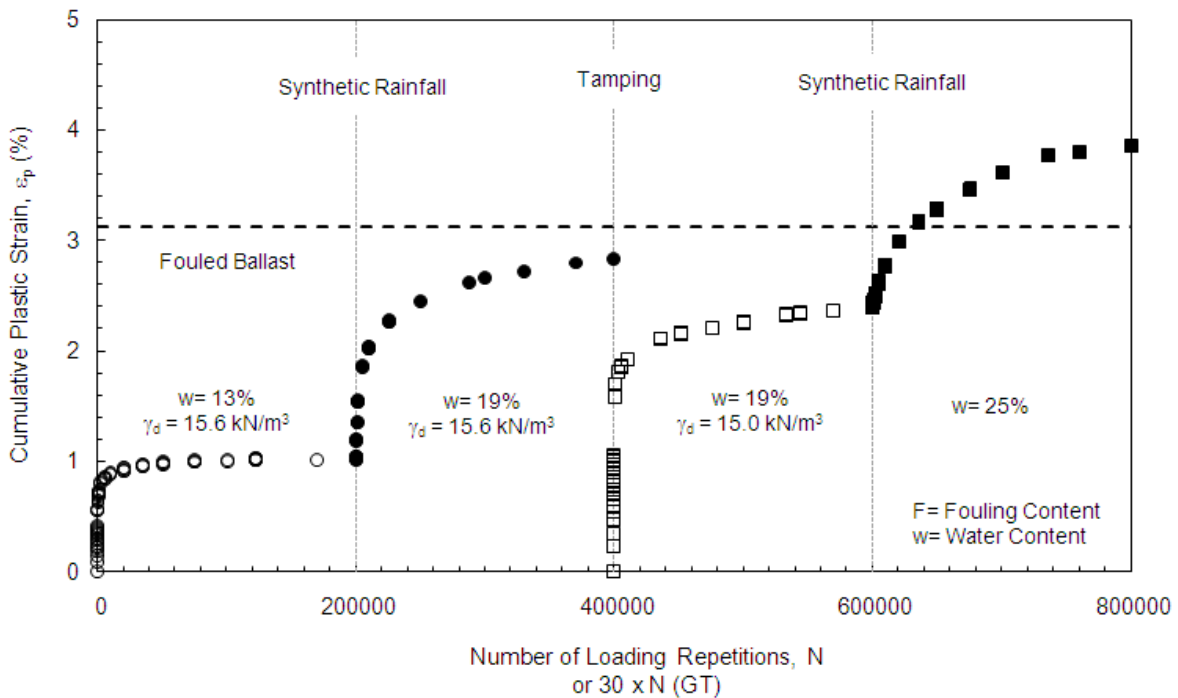


Figure 4.12 Simulation of Rainfall and Tamping in Highly Fouled Ballast

## 4.7 CONCLUSIONS

In this paper, the effect of fouling (internally generated mineral fouling, external coal fouling due to surface spillage, and clay fouling due to subgrade intrusion) on the permanent deformational behavior of ballast under traffic loading was studied. The experimental study was conducted using a large-scale cyclic triaxial apparatus at a representative field stress condition of 90 kPa confining stress and 300 kPa cyclic deviator stress. Fouling ranging from 0 to 25% by weight with water contents ranging from 0 to 30% were tested. Large-scale cyclic triaxial test results showed that increased fouling and moisture increases the accumulation of plastic strains ( $\epsilon_p$ ) in ballast.

Two main phases were distinguished in the development of  $\epsilon_p$  with loading cycles in fouled ballast: (1) initial compaction phase (ICP), where the  $\epsilon_p$  of ballast steadily increases to a certain point ( $N < 10,000$ ) and (2) fouling impact phase (FIP), where the  $\epsilon_p$  and the rate of plastic strain of ballast increases due to the presence of fouling materials (or remains stable in the absence of fouling). For non-cohesive (mineral and coal) fouling, fouling index and moisture were the controlling parameters. A non-cohesive fouling index (NFI) was introduced to account for the factors affecting the  $\epsilon_p$ . For cohesive (clay) fouling, in addition to fouling index and moisture, Atterberg limits (PL and LL), and % of P200 were identified as controlling parameters. A cohesive fouling index was introduced to account for these factors. A limit for deformational behavior of fouled ballast was illustrated using a suction-based criteria. For the representative state of stress for ballast, fouling materials, irrespective of type, with suction greater than 2,000 kPa only show the initial compaction phase.

The main mechanism for accumulation of plastic strain in ballast is contaminated contact points of large ballast particles by the fouling material. Fouling at contaminated contact points can be compressed or squeezed out during cyclic loading, resulting in accumulation of plastic deformation. Also, decreased shear strength of fouling materials at the contact points under cyclic loading increases the  $\epsilon_p$  of ballast in cohesive and non-cohesive fouling.

The effect of maintenance on  $\epsilon_p$  was studied. Ballast in a highly fouled condition exhibits extensive  $\epsilon_p$  immediately after tamping due to rearrangement of the particles and loss of dense condition that has been achieved in previous traffic loading. In a high fouling condition, tamping temporarily solves the problem of uneven surfaces but shortens the long-term serviceability of the railway track. The results of this study produced the essential data to account for typical fouling conditions in the railway track to provide a basis in planning the maintenance activities.

## ACKNOWLEDGEMENT

Funding for this research was provided by the National Center for Freight and Infrastructure Research and Education (C-FIRE). Mr. Steven Chrismer (Amtrak) provided a valuable review for the presented materials. Andrew Keene and Evan Thomas assisted during the laboratory works. Xiadong Wang (Soil Mechanics Laboratory) and William Lang (Structural and Material Laboratory) of the University of Wisconsin-Madison assisted with the experimental setups for the cyclic triaxial testing; their assistance is gratefully acknowledged. Assistance from the BNSF Railway and Wisconsin and Southern Railroad Company for providing the ballast is appreciated.

## REFERENCES

- AREMA, 2003, *Manual for Railway Engineering*, American Railway Engineering Association, Washington, D.C
- Ahlf, R.E., 2007, *Railway Track Systems: Engineering and Design, Unpublished and Personal Communication*
- Barksdale, R.D. and Itani, S.Y., 1989, Influence of Particle Shape on Base Behavior, *Trans. Res. Rec.*, National Research Council, Washington, D.C., 1227, pp.173-182
- Chrismer, S., and Davis, D., 2000, Cost Comparisons of Remedial Methods to Correct Track Substructure Instability, *Trans. Res. Rec.*, 1713, pp.10-15
- Darell, D.D., 2003, Substructure Can Add Life to Rail and Ties, *Railway Track and Structures*, 99(3), pp. 25–27
- Edil. T.B., Krizek, R.J., and Zelasko, J., 1975, Effect of Grain Characteristics on Packing of Sands, *Proc. of the Istanbul Conf. on Soil Mechanics and Foundation Eng.*, Istanbul, Turkey, Vol. I, pp. 46-54

- Federal Railroad Administration (FRA), 2007, *Track Safety Standards Compliance Manual*, USDOT, Washington D.C
- Haque A., Kamruzzaman, A., Christie, D., Bouazza, A.M., 2008, Towards a Better Design Guideline of Subballast Materials for Filtration Purpose Under Cyclic Load, *Proc. of Conf. Railway Eng.*, Perth, Australia, pp.611-617
- Huang, H., Tutumluer, E., Dombrow, W., 2009, Laboratory Characterization of Fouled Railroad Ballast Behavior, *88th annual Mtg. of Trans. Res. Board*, on CD-ROM
- Indraratna, B., Salim, W., 2002, *Mechanics of Ballasted Rail Tracks: A Geotechnical Perspective*, Taylor & Francis Group plc, London, UK
- Indraratna, B., Nimbalkar, S., Christie, D., Rujikiatkamjorn, C., Vinod, J., 2010, Field Assessment of the Performance of a Ballasted Rail Track With and Without Geosynthetics, *J. of Geotech. & Geoenv. Eng.*, 136(7), pp.907-1008
- Ionescu, D., 2004, Ballast Degradation and Measurement of Ballast Fouling, *7<sup>th</sup> Railway Eng. Conf.*, Commonwealth Institute, London
- Kuerbis, R. H., Vaid, Y. P., 1990, Corrections for Membrane Strength in the Triaxial Test, *Geotechnical Testing J.*, GTJODJ, 13(4), pp.361-369
- Kramer, S.L., 1996, *Geotechnical Earthquake Engineering*, Prentice Hall, First Edition
- Lambe and Whitman, 1969, *Soil Mechanics*, John Wiley and Sons, NY
- Lee, H. M., 2009, Ballast Evaluation and Hot Mixed Asphalt Performance, *Proc. BCR2A Conf.*, Univ. of Illinois Urbana-Champaign, Urbana, IL, pp.1283-1289
- Liu, J., and Xiao, J., 2010, Experimental Study on the Stability of Railroad Silt Subgrade with Increasing Train Speed, *J. of Geotech. & Geoenviron. Eng.*, ASCE, 136(6), pp.833-842
- Polito, C.P., and Martin II, J.R., 2001, Effects of Nonplastic Fines on the Liquefaction Resistance of Sands, *J. of Geotech. & Geoenviron. Eng.*, ASCE, 127(5), pp.408-415
- Selig, E.T., and Waters, J.M., 1994, *Track Geotechnology and Substructure Management*, Thomas Telford, NY
- Thevanayagam, S., and Martin, G.R. 2002, Liquefaction in Silty Soils - Screening and Remediation Issues, *Soil Dynamics and Earthquake Eng.*, 22, pp.1035-1042
- Vanapalli, S.K., Fredlund, D.G., Pufahl, D.E., and Clifton, A.W. 1996, Model for the Prediction of Shear Strength with Respect to Soil Suction, *Can. Geotech. J.*, 33, pp.379-392.
- Zaayman, L., 2006, Ballast Cleaning, a Prerequisite for a Sustainable, Reliable, Safe and Cost Effective Railway Track," *Magazine of the South African Ins. of Civil Eng.*, 14(5), pp.20-24

## CHAPTER 5: DETECTION OF FOULING IN BALLAST BY ELECTROMAGNETIC SURVEYING

### 5.1 ABSTRACT

During the service life of railway tracks, particle breakage, surface intrusion, and infiltration of fines from subgrade caused by traffic loading increase the amount of fines in ballast. This process is known as 'fouling'. Fouling increases plastic deformation of ballast, which leads to the early deterioration of track surfaces. To avoid progressive deterioration of the track, continuous and prompt maintenance is required when fouling approaches a critical level. Maintenance operations are scheduled on the basis of measured track deformation and the level of fouling. Recently, electromagnetic surveying and visual observation through boreholes have been proposed to detect and quantify the fouling content. However, systematic studies are required to validate the application of electromagnetic-based techniques in the quantification of fouling levels in the rail substructure. The change of electromagnetic parameters in simulated fouling processes was evaluated in a small-scale laboratory study using time domain reflectometry (TDR). An increase of fouling depth increased the relative real dielectric permittivity from 1.2 to 2.0 while the increase in water content of the fouling material from 5 to 10% increased the electrical conductivity of fouled ballast from 10 to 24 mS/m. The TDR results were combined to develop a qualitative approach to assess the gradual change of fouling content of ballast.

### 5.2 INTRODUCTION

Ballast is the large-size aggregate layer in railway substructure that distributes the loads on the track to the foundation soil and provides proper drainage to the track structure. Unlike base layers in pavement structures, railway ballast breaks and deteriorates under the cyclic loads from trains. Throughout this deterioration process, ballast properties deviate from the specifications and form 'fouled ballast'. Fouling starts with internal degradation of the ballast, and continues with subgrade infiltration and surface spillage (Selig and Waters 1994; Darell 2003; Chrismer and Read 1994; Descantes et al 2006; Zaayman 2006). A major concern facing the US freight rail transportation industry is high maintenance costs due to heavy freight loads and substandard track substructure (Lee 2009). Proper maintenance of railway track is confounded by inadequate non-destructive techniques to estimate the condition of track (Al-Qadi et al. 2008). In the US, there are over 371,200 km of railroad track that must be periodically assessed (Al-Qadi et al. 2008). The current assessment methods include forensic investigations of the track and use of ground penetrating radar (GPR –Clark et al. 2001; Huang et al. 2009; Raymond 1986). As the amount of fouling increases in the ballast layer, GPR images a reduced thickness of track bed (Al-Qadi et al. 2008; Clark et al. 2001). However, as ballast becomes progressively more fouled and retains more moisture, the reflection becomes less defined and horizons become more difficult to track. GPR studies illustrate the difficulties in data interpretation and the sensitivity to the water content of fouled ballast (Al-Qadi et al. 2008; Clark et al. 2001; Jack and Jackson 1998). Studies by Ebrahimi et al. (2010) showed that the fouling content and moisture increased the plastic deformation of track and significantly affect the long-term performance of the track.

The objective of this paper is to characterize electromagnetic (EM) parameters of fouled ballast using time domain reflectometry (TDR) methodology to assess the depth of fouling and moisture content of fouled ballast. Two main sources of fouling, including internal ballast crushing (i.e., 'mineral fouling') and surface spillage of coal dust (i.e., 'coal fouling') were tested. The correlation between the EM properties of ballast with a gradual increase in the depth of fouling was derived.

### 5.3 EM WAVE PROPAGATION AND TDR MEASUREMENTS

In TDR measurements, an electromagnetic (EM) step voltage is propagated along the length of TDR probes. The time and the amplitude required for the EM wave to propagate and reflect back to the source is measured and, if the geometry of the probes is known, the dielectric permittivity and electrical conductivity of the material between the probes can be estimated.

The propagation velocity ( $V$ ) of an EM wave depends on the electrical conductivity ( $\sigma$ ), complex dielectric permittivity ( $\epsilon = \epsilon' - j\epsilon''$ ), and complex magnetic permeability ( $\mu = \mu' - j\mu''$ ) of the medium (Santamarina 2001). If the material is assumed to be non-ferromagnetic (i.e.,  $\mu = \mu_0$  where  $\mu_0 = 4\pi \cdot 10^{-7}$  H/m is the magnetic permeability of free space) and the imaginary component of the dielectric permittivity is assumed negligible (i.e.,  $\epsilon'' \ll \sigma/\omega$ ), the EM wave velocity is:

$$V = \frac{c_0}{\sqrt{\frac{1}{2} \cdot \left[ \varepsilon_r' + \sqrt{\varepsilon_r'^2 + \left( \frac{\sigma}{\omega \cdot \varepsilon_0} \right)^2} \right]}} \quad (\text{Eq. 5.1})$$

where  $c_0=1/(\sqrt{\varepsilon_0 \cdot \mu_0})$  is the EM wave in free space,  $\varepsilon_0 (=8.85 \cdot 10^{-12} \text{ F/m})$  is the dielectric permittivity of the free space, and  $\varepsilon_r (= \varepsilon'/\varepsilon_0)$  is the relative real dielectric permittivity. If the electrical conductivity of the material is small with respect to the relative real dielectric permittivity ( $\sigma/\omega \ll \varepsilon'$ ), Equation 5.1 simplifies to:

$$V = \frac{c_0}{\sqrt{\varepsilon_r'}} \quad (\text{Eq. 5.2})$$

In TDR measurements, the relative real dielectric permittivity of the material between the probes can be determined by measuring the travel time along the length of the probe. Assuming low electrical conductivity and non-ferromagnetic materials, the relative real dielectric permittivity is:

$$\varepsilon_r' = \left( \frac{c_0 \cdot t}{2 \cdot L} \right)^2 \quad (\text{Eq. 5.3})$$

where  $t$  is the two-way travel time for the pulse along the length ( $L$ ) of the TDR probe. The two-way travel time is measured from abrupt changes in slopes of the TDR waveforms. For an electromagnetic TDR voltage pulse of magnitude ( $V_T$ ) traveling in a conductive material the reflected voltage ( $V_R$ ) can be described as (O'Connor and Dowding 1999):

$$V_T = V_R e^{-2\alpha L} \quad (\text{Eq. 5.4})$$

where  $\alpha$  [1/m] is the attenuation coefficient and, for non-ferromagnetic material, can be approximated as (O'Connor and Dowding 1999; Dalton et al. 1984):

$$\alpha = \frac{\sigma}{2} \sqrt{\frac{\mu_0 \mu_r}{\varepsilon_0 \varepsilon_r}} = 60 \Omega \cdot \pi \frac{\sigma}{\sqrt{\varepsilon_r'}} \quad (\text{Eq. 5.5})$$

where  $\sigma$  [S/m] is the electrical conductivity of the material along the TDR probes. Giese and Tiemann (Giese and Tiemann 1975) proposed that the electrical conductivity from a TDR waveform could be determined from the characteristic impedance of the probe ( $Z_p$ ) and the cable tester out impedance ( $Z_c$ ) using the following equation (Topp et al. 1980),

$$\sigma = \frac{\varepsilon_0 c}{L} \frac{Z_p}{Z_c} \left( \frac{2V_T}{V_R} - 1 \right) = \frac{K}{Z_c} \left( \frac{2V_T}{V_R} - 1 \right) \quad (\text{Eq. 5.6})$$

where  $K$  (1/m) is the geometric probe constant that is empirically determined by calibrating the TDR probe with solutions of known electrical conductivity. Therefore, by comparing the relative amplitudes of the reflected voltages, the electrical conductivity of materials can be obtained.

#### 5.4 MATERIALS

Natural granitic ballast was provided from a quarry in Wyoming by Burlington Northern and Santa Fe Railway (BNSF). The particle size distribution of the ballast (ASTM D6913) and the ballast specification #24 by AREMA (2002) are shown in Fig. 5.1. The particle size distribution of the as-received BNSF ballast is slightly coarser than that of the AREMA specification. The ballast has a maximum particle size of 60 mm and a minimum particle size of 25 mm. A sample of highly fouled ballast was received from Wisconsin and Southern Railroad Company in Madison, WI. The fouled ballast was sieved and separated in different particle sizes. Particles with grain size  $< 4.75$  mm were designated as 'mineral

ballast fouling', as suggested by Selig and Waters (1994). The mineral fouling has low plasticity with liquid limit of 20. A sample of coal was obtained from the Charter St. Heating and Cooling Plant in Madison. Coal was ground to produce the particle size distribution of coal fouling similar to that observed in the field (Huang et al. 2009). The coal dust sample was a non-plastic material with liquid limit of 36. Samples were prepared using BNSF ballast, mineral fouling, and coal fouling to create various fouling conditions, as shown in Fig. 5.2.

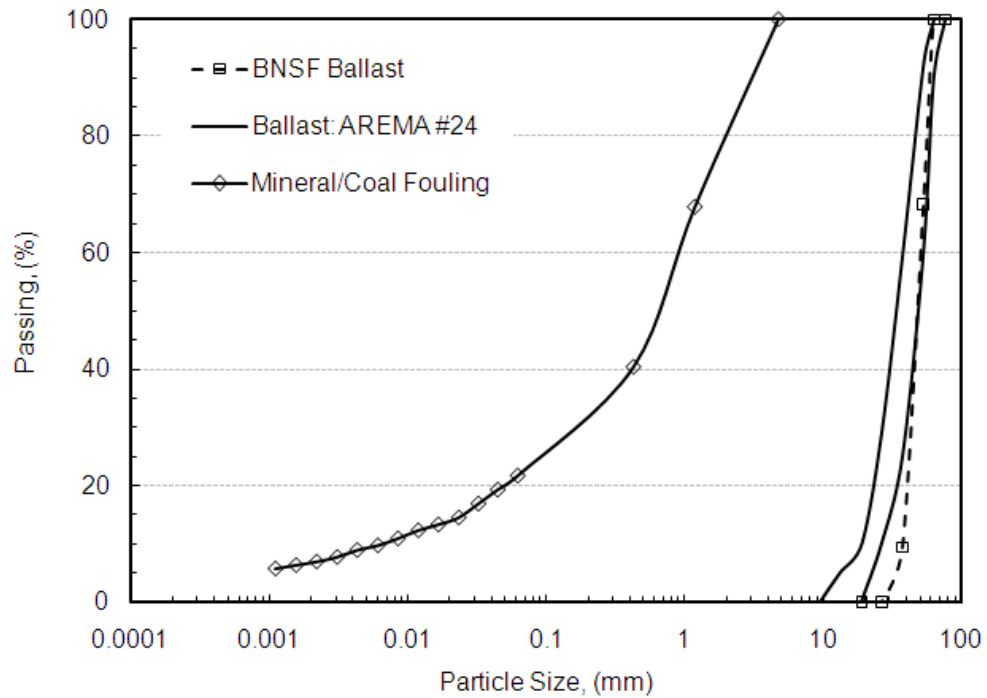


Figure 5.1 Particle Size Distribution of Ballast, Coal Dust Fouling, and Mineral Ballast Fouling

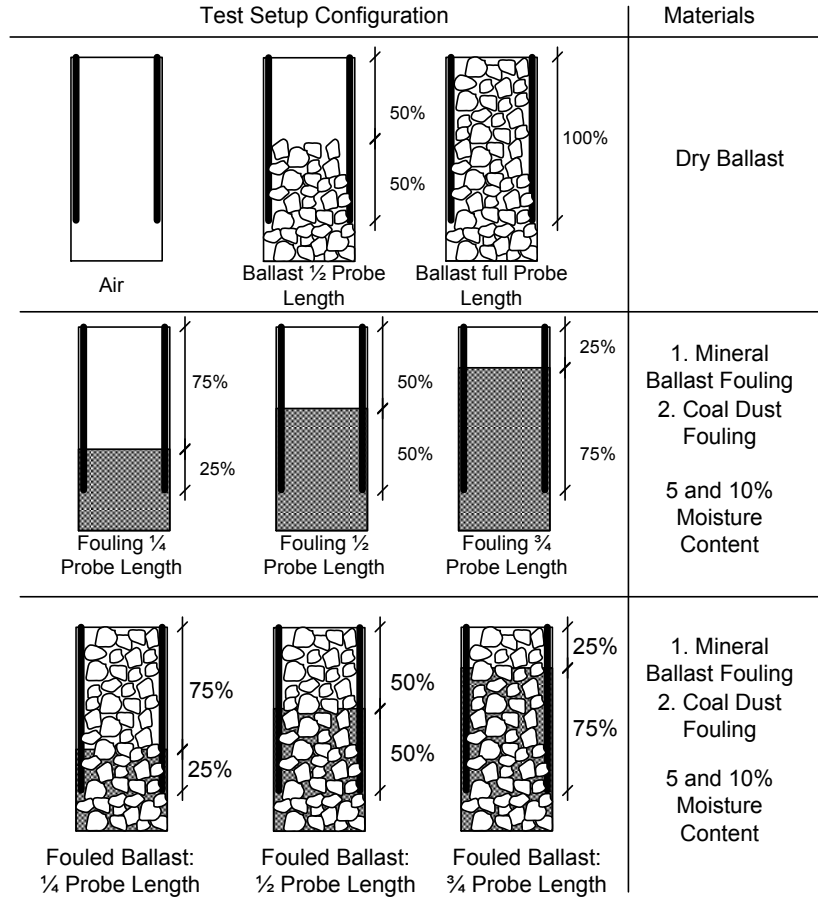


Figure 5.2 Test setups on Clean Ballast, Fouling Materials, and Fouled Ballast with various Fouling Material and Moisture Contents

## 5.5 METHODS

The TDR probes used in this study were two stainless steel rods of 5.0-mm diameter and 304-mm length. The separation between rods was 152 mm. The rods were connected to a  $Z_0=50 \Omega$  impedance coaxial cable. The cable was split to create the electrical connection to the probe legs. The coaxial cable and probe were connected to a Campbell TDR100 system (Campbell Scientific Inc. 2007), which created the fast-rise electrical step function and collected the reflected signal from the TDR probe. The TDR100 software controlled the sampling rate, number of samples, and the number of stacked signals. A sketch of the TDR probe and testing system used in this study is shown in Fig. 5.3.

A PVC cylindrical container with 152-mm diameter and 406-mm length was designed to reduce boundary effects. A two-rod probe configuration is most sensitive to materials placed between the rods and its sensitivity greatly attenuates at distances greater than two times the separation between the rods (Jones et al. 2002; Robinson et al. 2003). The probes were attached to the sides of the specimen container as a compromise to avoid difficulties in the preparation of the ballast specimens, while sensing the properties of the material outside the cell. To estimate the sensitivity of the testing system to the material outside the cell, the configuration with TDR probe separations equal to 43 and 152 mm was tested.

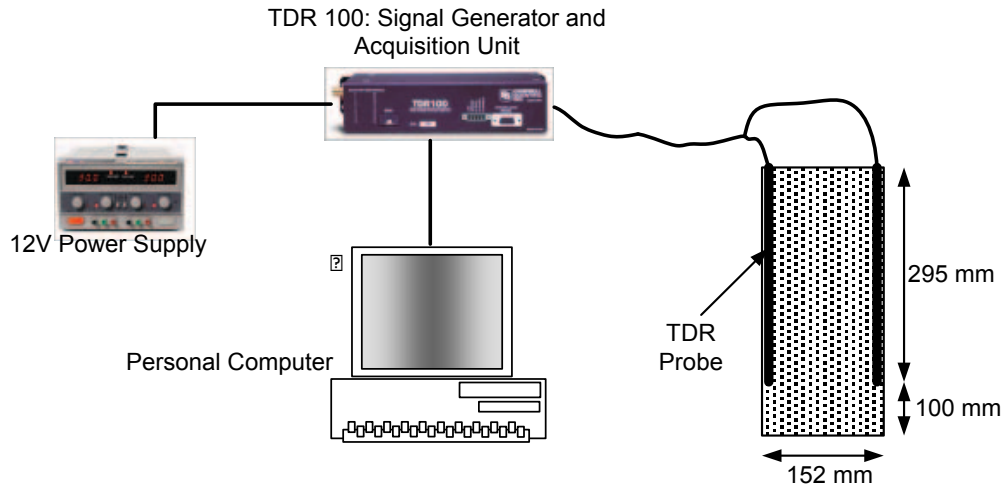


Figure 5.3 Schematic Diagram of TDR Testing Components. Note: TDR probes were attached to the wall of a polyvinyl chloride (PVC) pipe

## 5.6 RESULTS AND DISCUSSION

### 5.6.1 TDR Calibration

The EM waveforms generated in TDR with 43-mm and 152-mm probe separations are shown in Fig. 5.4. Two-way travel time for the probe separation of 152 mm is lower than the one from the 43-mm probe separation. This difference is due to the effect of electromagnetic properties of the boundary (PVC container and air) on the obtained waveforms in the DI water. The EM wave velocity obtained from TDR probes with 152-mm separation was increased with a coefficient of 1.16 to account for the EM wave propagations in the air and PVC media. The relative real dielectric permittivity was calculated using the corrected EM wave velocity in the 152-mm probe separation.

The TDR probes were calibrated on media with known EM properties, as shown in Fig. 5.5. The EM wave velocity and attenuation of various media is different due to the different relative real dielectric permittivity and electrical conductivity of media. The  $\epsilon'_r$  for air is 1, while the  $\epsilon'_r$  for de-ionized (DI) water is 80; therefore, the two-way travel time of waveform in the air is approximately one-ninth of that in the DI water. Also, the magnitude of the reflected signal gives an indication of the electrical conductivity of the material. As the electrical conductivity of media increases, the reflection coefficient of media decreases. DI water has the lowest electrical conductivity, while the electrical conductivity of media increases by increasing the concentration of NaCl salt in the water. The TDR probes were calibrated based on these results, and the geometric probe constant  $K$  (Eq. 5.6) was determined to be  $10 \text{ m}^{-1}$ .

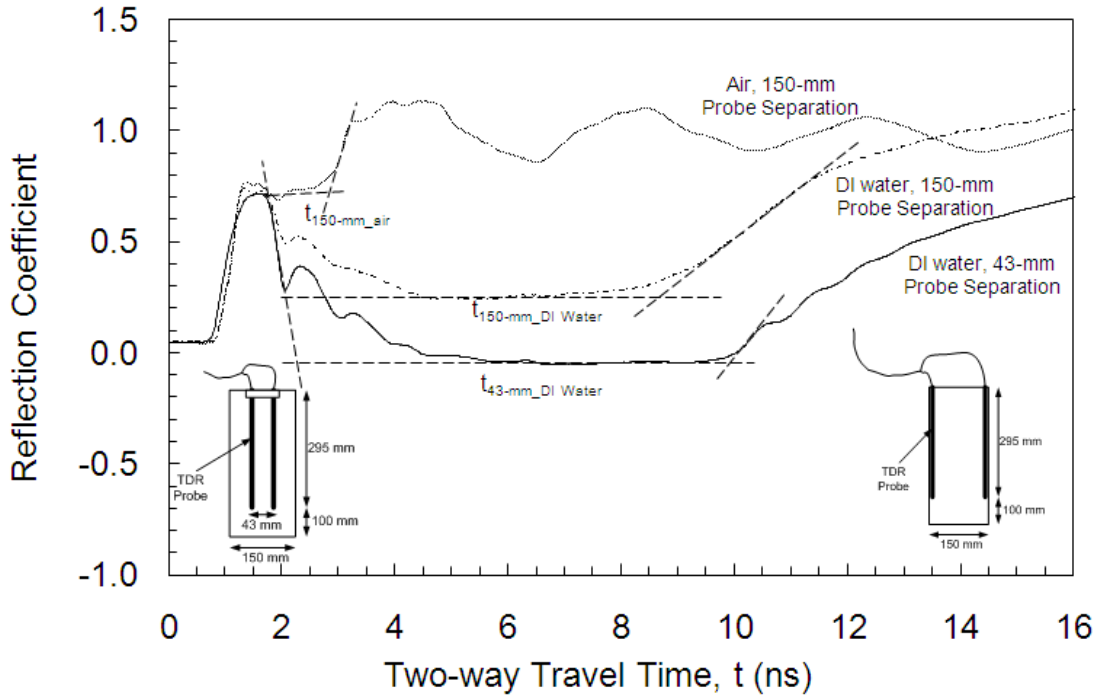


Figure 5.4 Comparison between EM Waveform Propagation in Different Probe Configurations

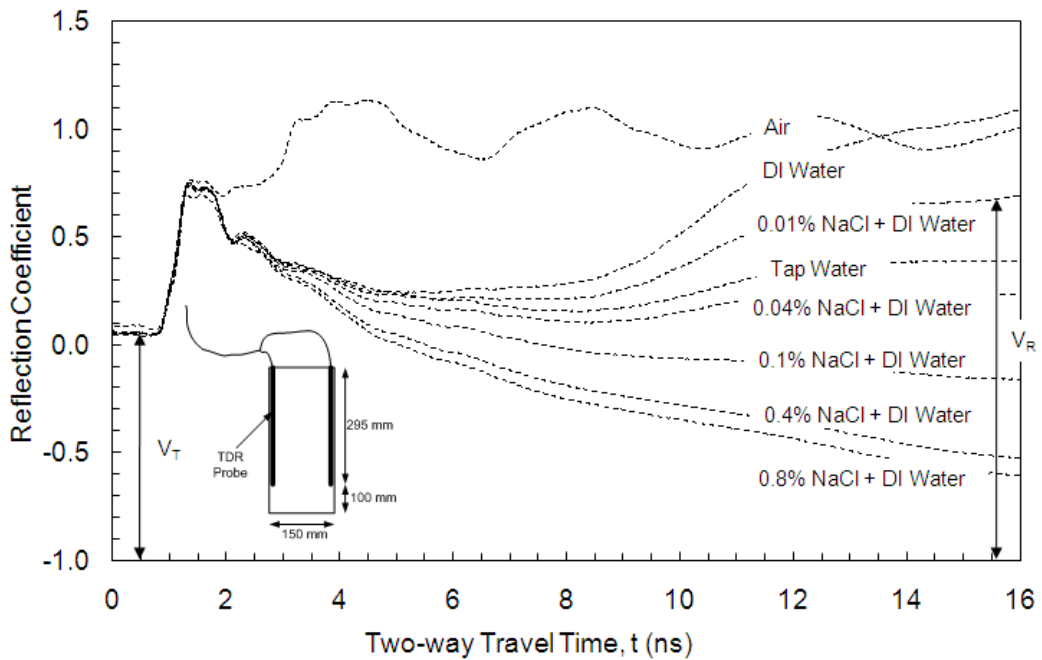


Figure 5.5 Calibration of TDR Probes in Different Testing Media

### 5.6.2 Ballast, Fouling, and Water Content

The effect of dry ballast depth on the EM-wave propagation is shown in Fig. 5.6. Increasing the length depth of ballast in the test setup increases the two-way travel time recorded from the TDR probes. This is due to the relative real dielectric permittivity ( $\epsilon'_r$ ) of geomaterials which is in the range of 4 to 10 (Lide 2007) while the relative real dielectric permittivity of air is 1. The TDR waveforms generated for varying depths of dry mineral fouling are shown in Fig. 5.7. By comparing two-way travel time of waveforms in the same depth of ballast and dry mineral fouling, the  $\epsilon'_r$  of mineral fouling is greater than that of ballast (i.e., longer two-way travel time of mineral fouling). This observation can be explained by the differences in mineralogy and porosity of the ballast particles (ballast mostly comprised of granite and rhyolite, while fouling material consisted of dolomite and quartz). Also, the relative real dielectric permittivity of a mixture of air and solids is dependent on the dielectric permittivity of each phase as well as the porosity and degree of saturation. Mixture models for relative real dielectric permittivity of soils can be used to interpret these results (Robinson et al. 2003):

$$\epsilon'_r = \sqrt[\beta]{(1-n) \cdot \epsilon'^{\beta}_{r\_ballast} + n \cdot S_r \cdot \epsilon'^{\beta}_{r\_water} + n \cdot (1-S_r) \cdot \epsilon'^{\beta}_{r\_air}} \quad (\text{Eq. 5.7})$$

where  $\epsilon'_{r\_ballast}$ ,  $\epsilon'_{r\_water}$ , and  $\epsilon'_{r\_air}$  are the relative real dielectric permittivity of the ballast (solid mineral), pore water, and pore air, respectively;  $S_r$  is the degree of saturation; and  $\beta=0.5$  is an experimentally determined parameter. For dry ballast, (i.e.,  $S_r = 0$ ), the higher local porosity means a higher volume of air ( $\epsilon'_r=1$ ) in the ballast specimen and a lower volume of ballast minerals ( $\epsilon'_r = 4$  to 10). The presence of fewer ballast particles decreases the bulk dielectric permittivity, corresponding to shorter two-way travel times in the TDR traces.

The TDR waveforms generated for varying depth of fouling for the mineral fouling in different water contents are shown in Fig. 5.8. The mineral fouling was mixed with 5 and 10% water to reproduce a range of water content of fouling material experienced in the field. By adding fouling content, four media with different electromagnetic properties contribute the waveforms generated from TDR. Ballast grains, fouling, air, and water affect the  $\epsilon'_r$  and  $\sigma$  of the fouled ballast. As shown in Fig. 5.8, two-way travel time increases with increasing depth of fouling due to the higher permittivity of fouling materials filling the ballast voids and the corresponding reduction in porosity. To evaluate the effect of fouling on the dielectric permittivity of ballast, another term (i.e., the volume of fouling) should be added to the Eq. 5.7.

Fig. 5.8 shows that an increase in water content in the fouling increases the EM wave travel time due to the higher dielectric permittivity of water in the fouled ballast voids (Eq. 5.2). The magnitude of reflected signals gives an indication of the increase of the electrical conductivity of the material (Eq. 5.6). For both mineral ballast fouling and coal dust fouling, as the fouling water content increases, the electrical conductivity of the material increases. The increase in the electrical conductivity occurs because the relative portion of higher conductivity phase (i.e., water) increases along the length of the TDR probes.

The relative real dielectric permittivity of fouled ballast with mineral fouling and coal fouling was calculated (Eq. 5.3) from the obtained data in Figs. 5.8 and 5.9. Dielectric permittivity of both fouled ballast types increases by increasing the depth of fouling from 0 to 75% of the length of TDR probes (Fig. 5.10). Increasing the dielectric permittivity of the medium reduces the EM wave velocity of fouled materials (Eq. 5.2). Electrical conductivity of fouled ballast in various depths was calculated using Eq. 5.6 and Fig. 5.8. The electrical conductivity of fouled ballast increases as the depth of moist fouling increases. This is due to the high amount of water located between the TDR probes. This change of electrical conductivity with depth of fouling appears to level off after about 50% fouling. However, more studies are required to find more comprehensive changes of electrical conductivity with the depth of fouling.

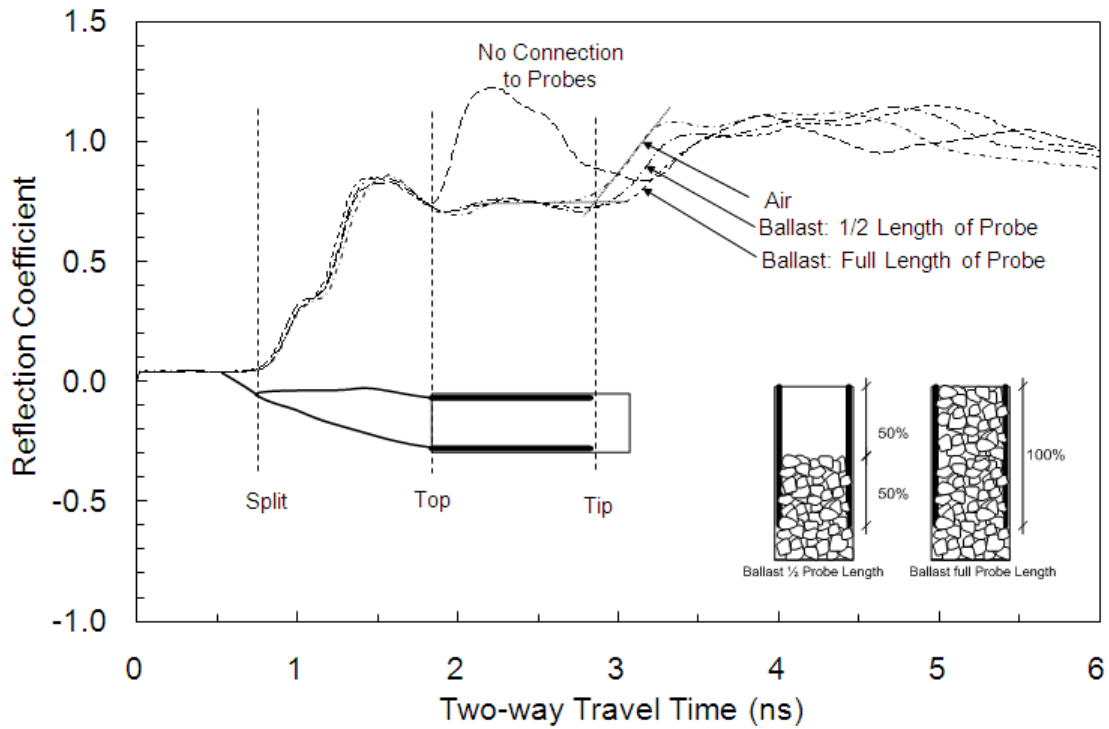


Figure 5.6 Collected TDR Data on Dry Ballast

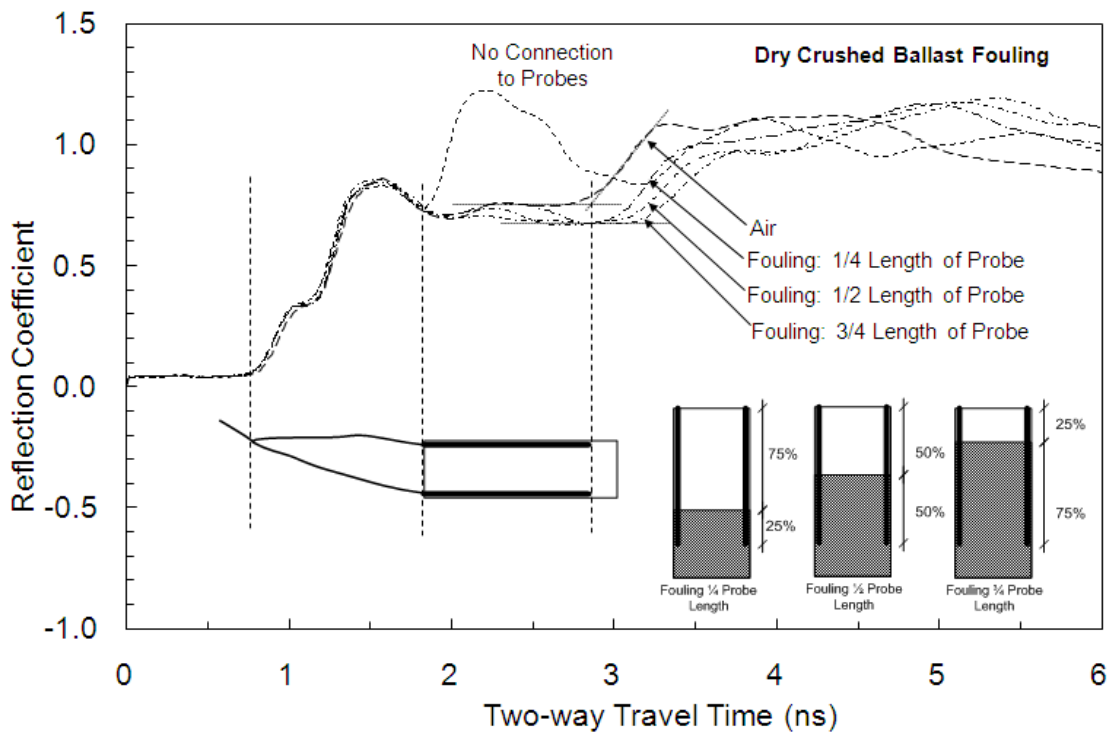


Figure 5.7 Collected TDR Data on Dry Fouled Ballast

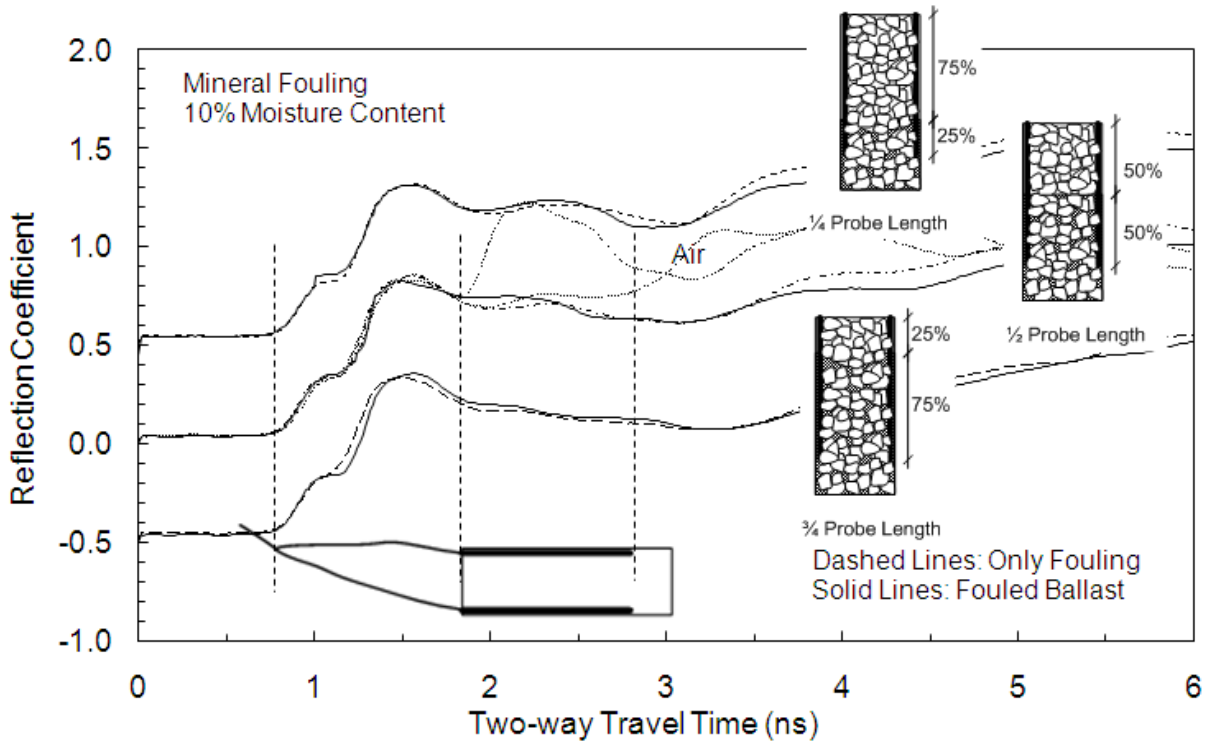
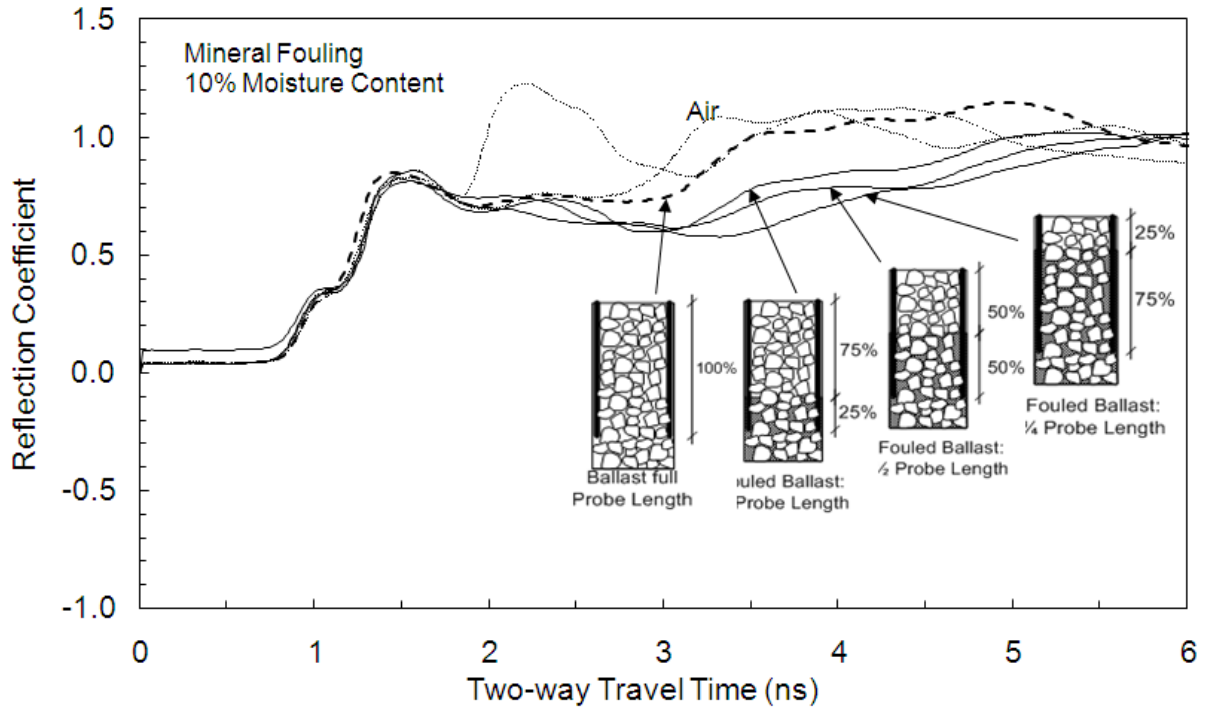


Figure 5.8 Comparison between TDR Results Collected for Test on Fouled Ballast at 5 and 10% Water Content

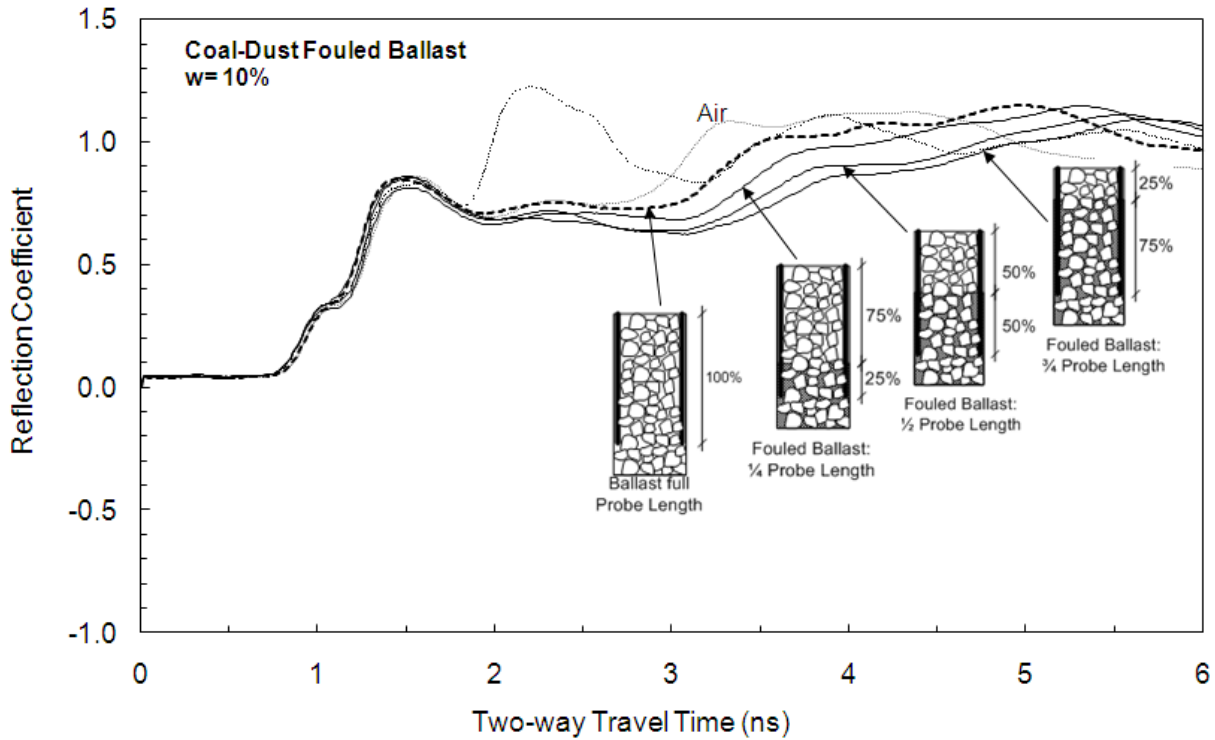


Figure 5.9 Collected TDR Data on Coal-Dust Fouled Ballast at 0 and 10% Water Content

The electrical conductivity of fouled ballast with 10% water content is about three times the one with 5% water content in the same depth of fouling.

Fig. 5.10 can be used as a qualitative approach to determine the depth of fouling material and the water content of fouled ballast as two main parameters for properly timed maintenance operations. The TDR probes can be implemented after the track construction with a proper separation for investigating the gradual change of fouling level and water content in the ballast-track. The feasibility of inserting TDR probes of proper diameter into the ballast layer after track construction should be evaluated.

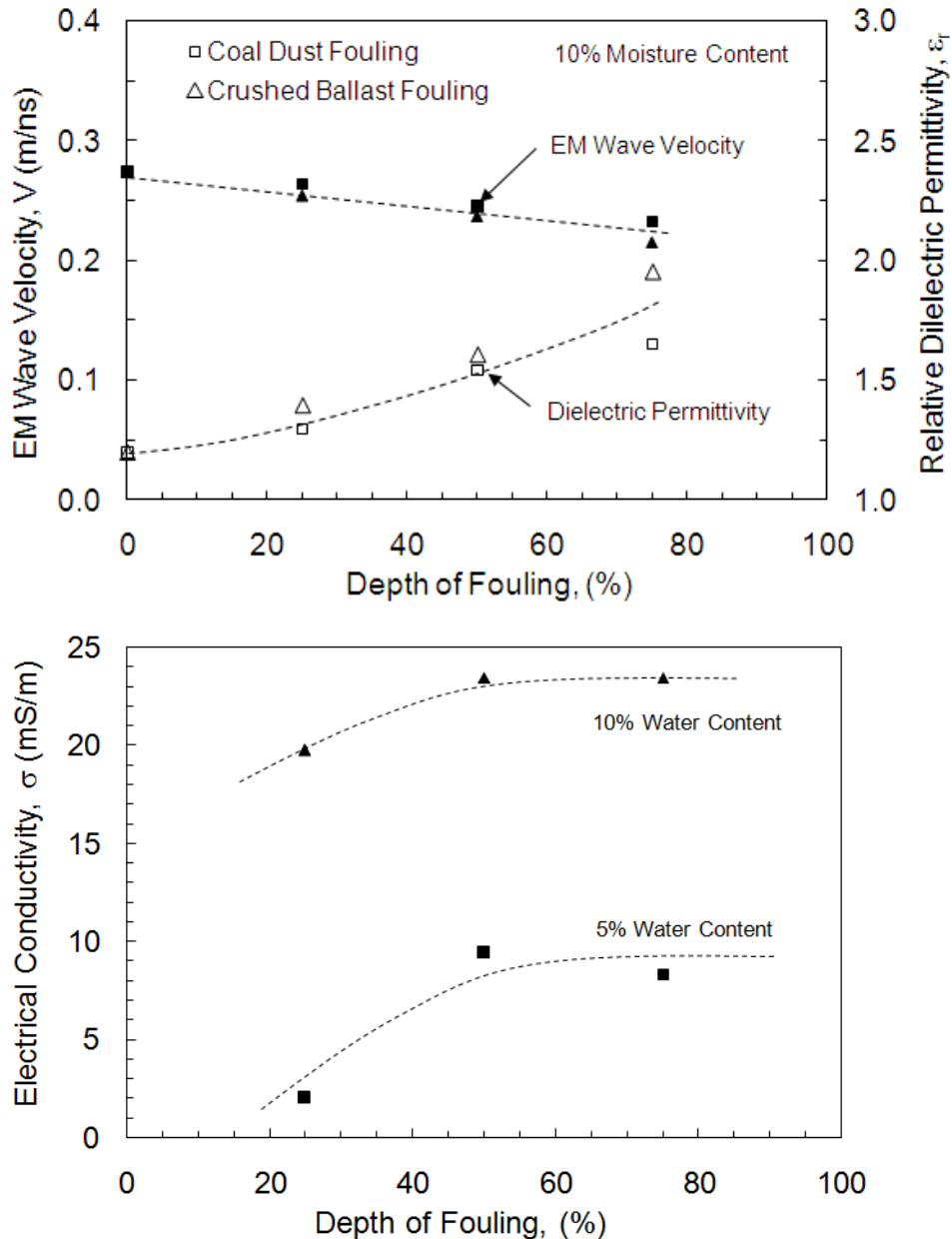


Figure 5.10 Change in Dielectric Permittivity and EM Wave Velocity of Various Fouled Ballast (a) and Electrical Conductivity of Mineral Fouling (b) for Different Depths of Fouling

### 5.7 CONCLUSIONS

Depth and moisture content of fouling were evaluated using TDR methodology. The waveforms generated from TDR probes showed that the increase in the water content and depth of fouling changes the electromagnetic properties of ballast. Increasing the fouling depth of ballast from 0 to 75% increases the relative real dielectric permittivity of fouled ballast from 1.2 to 2.0, while the EM wave velocity of media decreases from 0.27 to 0.21 m/ns. The TDR data showed that increasing the water content of fouling material increases the electrical conductivity, calculated from TDR wave forms. An increase in the water content of fouling from 5 to 10% increases the electrical conductivity of fouled ballast three times. The data obtained from the TDR shows that a qualitative method can be developed to detect the depth of fouling and water content in the ballast by evaluating the change in the electromagnetic properties of

ballast during gradual changes of fouling content, starting with clean ballast. More studies and field data are required to evaluate the practicability of TDR methodology and EM surveying methods in detecting field fouling conditions.

## **ACKNOWLEDGEMENT**

Funding for this research was provided by National Center for Freight and Infrastructure Research and Education (C-FIRE). Assistance of Andrew K. Keene for preparing the test setup and data collection, and BNSF and Wisconsin and Southern Railroad companies for providing the testing materials is appreciated. This study was conducted under the supervision of Prof. Dante Fratta.

## **REFERENCES**

- Al-Qadi, I., Xie, W., Roberts, R., 2008, Scattering analysis of ground-penetrating Radar Data to Qualify Railroad Ballast Contamination, *NDT&E Int.*, Elsevier, 41, pp.441–447
- Chrismer, S.M., Read, D.M., 1994, Examining Ballast and Subgrade Conditions, *Railway Track and Struct.*, AREMA, pp.39-42
- Clark M.R., Gillespie, R., Kemp, T., McCann, D.M., Forde, M.C., 2001, Electromagnetic Properties of Railway Ballast, *NDT&E Int.*, Elsevier, 34, pp.305–311
- Dalton F.N., Herkelrath W.N., Rawlins, D.S., Rhoades, J.D., 1984, Time Domain Reflectometry: Simultaneous Measurement of Soil Water Content and Electrical Conductivity with a Single Probe, *Science*, 224, pp.989–990.
- Darell, D.D., 2003, Substructure Can Add Life to Rail and Ties, *Railway Track and Structures*, 99(3), pp.25–27
- Descantes, Y., Fosse, Y., Milcent, F., 2006, Automated Measurement of Railway Ballast Angularity, *J. Geot. & Geoenv. Eng.*, ASCE, 18(4), pp.612–618
- Ebrahimi, A., Tinjum, J.M., Edil, T.B., 2010, Large-scale Cyclic Triaxial Testing of Rail Ballast, *Proc. AREMA 2010 Annual Conf.*, Orlando, FL, Aug 27-Sep1
- Giese K. and Tiemann, R., 1975, Determination of the Complex Permittivity from Thin-Sample Time Domain Reflectometry. Improved Analysis of the Step Response Waveform, *Advances in Molecular Relaxation Processes*, 7, pp.45-59.
- Huang, H., Tutumluer, E., Dombrow, W., 2009, Laboratory Characterization of Fouled Railroad Ballast Behavior, *88<sup>th</sup> annual Mtg. of Trans. Res. Board*, on CD-ROM
- Jack R., Jackson, P., 1998, Imagining Attributes of Railway Track Formation Using Ground Probing Radar (GPR), *Proc. Of the 1<sup>st</sup> Int. Conf. of Railway Eng.*, Eng. Technics Press, pp.20–32
- Jones, S., Wraith, J., and Or, D., 2002, Time Domain Reflectometry Measurement Principles and Applications, *Hydrological Process*, 16, pp.141-153
- Lee, H.M., 2009, Ballast Evaluation and Hot Mixed Asphalt Performance, *Proc. BCR2A Conf.*, Univ. of Illinois Urbana-Champaign, Urbana, IL, pp.1283-1289
- O'Connor, K. M. and Dowding, C. H., 1999, *Geomeasurements by Pulsing TDR Cables and Probes*, CRC Press. 412 pages.
- Raymond, G.P., 1986, Performance Assessment of a Railway Turnout Geotextile, *Can. Geotech. J.*, 23, pp.472–480
- Robinson, D., Jones, S., Wraith, J., Or, D., and Friedman, S., 2003, A Review of Advances in Dielectric and Electrical Conductivity Measurement in Soils Using Time Domain Reflectometry, *Vadose Zone Journal*, 2, pp.444-475
- Santamarina, J., in collaboration with Klein, K., and Fam, M., 2001, *Soils and Waves*, John Wiley & Sons, Chichester
- Selig, E.T., and Waters, J.M., 1994, *Track Geotechnology and Substructure Management*, Thomas Telford, NY
- Topp, G., Davis, J., and Annan, A., 1980, Electromagnetic Determination of Soil Water Content: Measurements in Coaxial Transmission Lines, *Water Resources Research*, 16(3), pp.574-582
- Zaayman, L., 2006, Ballast Cleaning, a Prerequisite for a Sustainable, Reliable, Safe and Cost Effective Railway Track, *Magazine of the South African Ins. of Civil Eng.*, 14(5), pp.20–24

## CHAPTER 6: MECHANISTIC-BASED MAINTENANCE PLANNING FROM DEFORMATION MODEL OF RAILWAY SUBSTRUCTURE

### 6.1 ABSTRACT

A railway ballast maintenance planning and scheduling tool is proposed based on incorporation of a deformation model of railway substructure. The prediction of the permanent deformation of ballast is based on (1) a mechanistic-based ballast deformation model and (2) a statistical technique termed "Support Vector Regression – SVR". Both approaches are based on data obtained using a large-scale cyclic triaxial (LSCT) apparatus. The mechanistic based deformation model introduces a correlation between the rate of plastic strain of ballast and different fouling and stress conditions. Even though rail professionals are aware of detrimental impacts of fouling on track performance, little information is available to predict and quantify this impact. In this study, the effect of fouling generation, moisture (i.e., climate), state of stress (i.e., freight load), and traffic are incorporated in a deformation model. The concept of statistical learning regression, i.e., support vector regression (SVR), was implemented to compare predictions from the statistical-based model with those from the deformation model. The results show a strong correlation ( $R^2=0.98$ ) between the predicted and calculated rate of plastic strain of ballast by SVR. The prediction from the statistical model depends significantly on large number of data to create reliable and accurate results in various track conditions. Maintenance planning and scheduling software was then developed to model surface deviation of the railway track and associated maintenance events using the mechanistic based predictive model. This software is a practical tool for determining the intervals between corrective maintenance activities (e.g., tamping) and necessity for preventive maintenance activities (e.g., undercutting or drainage systems, ...) in the railway track. The proposed method is based on large-scale laboratory tests and remains to be validated in the field.

### 6.2 INTRODUCTION

Maintenance of railway substructure is one of the main concerns facing the freight rail industry. Increasing demand for higher freight capacity (heavier loads and greater traffic volume) shortens the intervals between maintenance operations and increases costs. The frequency of railway maintenance is linked to the quality of ballast, which changes continually due to the generation of fine particles (i.e., 'fouling') and *in situ* moisture levels. Angular, uniform, large-size ballast particles play a significant role in distributing train loads to the subgrade. Ballast deteriorates with time under cyclic and heavy freight loads and deviates from its original standard specifications by generation of fines in ballast. The fouling process initiates by any of several potential fouling mechanisms including fracture and abrasion of ballast particles (i.e., 'mineral fouling'), infiltration from underlying layers (e.g., clay fouling), and spillage from surface sources (e.g., coal fouling) (Selig and Waters 1994; Darell 2003; Su et al. 2010, Huang et al. 2009). Fouling leads to an accumulation of permanent deformation in the track, thus resulting in increased surface deviation. Increasingly heavier freight loads in the US will likely increase the surface deviation of railway track and related maintenance costs (Lee 2009). Larsson and Gunnarsson (2001) stated that a 20% increase in axle load results in 24% extra maintenance cost. The maintenance operation for ballast tamping and surface alignment costs about \$500M annually for the 150,000 kilometers of Class1 track in the US (\$3,800/km/yr, Christmer and Davis 2000).

Efficient maintenance of railway substructure is essential to provide a continuous service at a reasonable cost. Maintenance decisions within the railway industry depend on available information from inspections, standards, and individual and institutional experience (Andersson 2002). Typically, inspection techniques tend to detect the rate of track deterioration. Within the rail industry, there are limited standard procedures or protocol to schedule preventive maintenance activities or, and possibly more importantly, to evaluate their potential effects (Andersson 2002).

There are two approaches used to develop a maintenance planning program for rail track, one is performance-based and the other mechanistic-based. Significant historical data (e.g., traffic, maintenance activities, substructures, and climate data) are required in the performance-based approach to create a comprehensive maintenance model. However, sufficient historical data are unlikely to be archived or accessible in many cases (Andersson 2002; Stirling et al. 1999). The key aspect of a mechanistic model is to integrate the performance of various components of the railway track as developed on the basis of mechanistic principles. Use of a mechanistic model can explain and predict the rate of track deterioration in various conditions and decreases the uncertainties of deterioration during

the service life of track. A comprehensive track deterioration model should combine both performance and mechanistic models to determine the track quality (Fazio and Prybella 1980; Zarembski 1998). A ballast deterioration model was proposed by Chrismer and Selig (1994) to predict ballast-related maintenance timing and costs based on field data; however, the effect of fouling condition, moisture content, and state of stress on the deformation of ballast and rail track was not included in Chrismer's study.

The objective of this study was to develop a deformation model for railway ballast to account for various fouling conditions, moisture (i.e., climate), traffic, freight capacity (i.e., level of stress), and material quality (e.g., rate of fouling generation). A statistical model for fouled ballast deformation is developed based on the concept of support vector regression (SVR) to compare with deformation model and evaluate the effectiveness and limits of each method. A maintenance planning and scheduling software incorporates the deformation model of track substructure to predict surface deviation of the railway track. This software is a tool for determining the intervals between corrective maintenance activities (e.g., tamping) and necessity for preventive maintenance activities (e.g., undercutting or drainage systems, ...) in the railway track.

## 6.3 BACKGROUND

### 6.3.1 Fouling Indices

Selig and Waters (1994) define a fouling content (FC) that has been widely used in the US as  $FC = P_4 + P_{200}$ ,  $P_4$  fraction is % mass < 4.75 mm, and  $P_{200}$  fraction is % mass < 0.075 mm. In Chapter 4, the affected contact points of ballast were shown to control plastic deformation of railway ballast under traffic loading; therefore, the volume of voids that have been filled by fouling defines the state of fouling. The volumetric fouling index (FI) has been proposed to equate the level of fouling in ballast due to different fouling materials with varying specific gravities as:

$$FI = FC \frac{G_{so}}{G_s} \quad (\text{Eq. 6.1})$$

where  $G_{so}$  is the reference specific gravity (= 2.6 as chosen from mineral fouling) and  $G_s$  is the specific gravity of each fouling material (2.6 for mineral fouling and 1.3 for coal fouling).

### 6.3.2 Maintenance Planning Model for Railway Ballast

The framework of track maintenance planning for railway track is shown in Fig. 6.1. The main parts of this model are track inspection, a track deterioration model, and standards for maintenance planning. This concept can be adopted for railway ballast. Prior to using the maintenance model, ballast quality is determined by inspection techniques, such as those detailed in Chapter 5. From the deterioration model (or deformation model), the surface deviation of the track due to the subgrade and ballast deformation can be predicted. Maintenance criteria are assigned with respect to rail class (i.e., passenger or freight rail and operating speed) to estimate the timing for corrective (e.g., tamping) or preventive (e.g., ballast cleaning) maintenance activities.

## 6.4 STATISTICAL APPROACH

### 6.4.1 Support Vector Regression for Geotechnical Applications

Support vector machines (SVMs) are valuable tools for data classification. Application of SVMs in geotechnical engineering is an emerging area. Dibike et al. (2001), Maalouf et al. (2010) and Pal (2006) used the SVM for infrastructure applications. Dibike et al. (2001) used SVMs in rainfall and run-off problems. Maalouf (2008) used this method to predict asphalt mix performance for highways. Pal (2006) examined the potential of SVMs for assessing liquefaction potential from field data.

Support vector machines are based on statistical learning theory as proposed by Vapnik (1995) to find an optimal hyper-plane as a decision function in high dimensional space. SVM produces a model based on the training data and predicts the target values of the test data (given data attributes or independent variables). In statistical learning theory (Vapnik 1995), the problem of learning an input-output relationship from a data set is generally viewed as the problem of choosing from the given set of

functions  $f(\mathbf{x}, \alpha)$ ,  $\alpha$  is scalar and  $\alpha \in \mathbb{R}$ , where  $\mathbf{x} \in \mathbb{R}^n$  is the vector of independent variable (e.g., fouling index, water content, stress, ...) with fixed but unknown probability distribution function  $P(\mathbf{x})$ .

The conditional distribution function  $P(y|\mathbf{x})$  that best approximates the output value  $y$  (e.g., plastic strain of ballast) to every input vector  $\mathbf{x}$  is fixed but unknown. The selection of the desired  $P$  and  $f$  function is based on a training set of independent and identically distributed observations  $(x_1, y_1), \dots, (x_l, y_l)$  according to  $P(\mathbf{x}, y) = P(\mathbf{x}) P(y|\mathbf{x})$ . The expected loss (or discrepancy) due to classification or estimation errors, is given by the risk function

$$R(\alpha) = \int L(y, f(\mathbf{x}, \alpha)) dP(\mathbf{x}, y) \quad (\text{Eq. 6.2})$$

where  $L(y, f(\mathbf{x}, \alpha))$  is the discrepancy between the measured  $y$  and the predicted  $f(\mathbf{x}, \alpha)$  by the SVM. The goal is to find the function  $f(\mathbf{x}, \alpha)$  that minimizes this risk function,  $R(\alpha)$ , where the only available information is the training set (e.g., plastic strain of ballast obtained from experiments). The risk function is unknown since  $P(\mathbf{x}, y)$  is unknown; therefore, a risk minimization is necessary. One method is called the empirical risk minimization (ERM) inductive principle. This straightforward approach is to minimize the empirical risk:

$$R_{\text{emp}}(\alpha) = \frac{1}{l} \sum_{i=1}^l \frac{1}{2} |f_{\alpha}(x_i) - y_i| \quad (\text{Eq. 6.3})$$

To minimize the actual risk of the model with a limited number of training samples (e.g., limited measured data), Vanpik (1995) developed a statistical technique that incorporated structural risk minimization. Details of this solution are presented in Vanpik (1995).

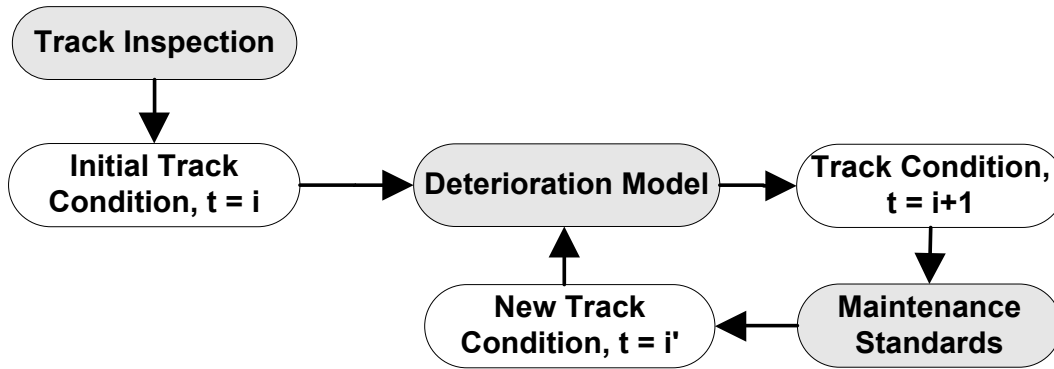


Figure 6.1 Different Components of Railway Maintenance Planning

### 6.4.2 Support Vector Regression

Support vector machines can be applied to regression problems by the introduction of an alternative loss function that is modified to include a distance measure (Smola and Scholkopf 2004). Let the observed variable  $y$  (e.g., plastic strain of ballast) have real value, and let  $f(\mathbf{x}, \alpha)$ ,  $\alpha \in \mathbb{R}$ , be a set of real functions that contains the regression function  $f(\mathbf{x}, \alpha_0)$ . Given a training set of instance label pairs  $(x_i, y_i)$ ,  $i = 1, 2, 3, \dots, l$ , where  $x_i \in \mathbb{R}^n$  and  $y_i \in \mathbb{R}$  with a linear function,  $f(\mathbf{x}, \alpha) = (\mathbf{w} \cdot \mathbf{x}) + b$ . The training pattern is linearly separable if there exists a vector  $\mathbf{w}$  and a scalar  $b$ . The optimal function is given by minimizing the empirical risk

$$R_{\text{emp}}(\mathbf{w}, b) = \frac{1}{l} \sum_{i=1}^l |f_{\alpha}(x_i, \alpha) - y_i| \quad (\text{Eq. 6.4})$$

with the most general loss function with an  $\varepsilon$ -insensitive zone described as

$$\begin{aligned} |f(\mathbf{x}, \alpha) - y|_{\varepsilon} &= \varepsilon & \text{if } |f(\mathbf{x}, \alpha) - y| \leq \varepsilon; \\ |f(\mathbf{x}, \alpha) - y|_{\varepsilon} &= |f(\mathbf{x}, \alpha) - y| & \text{otherwise} \end{aligned} \quad (\text{Eq. 6.5})$$

The objective is now to find a function  $f(x, \alpha)$  that has at most a deviation of  $\epsilon$  from the actual observed targets  $y_i$  for all the training data and, at the same time, is as flat as possible. This is equivalent to minimizing the functional

$$\Phi(w, \xi^*, \xi) = \|w\|^2 / 2 + C (\sum \xi^* + \sum \xi) \quad (\text{Eq. 6.6})$$

where  $C$  is a pre-specified value; and  $\xi^*$ ,  $\xi$  are positive slack variables representing upper and lower constraints on the outputs of the system (Fig. 6.2). Using a Lagrange function (Vanpik 1995), the partial derivatives of this function with respect to the primary variables ( $w$ ,  $\xi$ ,  $\xi^*$ ) have to vanish for optimality (i.e., the saddle point condition). The desired vectors can be found as:

$$w_0 = \sum_{\text{support Vector}} (\alpha_i^* - \alpha_i) x_i \quad (\text{Eq. 6.7})$$

where  $0 \leq \alpha_i^*$  and  $\alpha_i \leq C$  and therefore:

$$f(x) = \sum_{\text{support Vector}} (\alpha_i^* - \alpha_i) (x_i \cdot x) + b_0 \quad (\text{Eq. 6.8})$$

When linear regression is not appropriate, as in the case of many engineering applications, a nonlinear mapping kernel  $K$  is used to map the data into a higher-dimensional feature space. In this model, the kernel  $K$  function replaces the dot operation between  $x$  in Eq. 6.8. The kernel function is defined as

$K(x_i, x_j) = \exp(-\gamma \|x_i - x_j\|^2)$  that creates a reasonable mapping function for typical engineering data.  $\gamma$  is a multiplier in the Kernel function.

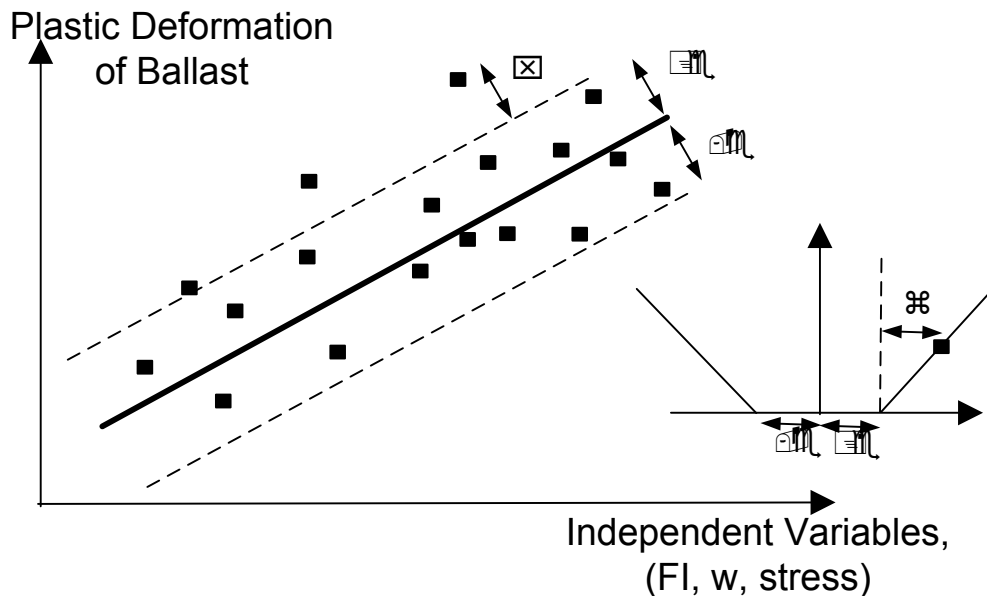


Figure 6.2 Pre-specified Accuracy  $\epsilon$  and Slack Variable ( $\zeta$ ) in Support Vector Regression (after Scholkopf 1997)

## 6.5 MATERIALS AND METHODS

The ballast deformation model was based on experiments performed on a granitic ballast sample that was provided from a quarry in Wyoming by BNSF Rail Company. Particle size of the ballast was 25 to 63 mm. Different sources of fouling were tested in this study, including fouling from subballast intrusion or ballast breakage (i.e., mineral fouling) and surface spillage (i.e., coal fouling). The mineral and coal fouling were non-plastic. Specific gravity of coal fouling was 1.3 and that of mineral fouling was 2.6. The details of tested materials are given in Chapter 4.

A prototype large-scale cyclic triaxial (LSCT) apparatus was developed to test a specimen with 305-mm diameter and 610-mm length. Plastic deformation of ballast in various fouling, moisture, and stress condition was determined over  $2 \times 10^5$  traffic cycles. The ballast specimens were tested at a reference stress state consisting of a confining stress ( $\sigma_{3,ref}$ ) of 90 kPa and a cyclic stress ( $\sigma_{d,ref}$ ) of 300 kPa to study the effect of fouling conditions. The method of determining the representative state of stress for ballast is described in Chapter 3. The ballast specimens were also tested in various states of stress to determine the deformational behavior of ballast under heavier freight loads. Ballast specimens were prepared by compaction to the maximum dry unit weight of ballast  $\gamma_d = 15.8 \pm 0.3 \text{ kN/m}^3$ . Again, additional details on specimen preparation are given in Chapter 3.

## 6.6 SUMMARY BEHAVIOR OF FOULED BALLAST

Plastic strain ( $\epsilon_p$ ) of fouled ballast was measured as a function of loading cycles (N) for a wide range of FI and water contents (w). The rate of  $\epsilon_p$  in semi-log scale,  $r_p$ , was calculated. The number of load repetitions (N) was also converted into million gross tones for rail cars with axle load of 264 kN (30 tones) ( $\text{MGT} = \frac{N \times 30}{10^6}$ ), a widely used terminology among rail professionals. As presented in Chapter 4, mineral and coal fouling materials were called ‘non-cohesive fouling’ and have similar deformational behavior. The  $\epsilon_p$  of ballast increases linearly up to  $N=10^4$  (0.3 MGT) in a semi-log scale as shown in Fig. 6.3. This part of the deformation model is called the ‘initial compaction phase (ICP)’. The  $r_p$  of ballast is fairly constant in the ICP. When the ICP is passed, an increase in  $\epsilon_p$  is pronounced and the  $r_p$  increases linearly. This part of the deformational behavior of ballast is called the ‘fouling impact phase (FIP)’. Therefore, a deformation model was proposed as shown in Fig. 6.3b to account for ICP and FIP parts of the plastic strain of fouled ballast. Parameters ‘a’ and ‘b’ in Fig. 6.3b represent the ICP and FIP in the deformation model of ballast.

## 6.7 DEFORMATION MODEL OF RAILWAY BALLAST

Ballast is typically placed in a railway track in a clean or slightly fouled condition. However, generation of fouling continues during the service life of the track. To predict the deformation of ballast during the service life of rail track, three steps are taken: (1) the deformation model for railway ballast in a certain fouling condition (water content and FI) is characterized, (2) the deformation model for ballast at different states of stress is determined, and (3) an incremental analysis (integrating the change of fouling, water content, and traffic loading during the service life of a track) is performed.

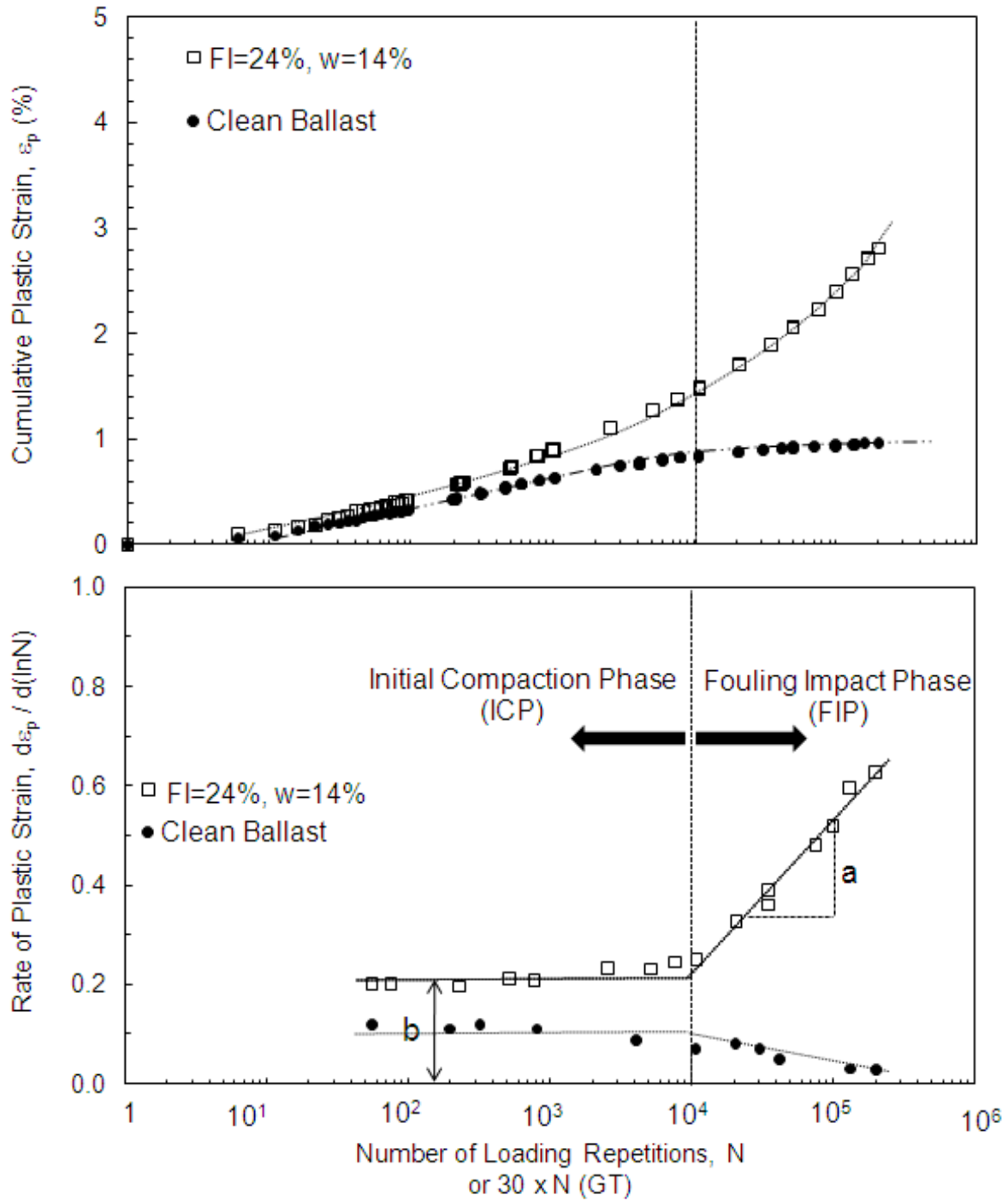


Figure 6.3 Deformation Model for Railway Ballast Presented by Deformation of Clean ballast and Fouled Ballast with FI=24% and w=14%

### 6.7.1 Effect of Fouling and Water Content on the Deformation Model

The deformation model of ballast at given FI and w at the reference confining stress ( $\sigma_{3ref}$ ) of 90 kPa and cyclic stress ( $\sigma_{dref}$ ) of 300 kPa was determined. Change in the FI during the LSCT tests is assumed negligible (less than 0.5%). This assumption is in good agreement with the typical rate of fouling

generation in ballast of about 0.1%/MGT (Selig and Waters 1994). As shown in Fig. 6.3b, the rate of plastic strain ( $r_p$ ) of ballast is defined:

$$r_p = \frac{d\varepsilon_p}{d\ln N} = b \quad N < 10^4 \text{ (0.3 MGT)} \quad (\text{Eq. 6.9a})$$

$$r_p = \frac{d\varepsilon_p}{d\ln N} = b + a \log(N - 10^4) \quad N > 10^4 \quad (\text{Eq. 6.9b})$$

The effect of fouling and moisture on parameters 'a' and 'b' at the representative state of stress is shown in Fig. 6.4. The parameters  $a_{\text{ref}}$  and  $b_{\text{ref}}$  can be defined as:

$$a_{\text{ref}} = R_a \text{FI}(w - 3) \quad (w > 3\%) \quad R^2=0.91 \quad (\text{Eq. 6.10a})$$

$$b_{\text{ref}} = R_b \text{FI}(w - 3) + b_o \quad (w > 3\%) \quad R^2=0.87 \quad (\text{Eq. 6.10b})$$

where FI is the fouling index and w is the water content of fouling materials. When  $w \leq 3\%$ , the  $r_p$  of ballast is constant ( $b_o = 0.08$ ) and  $r_p$  diminishes toward zero (Fig. 6.3) at FIP.  $R_a$  is 0.0012 and  $R_b$  is 0.0005 for fresh ballast conditions.  $R_a$  and  $R_b$  may change for different types of ballast (recycled or clean ballast) and fouling materials. Increasing FI and w accelerates the  $r_p$  of ballast both in ICP and FIP, with corresponding parameters 'a' and 'b'. At a given water content, the  $r_p$  of ballast in the ICP (i.e., parameter a) increases 2.5 times more than the  $r_p$  of ballast in the FIP (compare  $R_b$ ). The parameters a and b increase relatively linearly with FI and w for the series of tests on fouled railway ballast.

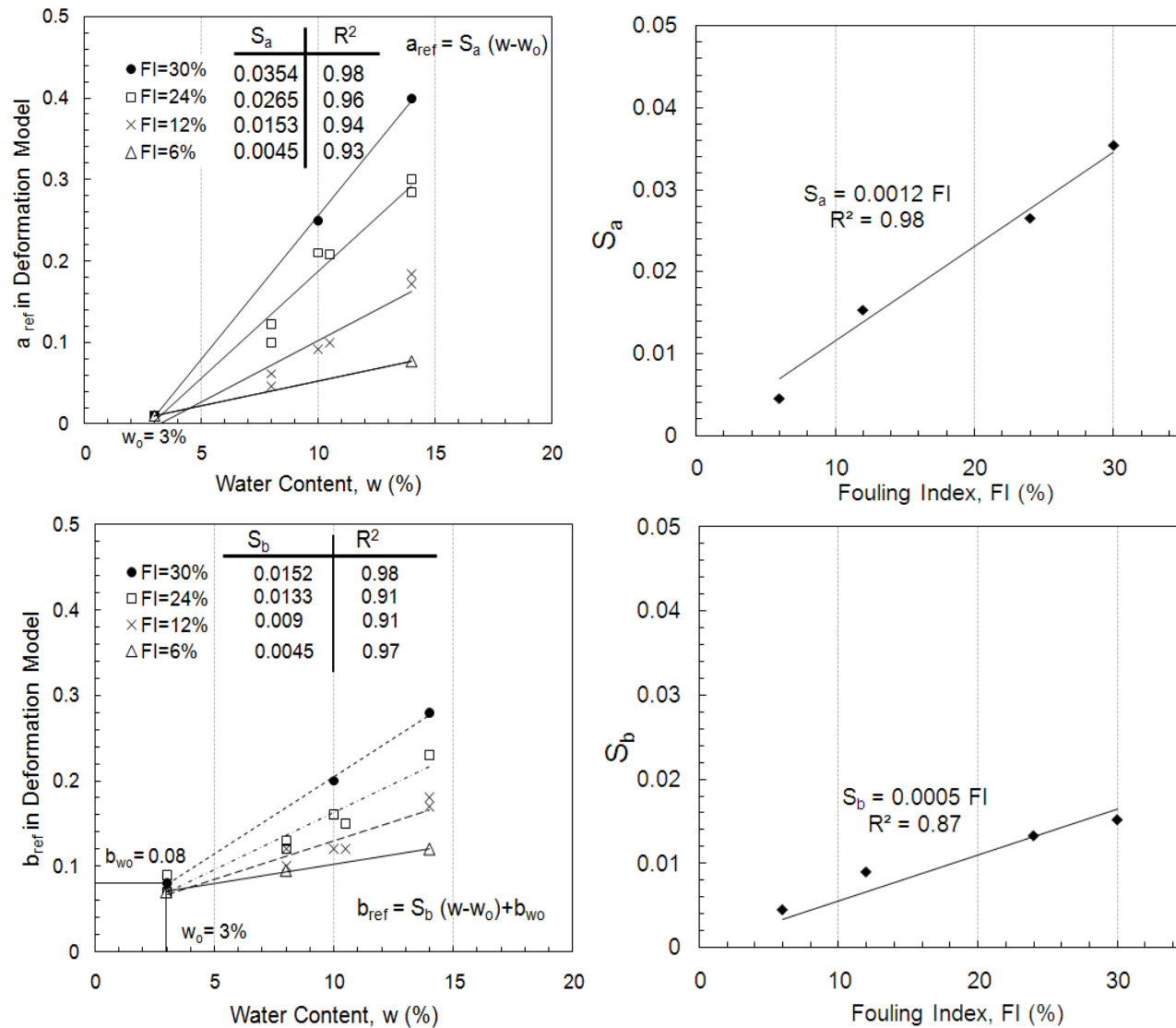


Figure 6.4 Parameters 'a' and 'b' in Deformation Model of Railway Ballast as a Function of FI and w

### 6.7.2 Effect of State of Stress on Deformational Behavior of Ballast

To include the state of stress in the deformation model of railway ballast, parameters 'a' and 'b' at various states of stress were determined relative to those with the reference state of stress (i.e.,  $a_{ref}$  and  $b_{ref}$ ). The ratio of principal stresses ( $\sigma_1 / \sigma_3$ ) is used to determine the deformational behavior of ballast in various states of stress, where  $\sigma_1 = \sigma_d + \sigma_3$ . The reference confining stress ( $\sigma_{3\ ref}$ ) of 90 kPa and cyclic stress ( $\sigma_{d\ ref}$ ) of 300 kPa results in  $\sigma_1 / \sigma_3 = 4.3$ . The range of  $\sigma_1 / \sigma_3$  from 3 to 10 was considered in the series of LSCT tests to account for the range of stresses that ballast can experience in railway track. The range of stresses was derived from the finite element analysis in Chapter 3.

The parameters of the deformation model (i.e., 'a' and 'b') at various states of stress are summarized in Table. 6.1. The normalized parameters  $\frac{a}{a_{ref}}$  and  $\frac{b}{b_{ref}}$  are shown in Fig. 6.5 as a function of  $\sigma_1 / \sigma_3$  and expressed as:

$$\frac{a}{a_{ref}} = 0.20 \left( \frac{\sigma_1}{\sigma_3} \right) \quad R^2=0.94 \quad (\text{Eq. 6.11a})$$

$$\frac{b}{b_{ref}} = 0.26 \left( \frac{\sigma_1}{\sigma_3} \right) - 0.26 \quad R^2=0.95 \quad (\text{Eq. 6.11b})$$

Parameter a increases linearly by a factor of 0.20 and b increases linearly by a factor of 0.26 with ratio of principal stresses. The  $r_p$  in initial compaction phase (i.e., parameter b) approaches zero when  $\sigma_1 / \sigma_3$  reaches to 1; i.e., isotropic stress condition for the ballast.

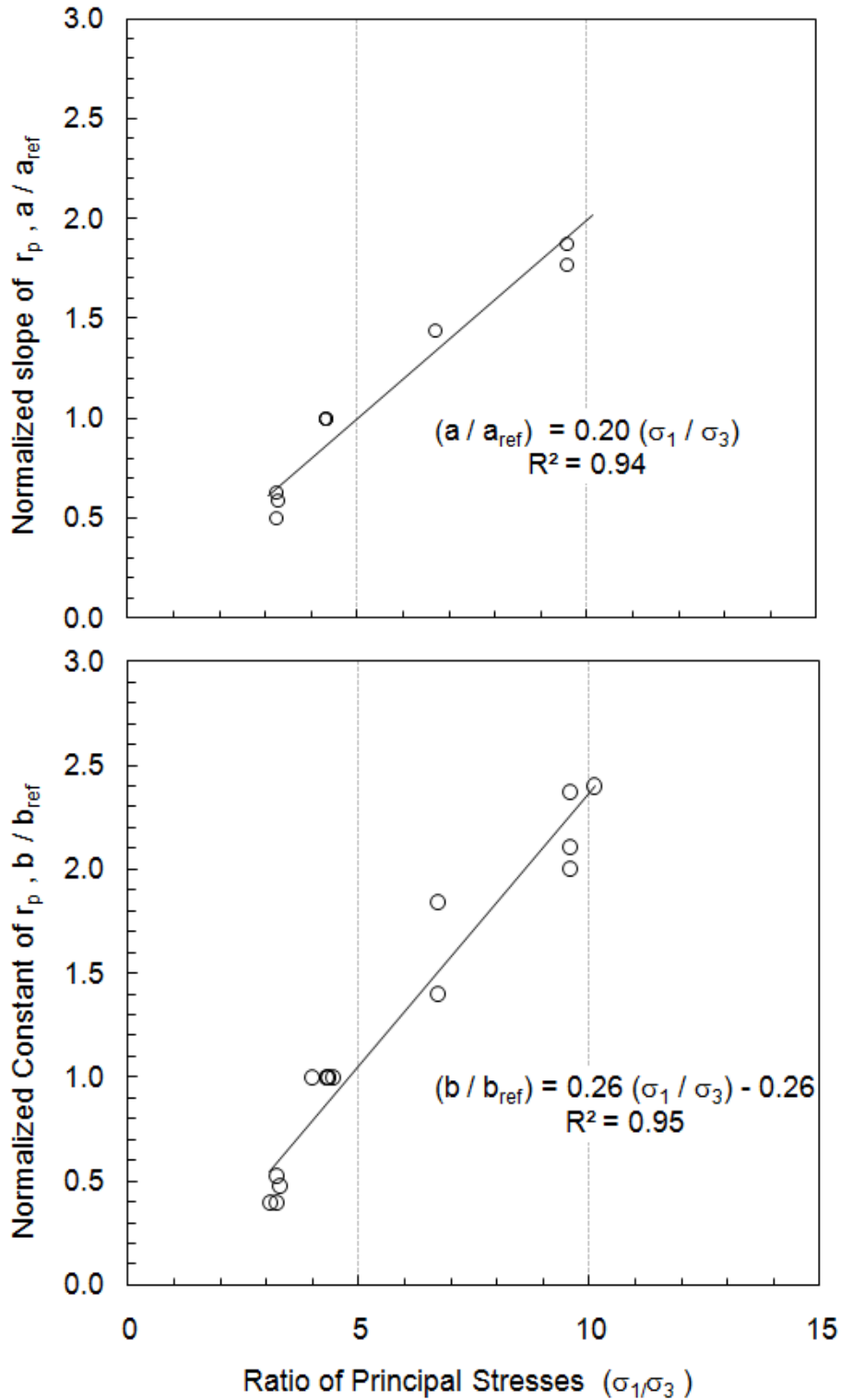


Figure 6.5 Normalized Deformation Parameters (i.e., a and b) of Railway Ballast as a Function of Principal Stress Ratios

Table 6.1 Deformation Model Parameters for Railway Ballast in Various Fouling Conditions

FI	w	$\sigma_3$	$\sigma_d$	b	a	$\frac{\sigma_1}{\sigma_3}$	$\frac{b}{b_{ref}}$	$\frac{a}{a_{ref}}$
20	13	35	300	0.45	0.3	9.5	2.36	1.875
		35	200	0.35	0.23	6.7	1.84	1.43
		<b>90</b>	<b>300</b>	<b>0.19</b>	<b>0.16</b>	<b>4.3</b>	<b>1</b>	<b>1</b>
		90	200	0.1	0.1	3.2	0.52	0.62
	8	90	200	0.1	0.01	3.2	0.52	0.5
		<b>90</b>	<b>300</b>	<b>0.19</b>	<b>0.02</b>	<b>4.3</b>	<b>1</b>	<b>1</b>
		35	300	0.4	0.05	9.5	2.10	2.5
	3	90	200	0.02	-0.0315	3.2	0.4	-*
		35	200	0.07	0.1346	6.7	1.4	-
		<b>90</b>	<b>300</b>	<b>0.05</b>	<b>-0.003</b>	<b>4.3</b>	<b>1</b>	<b>1</b>
10	12	35	201	0.2	0.22	6.7	0.5	1.29
		90	205	0.12	0.1	3.27	0.48	0.59
		<b>92</b>	<b>304</b>	<b>0.25</b>	<b>0.17</b>	<b>4.3</b>	<b>1</b>	<b>1</b>
		35	300	0.5	0.33	9.5	2	1.94
0	0	33	301	0.12	-0.05	10.1	2.4	-
		<b>88</b>	<b>303</b>	<b>0.05</b>	<b>0</b>	<b>4.4</b>	<b>1</b>	<b>1</b>
		96	198	0.02	0	3.1	0.4	-

\* The rate of plastic deformation decreases (i.e., fouling impact phase (FIP) was not observed) at water w < 3%.

### 6.7.3 Incremental Analysis by Integrating Change of Fouling, Moisture, and State of Stress

The continual change of fouling content (i.e., generation of fouling), moisture (i.e., effect of climate), and stress (freight load or higher speed) should be incorporated into the deformation model of railway ballast to determine the surface deviation of a track during traffic loading. To account for incremental changes in fouling, moisture, and stress, the  $\varepsilon_p$  of ballast should be calculated in increments of traffic (i.e.,  $\delta N$  or  $\delta MGT$ ). Fig. 6.6 demonstrates how change of fouling, water content, and state of stress is captured in an integrated deformation model for railway ballast. Based on this approach, FI is determined from the rate of fouling generation, while moisture and state of stress are from the climate data and traffic loading. Accumulation of  $\varepsilon_p$  of ballast ( $\delta\varepsilon_{pi}$ ) in a period of  $N_i$  to  $N_{i+1}$  traffic loading is calculated by integrating the  $r_p$  of ballast:

$$\delta\varepsilon_{pi} = \int_{N_i}^{N_{i+1}} \frac{d\varepsilon_p}{d(\ln N)} d(\ln N) \quad (\text{Eq. 6.12})$$

where  $N_i$  is the  $i^{\text{th}}$  increment of integration for the plastic strain. Accumulation of  $\varepsilon_p$  of ballast in different fouling conditions is calculated by summing the  $\delta\varepsilon_{pi}$  in increments of traffic, as:

$$\varepsilon_p(N) = \sum_{i=1}^N \left( \int_{N_i}^{N_{i+1}} \left( \frac{d\varepsilon_p}{d(\ln N)} \right)_i d(\ln N) \right) \quad (\text{Eq. 6.13})$$

In Eq. 6.13, the  $r_p$  of ballast  $\left( \frac{d\varepsilon_p}{d(\ln N)} \right)_i$  in  $i^{\text{th}}$  increment of traffic is a function of fouling, moisture, and level of stress at the beginning of that increment and is determined from the developed deformation model of railway ballast in this study.

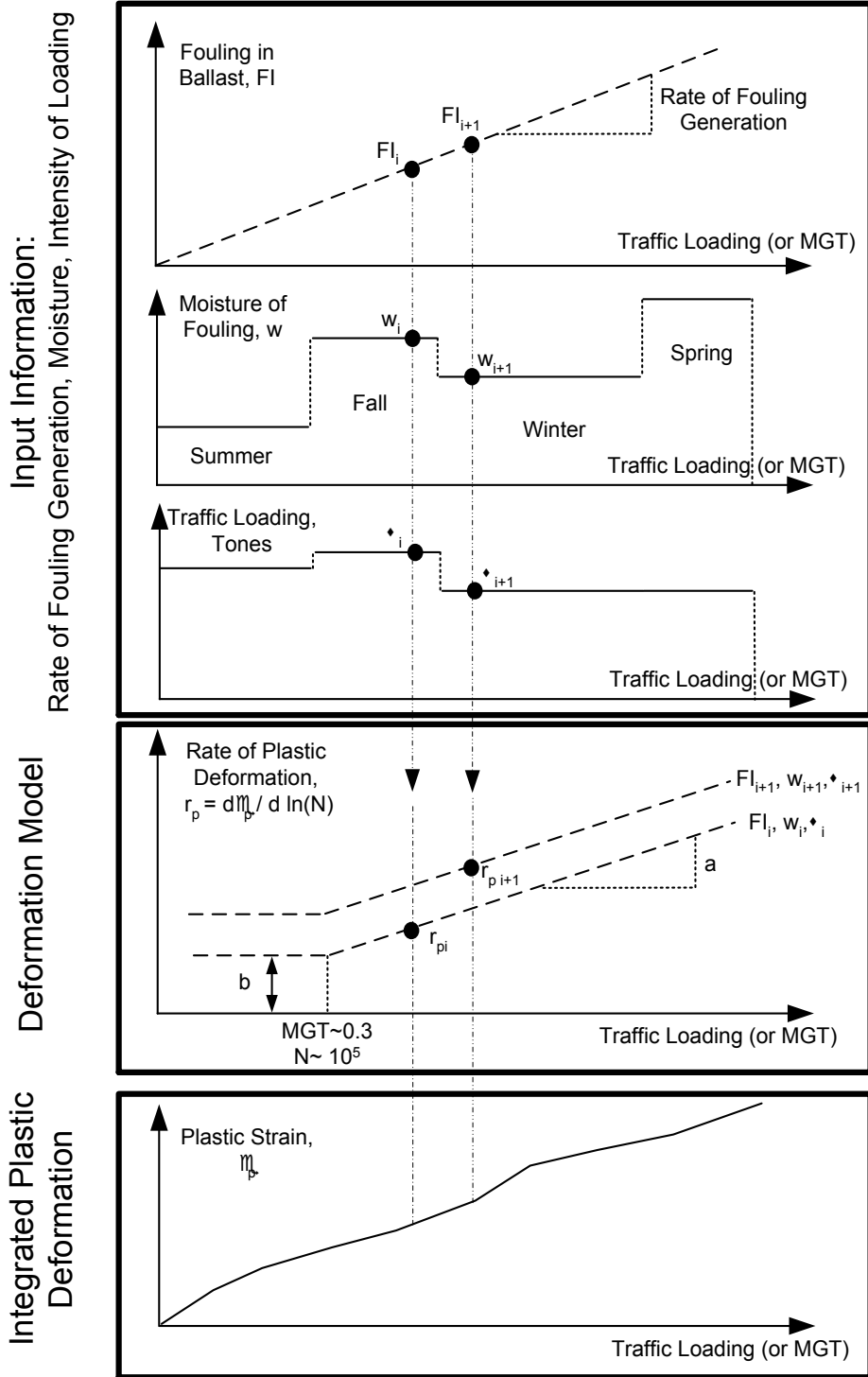


Figure 6.6 Maintenance Planning Using Incremental Analysis of Deformation Model for Ballast with Changing States of Fouling, Moisture, and Traffic

### 6.8 DEFORMATION MODEL OF RAILWAY SUBGRADE

To determine the surface deviation of railway track due to accumulation of deformation in the rail substructure, deformational behaviors of both the ballast and the subgrade layers are required. The deformation of subgrade can be predicted using the equation proposed by Li and Selig (1994), as follows:

$$\varepsilon_{ps} (N) = c \left( \frac{\sigma_{ds}}{\sigma_s} \right)^m N^d \quad (\text{Eq. 6.14})$$

where  $\varepsilon_{ps}$  (%) is the plastic strain of railway subgrade,  $\sigma_{ds}$  is the deviator stress on the subgrade, and  $\sigma_s$  is the unconfined subgrade strength described by Li and Selig (1994). Parameters 'c', 'd', and 'm' are related to the type of subgrade materials and proposed by Li and Selig (1994) and summarized in Table 6.2. The incremental calculation of plastic strain of the subgrade is also performed similar to the railway ballast to incorporate the strength of subgrade (i.e.,  $\sigma_s$ ) and the state of stress (i.e.,  $\sigma_{sd}$ ).

Talbot's equation (1985) is used to find the cyclic stress on subgrade ( $\sigma_{sd}$ ). The stress beneath the centerline of the tie at depth  $h$  (mm) below the tie,  $\sigma_{sd}$ , (kPa) is a function of stress over the bearing area of the tie ( $\sigma_t$ , kPa). Therefore, for a given thickness of ballast equal to  $h$ , stress on the subgrade is,

$$\sigma_{sd} = 957 \frac{\sigma_t}{h^{1.25}} \quad (\text{Eq. 6.15})$$

Table 6.1 Deformation Model Parameters for Railway Subgrade (from Li and Selig 1994)

Model Parameters	Subgrade Classification			
	ML	MH	CL	CH
d	0.1	0.13	0.16	0.18
c	0.64	0.84	1.1	1.2
m	1.7	2.0	2.0	2.4

### 6.9 RAIL TRACK SURFACE DEVIATION

Chrismer and Selig (1994) showed that the change in surface deviation of the railway track ( $\delta_v$ ) is a function of initial surface deviation ( $\delta_{v0}$ ), and the deformation of the track ( $d_L$ ) under traffic loading is:

$$\delta_v = \delta_{v0} + 0.15 d_L \quad (\text{Eq. 6.16})$$

where  $\delta_{v0} = 2.5$  mm was recommended if input data is lacking.  $d_L$  is the track deformation (from fouled ballast and subgrade), which is calculated from the deformation model presented in this study. This approach is adopted here.

### 6.10 MECHANISTIC-BASED MAINTENANCE PLANNING FOR RAIL SUBSTRUCTURE (WISCRAILTM)

A computer software program was developed using MATLAB<sup>TM</sup> to predict the surface deviation of the rail track due to deformation of railway substructure. This program incorporates the deformation model of railway ballast and subgrade as described above. The graphical user interface of the mechanistic based maintenance planning model for railway substructure, called 'WiscRail<sup>TM</sup>', is shown in Fig. 6.7. This program is capable of predicting the surface deviation of railway track for different fouling condition, subgrade material, and traffic load. As shown in Fig. 6.7, the program includes traffic data, change in axle load (indication of heavier freight load), moisture in fouled ballast, ballast condition, subgrade condition, initial track condition, rate of fouling generation due to particle breakage, subgrade infiltration, and external fouling. When surface deviation of railway track due to deformation of substructure exceeds the assigned limit based on various classes of railway systems and operation speeds, the maintenance is required. An example of required track alignments (i.e., tamping) is a 10-mm limit for surface deviation as shown in Fig. 6.7. For the given traffic and track conditions, five tamping activities are required in 6 years of track operation.

### 6.11 ANALYTICAL SUPPORT VECTOR REGRESSION

In addition to the deformation model discussed in this study, the concept of statistical learning (i.e., SVR) was used to predict the deformation of ballast for comparison. Hsu et al. (2010) proposed the

consideration of the radial base function (RBF) kernel  $K(x_i, x_j) = \exp(-\gamma \|x_i - x_j\|^2)$  that creates a reasonable mapping function for typical engineering data. There are two parameters for SVR method with an RBF kernel:  $C$  and  $\gamma$ . Parameters  $C$  and  $\gamma$  are unknown beforehand and model selection (parameter search) must be done. The parameter search is done to identify  $C$  and  $\gamma$  so that the statistical deformation model can accurately predict unknown testing data (i.e., plastic strains). A common method is to separate the data set into two parts, of which one is considered unknown. An improved version of this procedure is known as cross-validation. Hsu et al. (2010) proposed to use cross-validation to find the best parameter  $C$  and  $\gamma$  to train the data set and test the data. 5-fold cross-validation was done in this study where we first divide the training set into 5 subsets of equal size. Sequentially one subset is tested using the regression model trained with the remaining 4 subsets. Each instance (i.e., rate of plastic strain) of the entire training set is predicted and the cross-validation accuracy is the percentage of data which are correctly predicted. The cross-validation procedure can prevent the over-fitting problem (Hsu et al 2010).

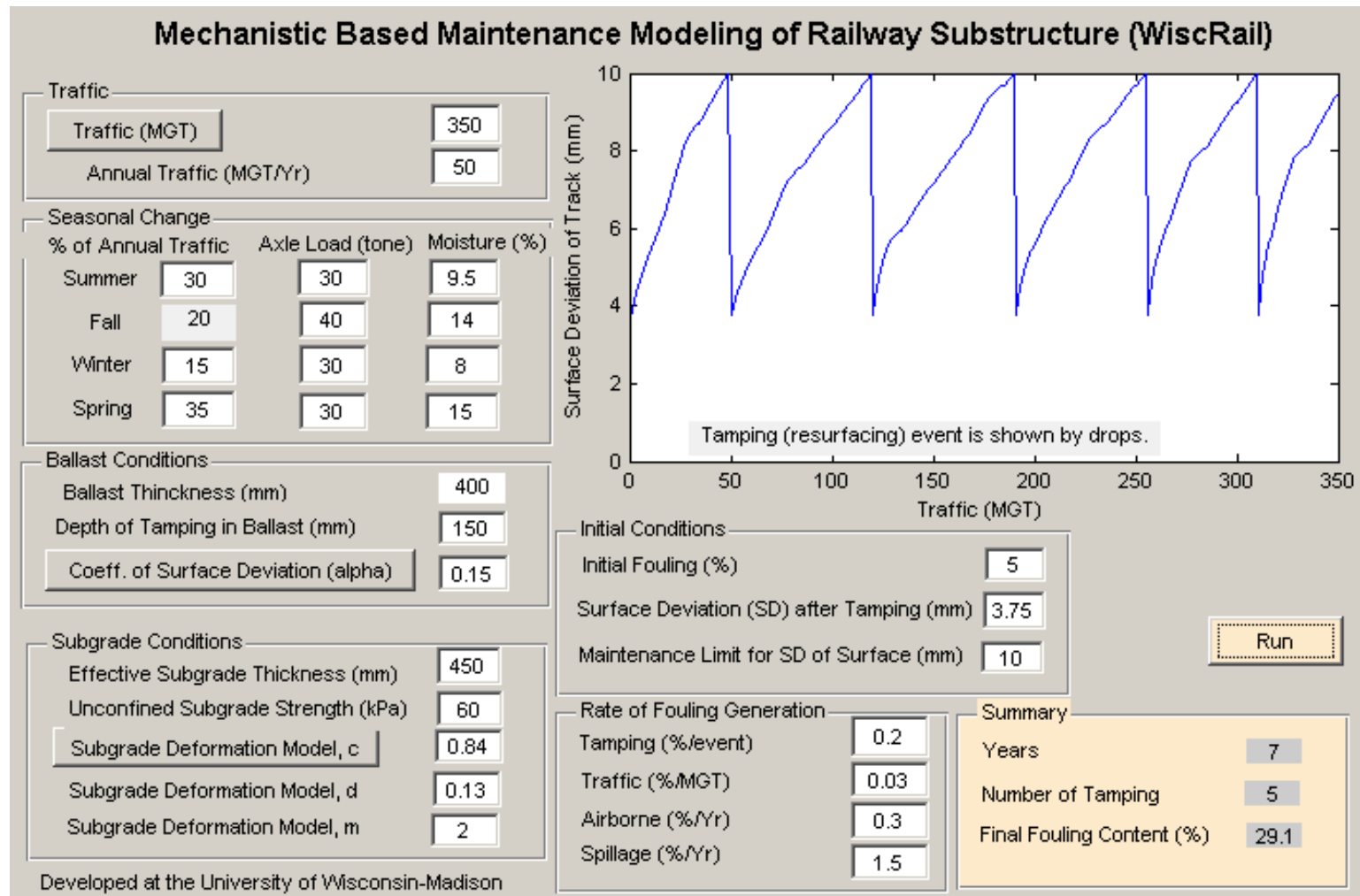


Figure 6.7 Graphical User Interface Software of Mechanistic Based Maintenance Model of Railway Substructure (WiscRail™)

Various pairs of  $(C, \gamma)$  values was tried by exponentially growing sequences of  $C$  and  $\gamma$  to identify good parameters, e.g.,  $C = 2^{-5}, 2^{-3}, \dots, 2^{15}$  and  $\gamma = 2^{-15}, 2^{-13}, \dots, 2^3$ . The set of  $C$  and  $\gamma$  with the best cross-validation accuracy was selected. All of the experimental calculations for SVR were conducted using the LIBSVM toolbox for MATLAB™ (Chang and Lin 2001).  $C = 1000$  and  $\gamma = 0.6$  resulted in the best statistical model with coefficient of deterioration ( $R^2$ ) of 0.96. The comparison between the prediction of the rate of plastic strain ( $r_p$ ) of railway ballast obtained from the developed deformation model in this study and the SVR is shown in Fig. 6.8. The SVR can predict the  $r_p$  of railway ballast with  $R^2 = 0.98$ , whereas the  $R^2$  is 0.89 based on the developed deformation model. Even though the SVR method more accurately determines the  $r_p$  of railway ballast, the lack of data in  $N > 1$  million significantly limits the application of this method for prediction of the railway maintenance in long-term service life. The proposed method is based on laboratory tests and requires validation in the field.

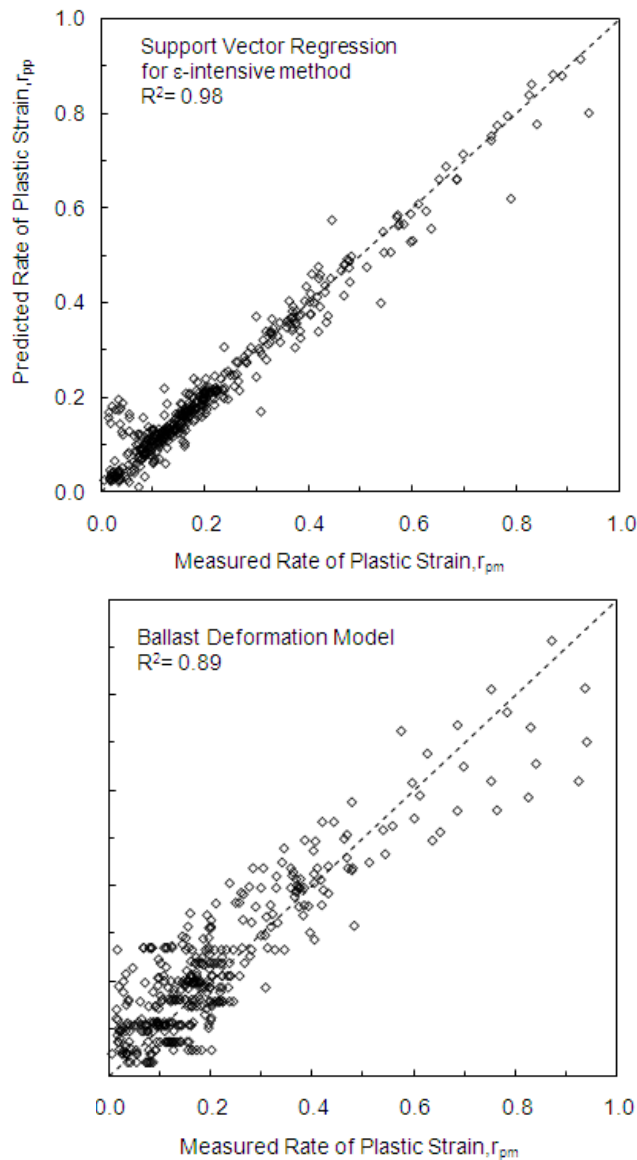


Figure 6.8 Comparison of Predicted Data from Ballast Deformation Model and Statistical Regression Method (SVR with  $\epsilon$ -insensitive of 0.1)

## 6.12 SUMMARY AND CONCLUSIONS

In this paper, a mechanistic-based maintenance planning and scheduling model is presented based on a deformation model of railway substructure. For predicting the permanent deformation of ballast, two approaches were taken. The first approach is based on a ballast deformation model, and the second approach is based on a statistical technique termed “Support Vector Regression – SVR”. Both approaches are based on the data obtained using large-scale cyclic triaxial apparatus. Two main phases were distinguished in the deformation model: (1) an initial compaction phase, where the semi-logarithmic  $r_p$  remains constant for loading cycles,  $N$  up to 10 000 and (2) a fouling impact phase, where  $r_p$  increases linearly due to the presence of fouling materials. Parameters ‘a’ and ‘b’ were used to characterize the FIP and ICP in the deformation model. A correlation between ‘a’ and ‘b’ parameters and fouling index, moisture, and state of stress are presented. The integrated plastic deformation of railway ballast in different fouling, moisture, and traffic loading conditions is used, along with a subgrade deformation model, to develop mechanistic based equations to predict the surface deviation of the railway track. Similarly, SVR is applied to the data to develop a predictive model. The SVR method determines the  $r_p$  of railway ballast more accurately; however, the SVR method is limited only over the range of  $N$  for which the data was developed. Finally, a maintenance planning and scheduling software program was developed by incorporating the predictive deformation model for railway substructure, which sets limits on the surface deviation of the railway track. The proposed method is based on laboratory tests and, although powerful, is recommended for a field validation prior to full-scale implementation in the profession.

## ACKNOWLEDGEMENT

Funding for this research was provided by the National Center for Freight and Infrastructure Research and Education (C-FIRE). Assistance from the BNSF Railway and Wisconsin and Southern Railroad Company for providing the ballast is appreciated.

## REFERENCES

- Andersson, M., 2002, *Strategic Planning of Track Maintenance*, Swedish National Rail Administration (Banverket), TRITA-INFRA 02-035
- Chang, C.C., and Lin, C.J., 2001, *LIBSVM: a Library for Support Vector Machines*, Software available at <http://www.csie.ntu.edu.tw/~cjlin/libsvm>
- Chrismer, S., and Davis, D., 2000, Cost Comparisons of Remedial Methods to Correct Track Substructure Instability, *Trans. Res. Rec.*, 1713, Paper #00-019, 10-15
- Chrismer, S.M., and Selig, E.T., 1994, *Mechanics-Based Model to Predict Ballast-Related Maintenance Timing and Costs*, Ass. of American Railroads, Report No. R-863, AAR-Technical Centre, Chicago, Illinois, USA
- Darell, D.D., 2003, Substructure Can Add Life to Rail and Ties, *Railway Track and Structures*, 99(3), pp.25–27
- Dibike, Y.B., Velickov, S., Solomatine, D.P., Abbott, M.B., 2001, Model Induction with Support Vector Machines: Introduction and Applications. *Journal of Computing in Civil Engineering*, 15(3), pp.208–216
- Fazio, A.E., and Prybella, R., 1980, Development of an Analytical Approach to Track Maintenance Planning, *Trans. Res. Rec.* 744, National Research Council, National Academy Press, Washington, D.C., USA, pp.46-52
- Hsu, J., Chang, C.C., and Lin, C.J., 2010, *A Practical Guide to Support Vector Classification*
- Huang, H., Tutumluer, E., Dombrow, W., 2009, Laboratory Characterization of Fouled Railroad Ballast Behavior, *88th annual Mtg. of Trans. Res. Board*, on CD-ROM
- Larsson, D., and Gunnarsson, J., 2001, A Model to Predict Track Degradation Costs, *Proc. of the 7th Inter. Heavy Haul Conf.*, Inter. Heavy Haul Ass. Inc., Virginia Beach, VA, USA, pp. 437-444.
- Lee, H. M., 2009, Ballast Evaluation and Hot Mixed Asphalt Performance, *Proc. BCR2A Conf.*, Univ. of Illinois Urbana-Champaign, Urbana, IL, pp.1283-1289

- Li, D., and Selig, E.T., 1994, Cumulative Plastic Deformation for Fine-Grained Subgrade Soils, *J. Geotech. Engrg.*, ASCE, 122(12), pp.1006-1014
- Maalouf, M., Khoury, N., and Trafalis, T.B., 2008, Support Vector Regression to Predict Asphalt Mix Performance. *International Journal For Numerical And Analytical Methods In Geomechanics*, 32, pp.1989–1996
- Pal, M., 2006, Support Vector Machines-Based Modeling of Seismic Liquefaction Potential, *International Journal for Numerical & Analytical Methods in Geomechanics*, 30, pp.983–996
- Selig, E.T., and Waters, J.M., 1994, *Track Geotechnology and Substructure Management*, Thomas Telford, NY
- Smola, A.J., and Scholkopf, B., 2004, A Tutorial on Support Vector Regression, *Statistics and Computing*, 14, pp.199-222
- Stirling, A.B., Roberts, C.M., Chan, A.H.C., Madelin, K.B., and Bocking, A., 1999, Development of A Rule Base (Code of Practice) for the Maintenance of Plain Track in the UK to Be Used in An Expert System, 2<sup>nd</sup> *Inter. Conf. on Railway Engineering*, London, UK
- Su, L., Rujikiatkamjorn, C., Indraratna, B., 2010, An Evaluation of Fouled Ballast in a Laboratory Model Track Using Ground Penetrating Radar, *ASTM Geot. Testing J.*, GTJ103045
- Talbot, A.N., 1985, *Stresses in Railroad Track-The Talbot Reports*, American Railway Engineering Association
- Vapnik V.N., 1995, *The Nature of Statistical Learning Theory*, Springer: New York
- Zaremski, A.M., 1998, Development and Implementation of Integrated Maintenance Planning Systems, Transportation Research Board Annual Meeting 1998, Washington D.C.

## **CHAPTER 7: SUMMARY AND MAJOR FINDINGS**

### **7.1 HIGHWAY RESEARCH**

Large-scale model experiments (LSME) and standard bench-scale resilient modulus (BSRM) tests were conducted on base course materials consisting of recycled pavement material (RPM), reclaimed road surface gravel (RSG), and conventional Class 5 base from Minnesota. The RPM and RSG were tested alone and with fly ash stabilization. Based on the findings of this study, the following conclusions are made:

The SRM of unstabilized base course materials backcalculated from the LSME was dependent on layer thickness and higher than that from the BSRM tests. This difference is explained by the differences in strain amplitudes induced in each method.

Plastic deformation behavior of materials obtained from the LSME indicated that the RPM and RSG have higher potential for accumulating plastic deformation during the service life of pavement system compared to the natural aggregate and stabilized RPM and RSG (SRPM and SRSG), which exhibit negligible plastic deformations.

Layer coefficients of the unstabilized granular base materials are not constant but increase with thickness. The layer coefficients for RSG and RPM are in the range of 0.1-0.2 and 0.1-0.25 depending on layer thickness (0.1 to 0.4m). The SRPM and SRSG have a layer coefficient of 0.3, which is independent of layer thickness. Stabilization of recycled materials can reduce the required thickness of the base course up to 30% based on the AASHTO 1993 design guide.

The lifetime expectancy of test materials predicted by the MEPDG code showed that not only the resilient modulus but also the plastic deformation of alternative recycled materials is essential for comprehensive design procedure when alternative materials are used. The results showed that stabilization of recycled materials with fly ash increases the lifetime of pavements constructed with 0.3-m-thick alternative recycled materials from 17 to 21 years.

### **7.2 RAILWAY RESEARCH**

A testing protocol and guidelines for fouled ballast has been developed due to the lack of consistent and systematic testing guidelines in the literature and in rail engineering practice. Confining stress ( $\sigma_3$ ) in the ballast layer was varied between 20 and 200 kPa, and deviator stress ( $\sigma_d$ ) between 50 and 300 kPa. A 5-Hz haversine, bell-shaped loading pulse simulates the traffic loading on ballast. A representative state of stress for railway ballast of  $\sigma_3 = 90$  kPa and  $\sigma_d = 300$  kPa in the LSCT was determined. Ballast that is mixed with relatively dry fouling material prior to compaction prevents the development of heterogeneous layers and simulates tamping activities (such as performed during maintenance events) in the track. Moisture that is added from the top of the specimen was found to best represent changing water content conditions during the study of deformational behavior of ballast.

The effect of fouling (internally generated mineral fouling, external coal fouling due to surface spillage, and clay fouling due to subgrade intrusion) on the permanent deformation of ballast under traffic loading was systematically studied. Large-scale cyclic triaxial test results showed that increased fouling and moisture contents accelerate the accumulation of plastic strains ( $\epsilon_p$ ) in ballast. Two main phases were distinguished in the development of  $\epsilon_p$  with loading cycles in fouled ballast: (1) initial compaction phase (ICP), where the  $\epsilon_p$  of ballast steadily increases to a certain point ( $N < 10,000$ ) and (2) fouling impact phase (FIP), where the  $\epsilon_p$  and the rate of plastic strain of ballast increases due to the presence of fouling materials (or remains stable in the absence of fouling). For non-cohesive (mineral and coal) fouling, fouling index and moisture were the controlling parameters. A non-cohesive fouling index (NFI) was introduced to account for the factors affecting the  $\epsilon_p$ . For cohesive (clay) fouling, in addition to fouling index and moisture, Atterberg limits (PL and LL) and % of P200 were identified as controlling parameters. A cohesive fouling index (CFI) was introduced to account for these factors. In this perspective, the indices for fouled ballast are expected to provide useful tools for assessing track condition. These parameters create a mechanistic rating system for controlling the quality of railway tracks without the shortcomings found in other indices (e.g., Selig and Waters 1994; Insoes 2002) that lack information about critical fouling levels and the ability to extend results for a lifetime assessment.

A limit for deformational behavior of fouled ballast was illustrated using suction-based mechanisms. For a representative state of stress for ballast, fouling materials, irrespective of type, with suction  $> 2,000$  kPa only show the initial compaction phase. The main mechanism for accumulation of plastic strain in ballast is contaminated contact points of ballast particles by the fouling materials. Also, decreased shear strength of fouling materials at the contact points under cyclic loading increases the plastic strain of ballast in cohesive and non-cohesive fouling. The effect of maintenance on  $\epsilon_p$  was studied. Ballast in a highly fouled condition exhibits extensive  $\epsilon_p$  immediately after tamping due to rearrangement of the particles and loss of dense condition that has been achieved in previous traffic loading.

Depth and moisture content of fouling were evaluated using TDR techniques. The waveforms generated from TDR probes showed that the increase in the water content and depth of fouling changes the electromagnetic properties of ballast. Increasing the fouling depth to depth of ballast from 0 to 75% increases the relative real dielectric permittivity of fouled ballast from 1.2 to 2.0, while the EM wave velocity decreases from 0.27 to 0.21 m/ns. The TDR data showed that increasing the water content of fouling material increases the electrical conductivity, calculated from TDR wave forms. An increase in the water content of fouling from 5 to 10% increases the electrical conductivity of fouled ballast three times. The data obtained from the TDR show that a qualitative method can be developed to detect the depth of fouling and water content in the ballast by evaluating the change in the electromagnetic properties of ballast during gradual changes of fouling content, starting with clean ballast.

Compiling these efforts together, a maintenance planning and scheduling program for railway substructure is proposed. A deformation model including the FIP and ICP was developed based on the data obtained from the LSCT apparatus. FIP and ICP in the deformation model were characterized in various fouling conditions, moisture contents, and states of stress. A maintenance planning and scheduling software was developed incorporating the predictive deformation model for railway substructure by limiting the surface deviation of the railway track. Developing a maintenance planning for railway track due to deformation of substructure reveals the benefits of mechanistic characterization of ballast. Based on the developed model and a given track condition, ballast with initial fouling of 5% requires four maintenance activities (i.e., tamping events) to level the track surface during six years of evaluation. Based on this model, fouling increases to 25% after six years.